Spring 2024

Experimental investigation of high-temperature brine-shale interactions

Anna Atasha Hoffmann
Missouri University of Science and Technology

Department: Geosciences and Geological and Petroleum Engineering

EXPERIMENTAL INVESTIGATION OF HIGH-TEMPERATURE BRINE-SHALE INTERACTIONS

by

ANNA ATASHA HOFFMANN

A DISSERTATION

Presented to the Graduate Faculty of the

MISSOURI UNIVERSITY OF SCIENCE AND TECHNOLOGY

In Partial Fulfillment of the Requirements for the Degree

DOCTOR OF PHILOSOPHY

in

GEOLOGY AND GEOPHYSICS

2023

Approved by:

David Borrok, Advisor
John Hogan
Jonathan Obrist Farner
Taghi Sherizadeh
Wan Yang

PUBLICATION DISSERTATION OPTION

This dissertation consists of the following two articles, formatted in the style by the Missouri University of Science and Technology:

Paper I, found on Pages 5-38, has been accepted by Applied Geochemistry Journal for publication.

Paper II, found on Pages 39-69, has been submitted to Applied Geochemistry Journal for publication.

ABSTRACT

Hydrofracturing (fracking), a common practice in the Petroleum Industry to induce or improve fluid flow in tight formations, creates chemical disequilibrium that further alters the porosity and permeability of host rocks and results in the production of saline and contaminated produced waters (PW). The PW of the Tuscaloosa Marine Shale (TMS) are Na-Ca-Mg-K-Cl brines with mean concentrations of approximately 16% Total Dissolved Solids (TDS) and circumneutral pH. Analysis of composition suggests the PW result from a 20 to 80% dilution of formation waters (relict brines of the Louann Salt) by fracking fluid. Trace element concentrations generally show moderate to strong correlations with overall salinity. Low concentrations of Pb and Zn suggest the presence of high amounts of H_2S in the TMS, limiting the solubility of sulfide phases.

Fracking is also used in wastewater disposal and enhanced geothermal system (EGS) energy production, where chemical variations of injection fluid affect the disequilibrium reactions in the host rocks. To improve our understanding of fluid-shale interactions over a broad range of fluid chemistries, we performed 56-day batch reaction experiments between TMS shales and solutions with combinations of the following initial values; (1) pH of 2, 4, or 6 (2) salinities of <0.1%, 3.2%, or 12% TDS, and (3) NaCl or Na-Ca-Mg-K-Cl compositions. Findings show that while the timing and extent of reactions varied with the initial fluid chemistry, resulting solutions converged to similar end chemistries, indicating that wastewater disposed or reused as fracking fluid into parent formations and the cycling of water-based EGS fluids should not have a significant secondary impact on host formation porosities.

ACKNOWLEDGMENTS

Kevin Gibbs, Darrell Knight, and the Goodrich Petroleum Company were instrumental in the collection of the produced waters. This material is based upon work supported by the Department of Energy National Energy Technology Laboratory under Award Number DE-FE0031575 (TUSCALOOSA MARINE SHALE LABORATORY). We also appreciate the analytical support provided by the Center for Earth and Environmental Isotope Research at UT El Paso.

TABLE OF CONTENTS

LIST OF ILLUSTRATIONS

PAPER I Page

PAPER II

NOMENCLATURE

Symbol	Description
Al	Aluminum
As	Arsenic
B	Boron
Ba	Barium
Br	Bromide
Ca	Calcium
Cd	Cadmium
Cl	Chloride
Co	Cobalt
Cr	Chromium
Cu	Copper
Fe	Iron
K	Potassium
Mg	Magnesium
Mn	Manganese
Mo	Molybdenum
Na	Sodium
Ni	Nickel
Se	Selenium

Si	Silica
SO_4	Sulfate
Sr	Strontium
Tl	Thallium
P	Phosphorus
Pb	Lead
V	Vanadium
Zn	Zink
bbl	Billion barrels
CO_2	Carbon Dioxide
DW	Dilute Water
EDS	Electron Dispersion Spectrum
EGS	Enhanced Geothermal Systems
FWV	Flowback Water Volume
gal	Gallons
g/L	Grams per Liter
HCO_3	Bicarbonate
H_2O	Water
H_2S	Hydrogen Sulfide
IC	Ion Chromatography
ICP-MS	Inductively Coupled Plasma Mass Spectrometry
ICP-OES	Inductively Coupled Plasma Optical Emission Spectrometry

kV	Kilovolts
mcf	Million cubic feet
mg/L	Milligrams per Liter
mm	Millimeters
pH	Alkalinity
POV	Produced Oil Volume
PW	Produced Waters
PWV	Produced Water Volume
SE	Scanning Electron
SEM	Scanning Electron Microprobe
TDS	Total Dissolved Solids
TMS	Tuscaloosa Marine Shale
USGS	United States Geological Survey
wt%	Weight Percent
XRD	X-Ray Diffraction
Ab	Albite
An	Anorthite
Bar	Barite
Cal	Calcite
Dol	Dolomite
Gyp	Gypsum
Il	Illite

Kao	Kaolinite
Ksp	Potassium Feldspar
Qtz	Quartz
NaCl	Salt

1. INTRODUCTION

When water is injected into the deep subsurface, mineral precipitation, and dissolution reactions influence the porosity and permeability of the host strata. Changes in porosity and permeability can enhance or retard fluid flow that is essential for activities such as hydrofracking operations in hydrocarbon source rocks, the disposal of contaminated waters (often water co-produced with hydrocarbons), and the efficiency of deep geothermal energy operations. To improve the understanding of critical water-rock interactions in shale-rich strata, high-temperature batch reaction experiments were performed to track fluid evolution and physical changes within the rocks. The project will evaluate a range of fluid conditions, including variable salinity, chemistry, pH, and oxidative states, to explore a variety of potential interactions.

The hydrofracturing process typically involves pumping large volumes of dilute water (often groundwater or stream water) amended with chemical treatments into a low-permeability hydrocarbon source rock. Water pumped at pressures exceeding the rock strength induces fracturing to allow fluid flow. Several studies have observed rapid changes in fracking water chemistry as water is returned to the surface after the hydrofracking process. These studies have shown that within the first two to three weeks of fracturing, there are rapid increases in total dissolved solids (TDS) of the flowback water (e.g., Engle and Rowan, 2014; Balashov et al., 2015; Vengosh et al., 2017). Elements such as sodium (Na), chloride (Cl), calcium (Ca), magnesium (Mg), bromine (Br), and strontium (Sr) tend to increase rapidly, while concentrations of sulfate decrease rapidly. The loss of sulfate may be tied to barite precipitation, as concentrations of Ba

decrease rapidly after an initial increase (Engle and Rowan, 2014). Sulfates may also be converted quickly to oxide minerals (Harrison et al., 2017; Lu et al., 2017b).

Several studies have recently been conducted to determine the source of increased TDS values in the returned fracking fluids. These studies have shown that increases in TDS are the result of frac fluid mixing with formation waters, as well as the dissolution of carbonate minerals, oxidation of pyrite, and some albitization and illitization reactions (Harrison et al., 2017; Lu et al., 2017a; Lu et al., 2017b; Osselin et al., 2019). The study by Lu et al., 2017b, looking at shale reactions to solutions of varying salinity, is one of the more extensive studies. The authors used simulated brines of various TDS concentrations to examine the dissolution and precipitation of minerals and their relationship to porosity and permeability. The authors identified the dissolution of calcite, dolomite, feldspar, and pyrite oxidation as critical factors in controlling permeability and porosity. They also suggested that increasing the salinity of the initial fracking fluid would increase dissolution and decrease precipitation. This was an excellent study, but it still leaves substantial gaps in our knowledge regarding the nature of these reactions.

For example, the fluid chemistry investigated in this study focused only on the Na-Cl system. In contrast, interaction with formation waters in natural systems involves complex chemical components, including additional elements that may lead to mineral precipitation. These are essential variables, as fracking fluids amended with acid treatments typically have a pH of about 2, while formation waters have a pH between 6 and 8. This means there are likely different reactions occurring throughout a broad range of pH. Moreover, changes in pH and redox conditions were not a focus of the Lu et al. (2017b) study.

Produced waters (PW) are a significant byproduct of the oil and gas industry. An estimated 900 billion barrels of PW are annually generated in the United States. Disposal methods are limited due to the high concentration of TDS (Clark and Veil, 2009; Veil, 2012). Produced waters have TDS concentrations between 100,000 to 400,000 mg/L and often include heavy metals, metalloids, and potentially hazardous dissolved organics (e.g., Carpenter et al., 1974; Kharaka et al., 1987; Benko and Drewes, 2008; Acharya et al., 2011; Alley et al., 2011; Boschee et al., 2014; Lester et al., 2015; Vengosh et al., 2017). According to an Argonne National Laboratory's 2009 study, most on-shore PW in the US is disposed of using deep injection wells, either into the formation where oil and gas were extracted (59%) or within deep non-producing (40%) formations. If we are to continue injecting PW into formations, we need to understand better how the PW chemistries (concentrations, components, and pH, among others) will interact with host rocks to determine how effective the sequestration is and how it might be improved. These interactions are significant for understanding the long-term fate and transport of potentially hazardous metals and metalloids.

The current progressive focus on geothermal energy production is on Enhanced Geothermal Systems (EGS), which evolved from an earlier Hot Dry Rock production concept. In this system, hot rocks (typically deep in the subsurface), which usually have low permeability and a lack of natural fractures, are drilled, synthetically fractured, and flooded with a fluid, which is then heated by the host rocks and pumped back to the surface to provide thermal energy (e.g., Gallup, 2009; Olasolo et al., 2016). There are two types of EGS, based on the 'working' fluid used; CO2-EGS and H2O-EGS. Due to early concerns regarding water-rock interactions at depth and the interest in using EGS as a

possible form of CO2 sequestration, most studies of fluid efficiency have focused on CO2-EGS (e.g., Olasolo et al., 2016). This focus on CO2-EGS has slowed our understanding of how H2O-EGS systems will impact the porosity and permeability of host rocks. These systems could perform better than CO2-EGS in deeper, larger energy content reservoirs (André et al., 2006; Regenspurg et al., 2010; Zhang et al., 2013; Pandey et al., 2014; Pandey et al., 2015). A recent study by Li et al. in 2019, using thermal-hydraulic-mechanical modeling, also suggests that H2O-EGS supports a higher heat extraction rate than CO2-EGS for the first and last ten years of a 30-year production period. Therefore, it is essential to understand water-rock interaction in the deep subsurface under various temperature and pressure conditions and within different rock types.

In this study, I will evaluate high-temperature reactions between shale-rich rock and fluids of varying chemistries using mixtures of dilute water and simulated produced water end members. I will also assess the impact of starting pH and the oxidation state of the fluids on these reactions. Both the fluid compositions and rock properties will be investigated. These parameters will allow the aggregate data to be used to understand fluid evolution in relation to mineral dissolution and precipitation and the overall changes to porosity and permeability. The expected outcomes of this investigation will be to (1) Identify the conditions that are most conducive to creating and maintaining permeability from hydrofracking, (2) Evaluate the consequences of using PW as a component for hydrofracking (as well as other subsurface disposal options), and (3) Provide guidance on how recycled brines within an H2O-EGS may influence rock conditions (at least where shale is present) over time.

PAPER

I. THE GEOCHEMISTRY OF PRODUCED WATERS FROM THE TUSCALOOSA MARINE SHALE, USA

Anna Hoffmann, David Borrok

Department of Geoscience and Geological and Petroleum Engineering, Missouri University of Science and Technology, Rolla, MO 65409

ABSTRACT

Produced water is a byproduct of oil and gas production. The chemistry of produced water may provide information about the source of the fluid and its evolution, leading to an improved understanding of the hydrology of petroleum systems. In this study, samples from 19 wells from the Tuscaloosa Marine Shale (TMS) in Mississippi and Louisiana, USA were analyzed for their major and trace element compositions. Data obtained from produced waters from the TMS were compared to existing chemical data from produced waters collected from nearby hydrocarbon reservoir rocks within the Gulf Coast Basin. The results show that produced waters from the TMS are highly saline, with a mean concentration of 15.9 g/L of total dissolved solids. Comparison of the chemistry of produced water from the TMS to early flowback waters demonstrated a rapid shift from the more dilute fracturing fluid to the formation water endmember composition. Most of the trace metals showed a moderate to strong correlation with the overall salinity

of the waters. Concentrations of Cu and V showed a moderate correlation with the amount of oil produced from the TMS wells, suggesting that these elements are strongly affiliated with the kerogen and subsequent dissolved (< 0.45 micron) organic phases. Analysis of the volume of produced water compared to the volume of water used during hydraulic fracturing indicates that 15% to 110% of the water volume used for fracking had been returned to the surface over the 2 to 5 year production period of the sampled wells. Chloride to bromide ratios suggest that the formation water in the TMS was derived from evaporated seawater. Comparison to historical data for produced waters in other formations in and around the Mississippi Salt Basin showed that waters in all the formations had a consistent origin (bitterns likely derived from the formation of the Louann salt). This implies that over geologic time periods fluids migrated through the TMS despite its low permeability present-day. The TMS also exhibited lower concentrations of dissolved transition metals such as Zn and Pb relative to those described in adjacent formations. This observation may suggest the presence of larger amounts of H2S, limiting the solubility of sulfide phases, in the shale unit relative to adjacent reservoir units.

1. INTRODUCTION

An estimated 900 billion barrels of water are annually co-produced with oil and gas in the United States (Clark and Veil, 2009; Veil, 2012). Produced waters are most often associated with high concentrations of salts, heavy metals, metalloids and potentially hazardous dissolved organic constituents (e.g., Carpenter et al., 1974; Kharaka

et al., 1987; Alley et al., 2011; Lester et al., 2015; Vengosh et al., 2017). Despite the well-understood practical water management problems posed by these fluids, produced waters also represent a relatively untapped pool of scientific information that could be used to further our understanding of fluid evolution and the hydrology of petroleum systems (e.g., Barnaby et al., 2004; Zhang et al., 2009; Engle et al., 2016; Saller and Stueber, 2018). For example, Zhang et al. (2009) was able to use the Na/Cl ratios of produced waters to fingerprint two different groups of formation waters in the Uinta Basin, Utah. The shallower fluid, derived from evaporated seawater, mixed with meteoric waters that had dissolved evaporites. The varying degrees of mixing provided insight into the plumping of the basin. Similarly, a study by Engle et al. (2016) identified two distinct chemical groups of formation waters in the Midland Basin. The authors noted that the bimodal salinity of the two waters in the Devonian reservoir suggested the existence of an aquitard acting as a barrier to the mixing of the two fluids. Saller and Stueber (2018) evaluated the formation waters of the Delaware Basin, Midland Basin, and Central Basin Platform and found three distinct chemical groupings that suggested evaporated seawater was being displaced by meteoric waters. The meteoric waters were likely driven by the hydraulic head created by tectonic uplift and the flow was controlled by networks of permeability within the strata.

Other investigators have measured the chemistry of produced water over short timescales to observe how the formation waters evolve in composition over time (e.g., Kim et al., 2016; Kondash et al., 2017; Vengosh et al., 2017). In all cases the flowback water (i.e., water returned in the first week or two of production) quickly changed in composition toward more saline formation waters as more water was produced from the

well. The evolution of these changes provides insight into the rapid water-rock interactions occurring in the subsurface, many of which could influence porosity and permeability and ultimately oil and gas production.

Finally, despite a handful of recent investigations (Barbot et al., 2013; Vengosh et al., 2014; Engle et al., 2016), there is still some debate as to whether the formation waters associated with tight shale hydrocarbon source rocks are chemically the same as the formation waters in surrounding reservoir rocks. Some previous work has suggested that brines within clay-rich strata can develop or inherit slightly different chemical compositions because of the relative impermeability of these units (Kharaka and Smalley, 1976; Fritz, 1986; Sherwood and Craster, 2000). If so, these relationships may be important in deciphering the history of formation waters and understanding the relative connectivity between formations.

In this study, we examined the chemistry of produced waters from 19 operating petroleum wells in the Tuscaloosa Marine Shale (TMS) in Louisiana and southwest Mississippi to investigate the origin(s) of the water and what the chemistry can tell us about the petroleum system. The availability of additional chemical data for produced waters in other units within the same basin provided an opportunity to compare and contrast differences in fluid evolution and the degree of connectivity between nearby geologic units. Additional information on the volumes of fracking water used, and the volumes of water, oil, and gas produced from the wells provided key constraints on fluid evolution.

2. GEOLOGY OF THE TMS AND GULF COAST BASIN

Samples of produced water collected in this study come from wells producing oil and gas in the TMS unit of the Tuscaloosa Group within the Mississippi Salt Basin, a sub-basin within the larger Gulf Coast Basin (Figure 1). The Gulf Coast Basin began forming during the break-up of Pangea in the late Triassic and early Jurassic, as the continental crust underwent extension (Wilhelm and Ewing, 1972; Galloway, 2008). This was followed by marine transgression during the late Jurassic, ultimately leading to the deposition of the Louann Salt (Wilhelm and Ewing, 1972, Galloway, 2008). Subsequent

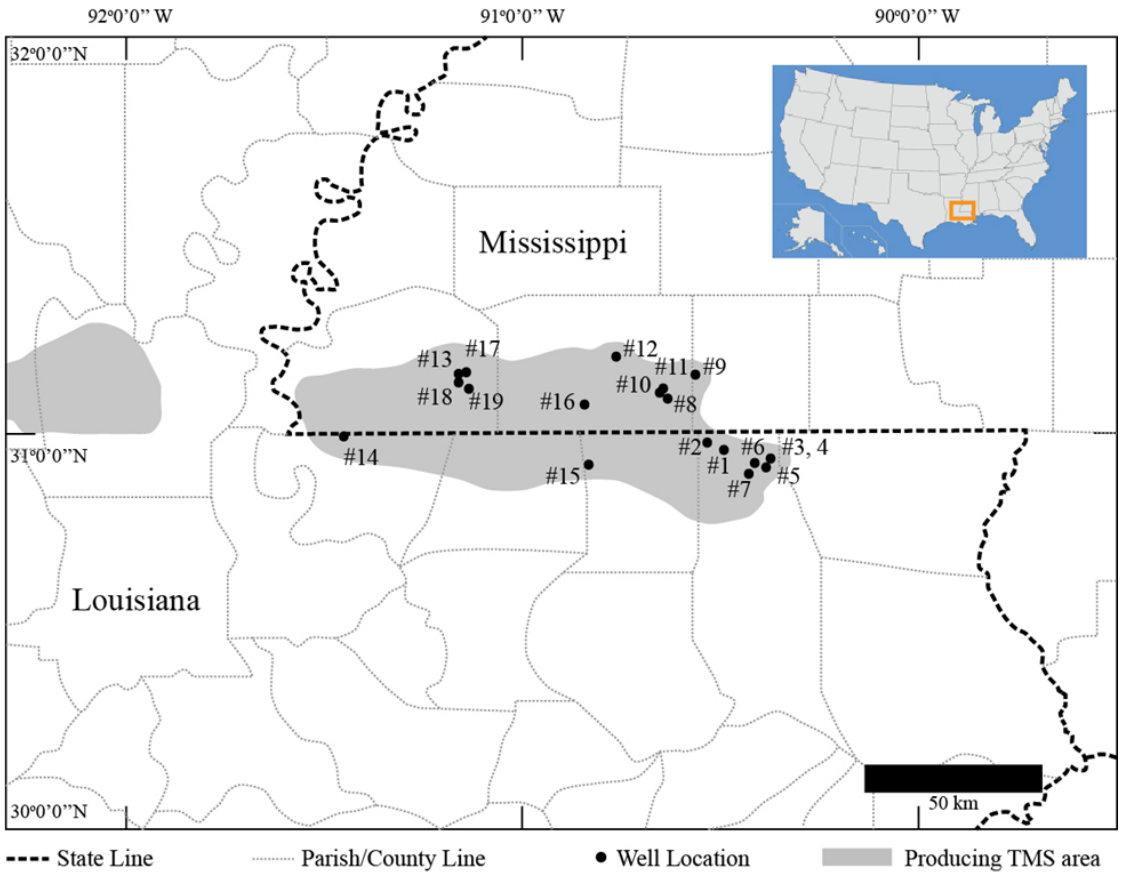

Figure 1. Regional map of the sample locations for produced waters within the TMS. The gray shaded region represents the extent of the currently producing area.

sediment loading led to the formation of many diapiric salt features (Humphris Jr., C.C. 1979; Hudec et al., 2013).

Although the TMS is the primary subject of our investigation, we also compare these data to historical chemical data from produced waters associated with a number of adjacent formations, as outlined in Figure 2. The oldest of these for which data are available is the Smackover Formation of late Jurassic age. The Smackover Formation has a maximum thickness of 430 m and has produced over 500 million bbl of oil (Kharaka et al., 1987; Mancini et al., 2008). The lower Cretaceous red and grey shales of the Hosston and Rodessa Formations have respectively produced 55 and 235 million bbl oil (Kharaka et al., 1987; Mancini et al., 2008). The uppermost unit of the lower Cretaceous is the Mooringsport Formation, which has a maximum thickness of 240 m and has produced 12 million bbl of oil (Kharaka et al., 1987; Mancini et al., 2008). The Tuscaloosa Group is a three-unit package of later Cretaceous sands and shales, which is described in more detail below. The late Cretaceous Eutaw Formation, consisting of calcareous sandstone and carbonaceous shale, spans a thickness of up to about 160 m and has produced 300 million bbl of oil (Kharaka et al., 1987; Mancini et al., 2008). Younger than the Jurassic and Cretaceous units (Figure 2), the Paleocene to Eocene age Wilcox Group, is comprised of a mix of shales, siltstones, and sandstones. The youngest formation where data for produced waters are available is the Eocene Sparta Formation of the Claiborne Group, which is comprised of loose, light colored sands interbedded with dark shales (Murray, 1947).

The TMS extends from the border of Louisiana in the west to Alabama and the Florida panhandle in the east. The TMS dips sharply from north to south towards the Gulf

of Mexico. Hence, TMS rocks sometimes crop out in northern Mississippi and Alabama, while they are deeply buried south of the currently producing area (Figure 1; Spooner, 1964; Mancini et al., 2008; Woolf, 2012). In the producing area in Mississippi and

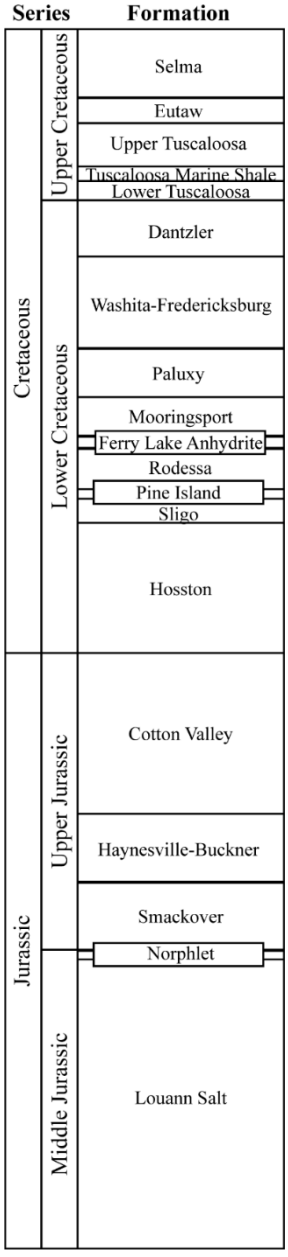

Figure 2. Generalized sequence of Jurassic and Cretaceous strata in the Gulf of Mexico Basin.

Louisiana, the base of the TMS is between 3200 and 4270 m below sea level, and ranges in thickness between 70 and 150 m. The base of the TMS in this region is characterized by a zone of high resistivity identified in well logs (>5 ohms or dramatic increases of >3.5 ohms according to John et al. [1997]). These increases in resistivity are thought to indicate the presence of free oil and gas (Werren et al., 1990; John et al., 1997; Allen et al. 2014). In a recent study of core samples near the base of the TMS from 11 wells in the producing zone, Borrok et al. (2019) indicates that the average concentrations of quartz, calcite, and total clay near the base of the TMS are 22.8 wt%, 17.2 wt%, and 47.6 wt%, respectively. Only minor amounts of other minerals such as pyrite, siderite, dolomite, plagioclase, and potassium feldspar were present (Borrok et al., 2019). Borrok et al. (2019) also reported an average value of 1.65 wt% for the total organic carbon (TOC) content near the base of the TMS. The kerogen in the TMS consists of a mixture of gas prone Type III kerogen and oil prone Type II kerogen. Analysis of Tmax and VRo measurements suggest that the producing area is in the early to middle oil generation window of thermal maturity (Valentine et al., 2016; Enomoto et al. 2017; Borrok et al., 2019). Other investigations where samples were collected over a broader zone of the TMS (including samples outside the producing zone) show roughly similar results, but TOC and calcite contents are lower on average (Valentine et al., 2016; Hackley et al., 2017; Enomoto et al., 2017), indicating that the mineralogy and geochemistry of the TMS is heterogeneous.

3. METHODS

3.1. SAMPLE COLLECTION

Samples of produced water for this study were collected in Nalgene™ plastic bottles from the water stream of the oil-water separator at each well site. No visible oil was present in these samples, so we did not pursue further oil/water separation procedures. At the time of sampling, the wells had been in production from 31 to 63 months (Table S1). Twelve of the samples were collected and processed in the field, while seven were collected a few days later and shipped to our lab at Missouri S&T for processing. Samples processed in the field were analyzed for pH in the field. pH was not measured for the samples processed off site. Samples processed in the field were filtered using 0.45 micron nylon syringe filters. Those analyzed for cations were acidified to a pH of 1.5 with drops of pure nitric acid, while samples analyzed for anions were filtered but not acidified. All samples were refrigerated for later analysis. Samples shipped to Missouri S&T were similarly processed; however, samples analyzed for cations were acidified to pH 1.5 prior to filtering to solubilize any trace elements that might have sorbed to solid particles in the raw waters prior to filtering. To ensure that the different processing methods did not bias the samples, we compared the concentrations of major and trace elements from the samples processed in the field with those processed in the lab. The results were quite similar in that the interquartile ranges (the ranges where the middle 50% of the data are found) were similar for all major and trace elements measured in both groups except for Zn, Mn, and Se (Figures S1 and S2). Because of this

discrepancy, we have not included data for Zn, Mn, and Se for the samples that were shipped and later processed.

3.2. SAMPLE PREPARATION AND ANALYSIS

Major cations (Na, Ca, Mg, K, Sr, and Fe) and some elements that form anions (e.g., P and B) were analyzed in diluted samples (100 to 1000 times) using matrix-matched standards on a Perkin Elmer©Avio 200 ICP-OES instrument in the Center for Research in Energy and the Environment at Missouri S&T. Trace elements (Al, V, Cr, Co, Ni, Cu, Zn, As, Se, Mo, Cd, Pb, Tl, Mn, Ba) were analyzed in diluted samples (1000 times) on a Perkin Elmer©NexION 300 ICP-MS instrument. Major anions (Cl, SO4, and Br) were analyzed in similarly diluted samples using a Dionex© IC instrument. Concentrations of HCO3 were determined using titration via Bromocresol Green and Methyl Red. Dissolved organic species were not analyzed in this study. Uncertainties for ICP and IC analyses were around ± 15% (calculated from replicate analyses of samples that underwent different dilutions). This level of uncertainty is primarily attributable to the large dilution factors needed to analyze these highly saline waters. The charge imbalances for all the wells ranged from +7.3% to -19.7%, with an average of -8.3%. The slight bias towards anions is likely attributable to small uncertainties in dilution volumes, as sample sets analyzed for cations and anions were prepared and diluted separately.

4. RESULTS AND DISCUSSION

Produced waters from the TMS are highly saline Na-Ca-Cl brines with concentrations of total dissolved solids ranging from 10.9 to 22.7 wt% (based on summing the weight percentages from the measured major cations and anions). The pH of the samples measured in the field ranged from 5.5 to 5.9. Dissolved organic species were not analyzed in this study. The results for all chemical analyses are summarized in Table S-1 in the electronic supplemental material.

4.1. MAJOR IONS

Box plots of the major anions and cations are presented in Figure 3. The dominant anion in all samples was Cl with concentrations ranging from 71 to 156 g/L with a mean of 103 g/L for all wells (Figure 3). The interquartile range for concentrations of Cl for all wells was 83 g/L to 115 g/L, indicating that most data clustered over a modest range. Concentrations of Br ranged from 0.77 to 1.4 g/L with a mean of 1.0 g/L, and carbonate alkalinity (as HCO3) ranged from 0.04 to 0.38 g/L. Only a handful of samples had concentrations of sulfate above the detection limit of 0.50 g/L, which was due to the large dilution factors (Table S1).

The dominant cation in the samples was Na with concentrations ranging from 29 to 48 g/L with a mean of 40 g/L, while concentrations of Ca ranged from 4.9 to 18.4 g/L with a mean of 11.8 g/L (Figure 3). As with the Cl data, the interquartile ranges for Na and Ca were both relatively narrow, ranging from 34.8 to 45.1 g/L and 8.8 to 15.7 g/L, respectively. Concentrations of Mg, Sr, and K were slightly lower, ranging from 0.46 to

1.4 g/L (mean 1.00 g/L), 0.09 to 0.86 g/L (mean 0.60 g/L), and 0.43 to 0.96 g/L (mean 0.68 g/L), respectively. Iron and Ba are also reported with the major cations, as their concentrations were substantially higher than other trace elements. Concentrations of Fe ranged from 0.07 to 0.27 g/L, while concentrations of Ba ranged from 0.02 to 0.14 g/L (Figure 3).

The log concentrations of Cl are plotted versus the log concentrations of major cations and selected element ratios in Figure 4. Available chemical data for flowback water were provided by the well operator for an additional well completed in the TMS in

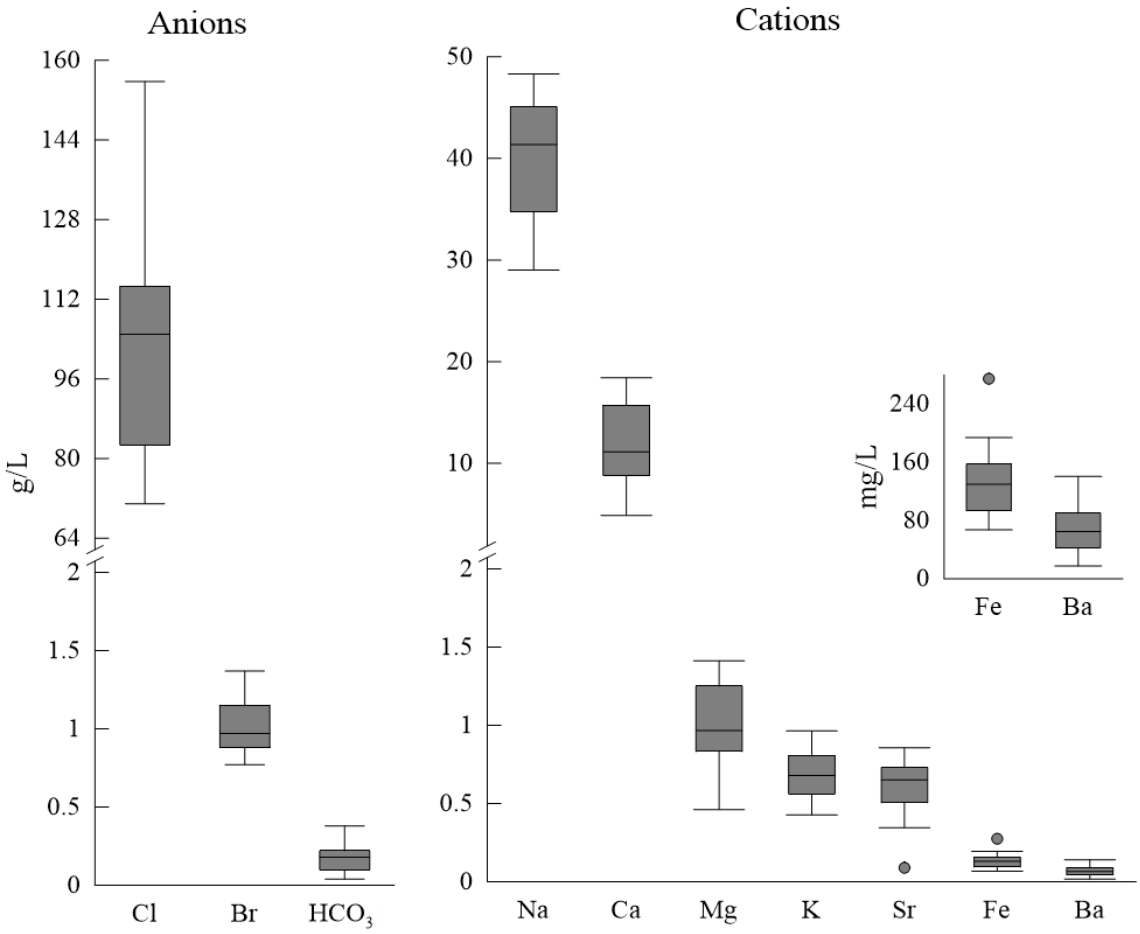

Figure 3. Box plots of concentrations of major anions and cations in produced waters from the TMS. Concentrations for SO4 are not included, as they were largely below detection (Table S1).

close proximity to the wells sampled here (Table S1). The chemical data from the flowback waters from this well are plotted for comparison in Figure 4. Flowback samples were collected after two days (Stage 1) and after one week (Stage 2) of the start of production. All the major cations are positively correlated with Cl (Figure 4). The flowback water has an initial dilute composition that within one week begins to approach the concentrations of major ions in the currently producing wells. This rapid transition toward the formation water endmember composition occurs despite the fact that only a small fraction of the fracking water volume was returned. This suggests that in addition to water-rock interactions, the highly-saline formation waters are rapidly exchanging with the more dilute fracking water. This behavior is consistent with observations from a number of other investigations (Haluszczak et al. 2013; Kim et al. 2016; Kondash et al. 2017; and Vengosh et al. 2017). For example, Haluszczak et al. 2013 showed that flowback water from Marcellus gas wells rapidly changed to a brine composition and suggested that less than 25% of the fracking water composition was represented in the returned brine after only two to three weeks.

The ratios of K/Na and Ca/Na in the produced waters of the TMS also increase with increasing concentrations of Cl (Figure 4). This pattern fits a scenario where the brine endmember (with the greatest amount of Cl) is progressively diluted with water of a relatively low TDS content with lower Ca/Na and K/Na ratios (Figure 4). The likely source for the dilute water endmember is the original fracking fluid. However, as all the wells in our study have been producing oil, gas, and water for at least 2.5 years (Table S1), this would mean that the fracking fluid signature persists in the TMS for a longer period of time than has been suggested in some previous investigations (Kim et al. 2016;

Kondash et al. 2017). Without additional isotopic data we also cannot rule out the possible presence of connate waters or meteoric waters from other sources (that are dilute relative to the brine endmember) in the TMS.

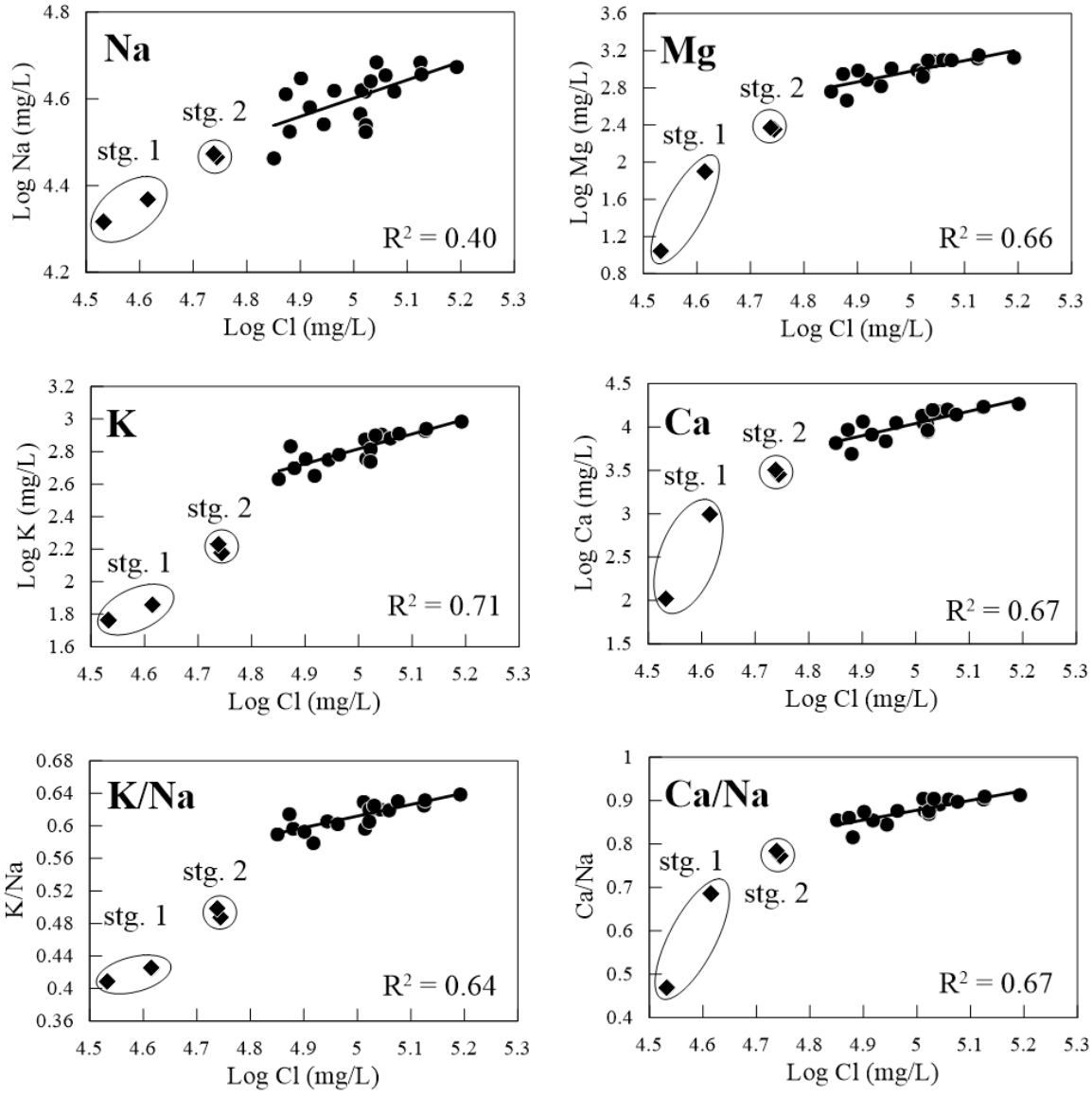

Figure 4. Log concentrations of chloride versus log concentrations of major elements and key elemental ratios of major cations (closed circles). Best-fit trendlines for these data are provided with R2 correlation coefficients. Chemical data from flowback two days (stage 1) and one week (stage 2) after production are shown in closed diamonds.

4.2. TRACE ELEMENTS

Measured concentrations of selected trace elements are presented in Figure 5. Boron exhibited the highest average concentration, with an interquartile range of 14.2 to 16.4 mg/L and a mean of 15.8 mg/L. Concentrations of Mn were widely variable among the well samples, with an interquartile range of 3.9 to 18.8 mg/L and a mean of 11.9 mg/L. Concentrations of Cu were high relative to reported concentrations in similar studies, with a mean of 9.3 mg/L and an interquartile range of 7.4 to 11.0 mg/L. Concentrations of P and Zn averaged 2.52 mg/L and 0.29 mg/L, respectively. All the other elements exhibited average concentrations of less than 1 mg/L (Figure 5).

The log concentrations of TDS are plotted versus the log of the concentrations of trace elements in Figure 6. For consistency in comparison, correlations are considered “strong”, “moderate”, or “absent to weak” if the respective R2 values fall within in the ranges of 1 to >0.6, 0.6 to >0.3, or 0.3 to 0. Many of the trace elements, including Zn, Tl, As, Mn, Ni, V, Co, and Pb exhibited moderate or strong positive correlations with TDS. As the total solute content of a brine increases relative to the total water content, the concentrations of all the individual solutes increases, which can also result in positive correlations among the individual elements (Engle et al., 2016). Therefore, the correlations shown here are best used as general indicators of relationships with TDS, such as which constituents are related to the brine itself and which are not. For example, a positive correlation with TDS probably does suggest that these elements were not contaminants introduced during well construction or hydraulic fracking activity, but are associated with the natural brine compositions. The strong affinity for many transition

metals to complex with Cl also increases the solubilities of many of these elements (e.g., Kharaka et al.,1987; Bebie et al., 1998; Borrok et al., 2008; Kamenetsky et al., 2016).

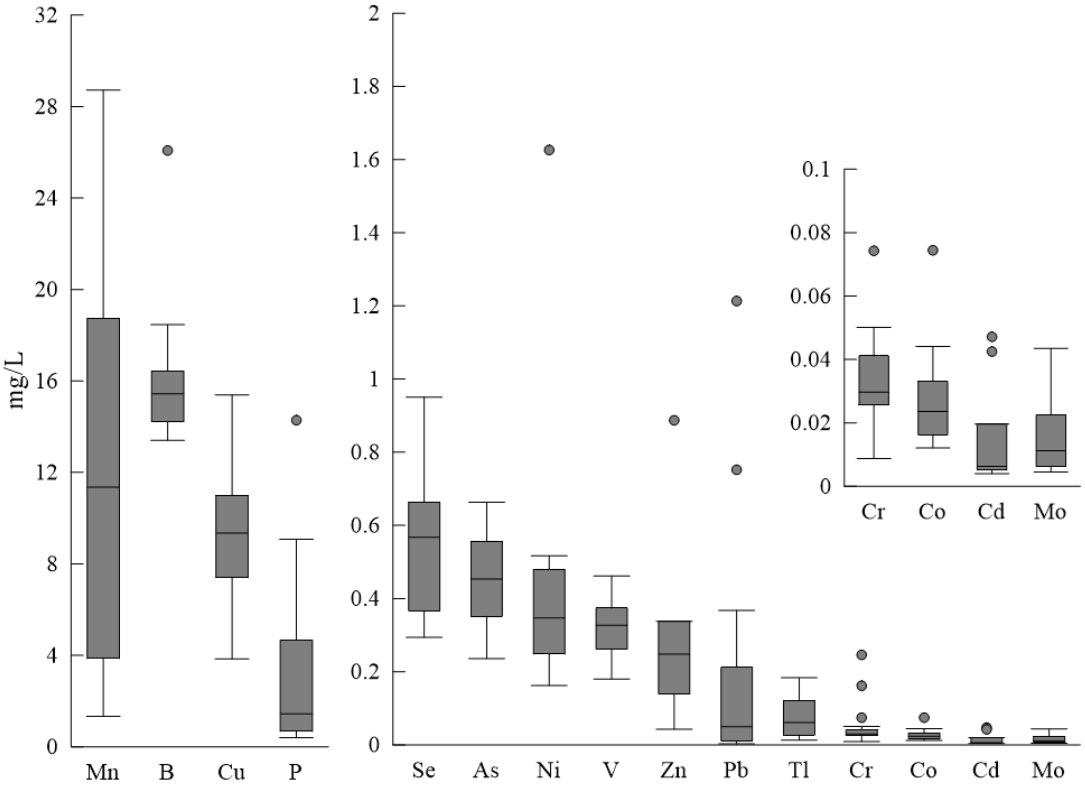

Figure 5. Box plots of the concentrations of trace elements in produced waters from the TMS. Concentrations of Cd and Mo are included only for wells where concentrations of these elements were greater than detection limits (Table S1). Zn has one additional outlier at 6.41 mg/L (not on graph).

Conversely, concentrations of Cu, Cd, Se, B, Mo, Cr, and P show absent or weak correlations with TDS (Figure 6). The reasons for the lack of correlation with TDS for these elements is uncertain, but it could be related to how quickly they equilibrate within the fluid, or it is feasible some amounts of these constituents were introduced during the fracking process. Phosphorous, for example, is a common constituent in many fracking fluids (e.g. Haluszczak et al., 2013).

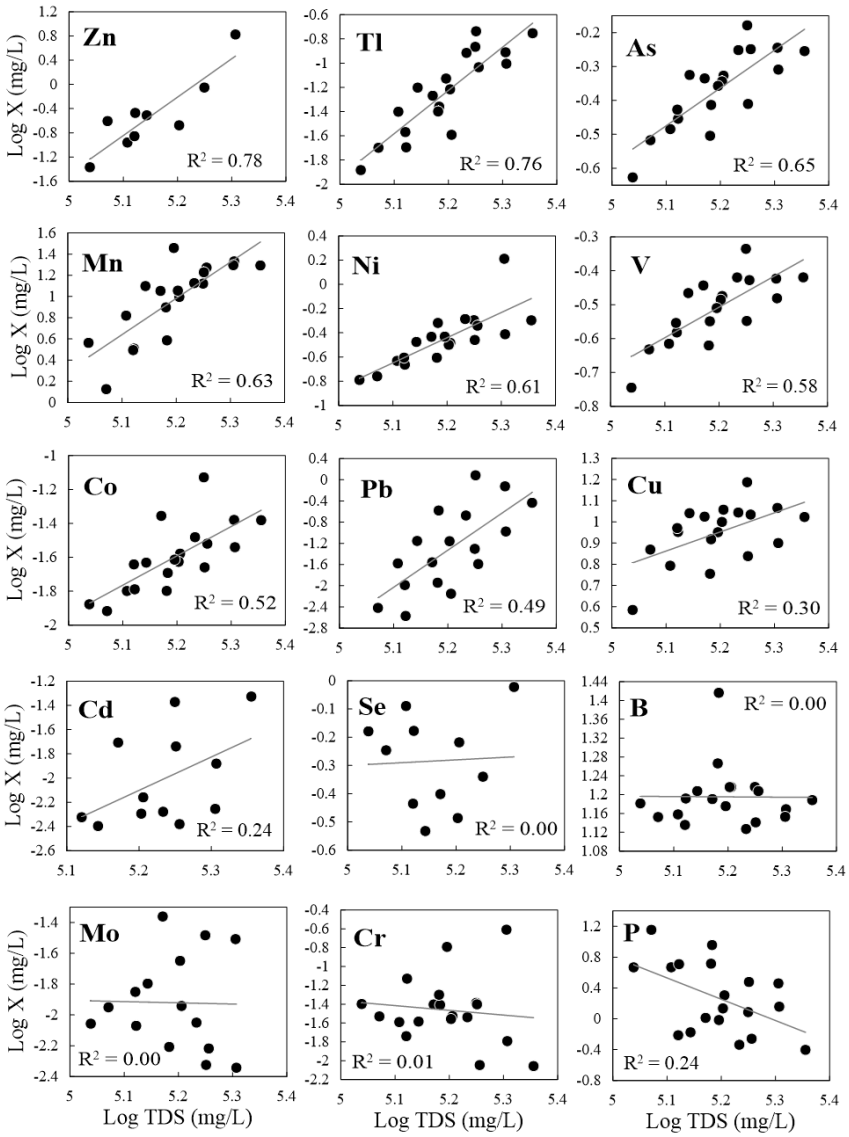

Figure 6. Log concentrations of trace elements versus log concentrations of TDS.

4.3. RELATIONSHIPS WITH OIL AND WATER PRODUCTION

Figure 7 presents a comparison of the TDS of produced waters relative to the Produced Oil Volume (POV), Produced Water Volume (PWV), and the ratio of Produced Water Volume to Fracking Water Volume (PWV/FWV) for each well. The concentrations of TDS are not well-correlated with oil production, but do exhibit moderate correlations with the total PWV and the PWV/FWV ratio. These relationships

are consistent with the hypothesis that the endmember formation water composition within the TMS has been diluted with varying amounts of the fracking fluid. In this scenario we would expect to see more of the formation water signature with more PWV and larger PWV/FWV ratios. The time of production for TMS wells is not well correlated with the PWV/FWV ratio (Table S1). This suggests that additional factors such as changes in the lengths and styles of horizontal completions, the quality and extent of fracking, and perhaps the existence of pre-existing fracture networks all play a role in controlling the PWV in TMS wells.

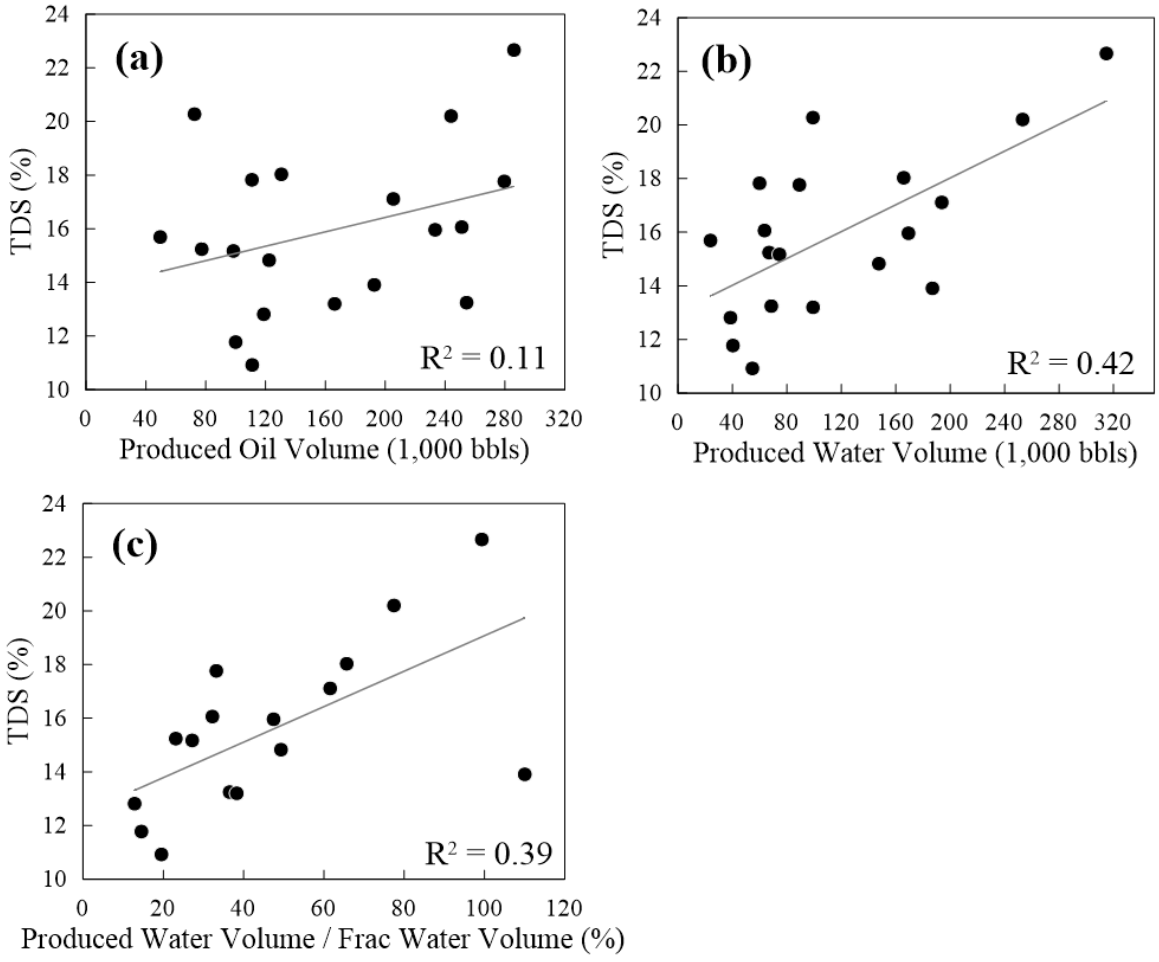

Figure 7. Correlation plots comparing TDS with (a) POV, (b) PWV, and (c) PWV/FWV for the TMS samples.

Most major elements exhibited a moderate (Cl, Na, Ca, Sr) or weak (Mg, K, Fe) correlation with PWV (Table S1). Trace elements tended to have absent to weak correlations with PWV except for Se, As, and V, which exhibited moderate correlations (Table S1). The correlation with Se and PWV was negative, while As and V correlations with PWV were positive. This further suggests that concentrations of Se are not linked to the formation water brine within the TMS, but could be released during the fracking process.

Most major and trace elements exhibited only weak or absent correlations with POV. Both Cu (0.45 R2) and V (0.30 R2) exhibited moderate correlations with POV, while no elements exhibited a strong correlations (Table S1). This could suggest that the richness of the hydrocarbon system itself is somehow related to the amount of Cu and possibly V in the produced water. If so, one reason for this may be that more oil production could be related to the presence of greater amounts of total organic carbon and kerogen in the TMS. Copper and some other trace elements such as V are frequently sequestered in organic complexes within the kerogen (Chaplin and Dunning, 1960; Jagtap and Ramaswamy, 2006; Premovic et al., 2007; Pushie et al. 2014). These element could make their way into the associated formation waters. Alternatively, concentrations of dissolved Cu and V in our study could reflect the presence of small amounts of oil that passed through the 0.45 micron filters used in our investigation. In this scenario, increases in the POV could be related to the effectiveness of the sampling procedure and not necessarily the richness of the hydrocarbon system.

4.5. RELATIONSHIPS WITH OTHER PRODUCED WATERS IN THE GULF COAST BASIN

Produced water data from the TMS were compared to historical produced water data mined from the USGS produced waters database from regions in and around the Mississippi Salt Basin (MSB; Figure 8). Specifically, we limited our comparison to data within the region located in and between the MSB to the northeast, the North Louisiana Salt Basin to the northwest and the South Louisiana Salt Basin to the south (Figure 8). The data included produced water samples from nine geological units ranging in age from Jurassic to Tertiary. Plots of well depth versus the log concentration of Cl and K/Na and Ca/Na ratios of these fluids are presented in Figure 9. The results show a gross correlation of increasing concentrations of Cl as a function of increasing well depth (Figure 9). This observation is consistent with most previous observations in that the salinity of formation waters in sedimentary basins tends to increase with increasing depth due in part to increases in solubility and the kinetics of water-rock interactions with increasing temperature (e.g. Kharaka and Hanor, 2003; Lu et al., 2017). Similar trends suggestive of progressive water-rock interaction with depth (and often within individual formations) seem evident in the K/Na and Ca/Na ratios (Figure 9). The K/Na ratios tend to increase with increasing depth in a roughly uniform fashion for all samples except those in the Jurassic Smackover Formation. This is likely attributable to differences in the mineralogical properties of the geological units, as all of the Tertiary and Cretaceous units are dominated by siliciclastic rocks, while the Smackover Formation is limestone. The K/Na ratio in the clastic rocks is likely controlled by the balance of alteration of K-bearing feldspars relative to the formation of illite. The limestone in the Smackover probably does not support the formation of much illite so the concentration of K in the

brine remains higher. Although there is little change in the Ca/Na ratios in the shallower formations, overall the ratios of Ca/Na tend to increase in the deeper units. This variation with depth, and within some of the individual formations is likely related to increasing water-rock interaction via dolomitization and albitization, which respectively result in the release of more Ca and the sequestration of Na (e.g., Land and Prezbindowski, 1981; Kharaka and Hanor, 2003; Houston et al., 2007). This also results in fluids evolving from Na-Cl waters to Na-Ca-Cl waters deeper in the basin.

All samples from our study and the produced waters database where both Cl and Br data were available are plotted on a log Cl vs. log Br graph in Figure 10. This plot provides a good indication of the origin of the brines, and suggests that all the samples (excepting the two from the Sparta Formation) are derived from the bitterns of progressively evaporated seawater. This is also the conclusion from previous investigations of produced waters and brines in the MSB basin (e.g., Carpenter et al., 1974; Land and Prezbindowski, 1981; Kharaka et al., 1987; and Hanor and McIntosh, 2007). These studies suggest that the bitterns were likely associated with the precipitation of the Late Jurassic Louann Salt and that these fluids were likely expelled from pore spaces during sediment loading. This is a meaningful observation for our study in that it suggests that formation waters derived from evaporated seawater were able to migrate through the TMS unit. It is also possible that fractures in the TMS (either pre-existing or induced during fracking) served as conduits for the brine migration. However, if this

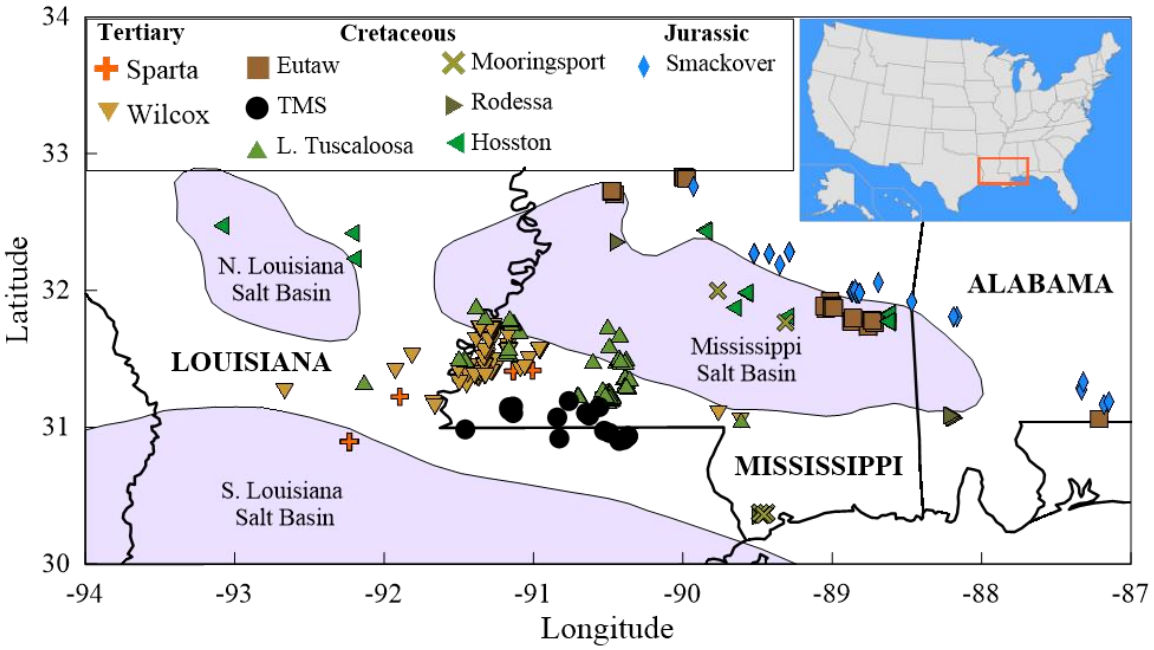

Figure 8. Regional map of wells with produced water data available from the USGS database and this study. Wells are identified by the geologic unit in which they were completed.

were the case we would expect the volume of water produced in the TMS to be much higher.

The TMS samples in Figure 10 fall along lines of mixing between the bitterns and more dilute seawater or freshwater. An important dilute endmember in the case of the TMS samples is most likely the water used for the fracking process. Kharaka et al. (1987) suggested that some mixing of the bitterns with meteoric fluids had occurred in samples collected from the adjacent formations, although it is less than the extent of dilution seen for the TMS samples. For example, the Cl and Br data suggest that the brine endmember in the TMS is diluted by up to 75% by more dilute fluids, whereas the percentages of dilution for produced waters in other formations is less (usually <50%; Figure 10). The additional dilution in the TMS samples is best explained by the presence of fracking

fluids. Other sources of dilute fluids make less sense, as it would be unreasonable to expect that a tight shale formation such as the TMS enabled a mixing pathway for more dilute fluids that was not also reflected in the more permeable reservoir rocks

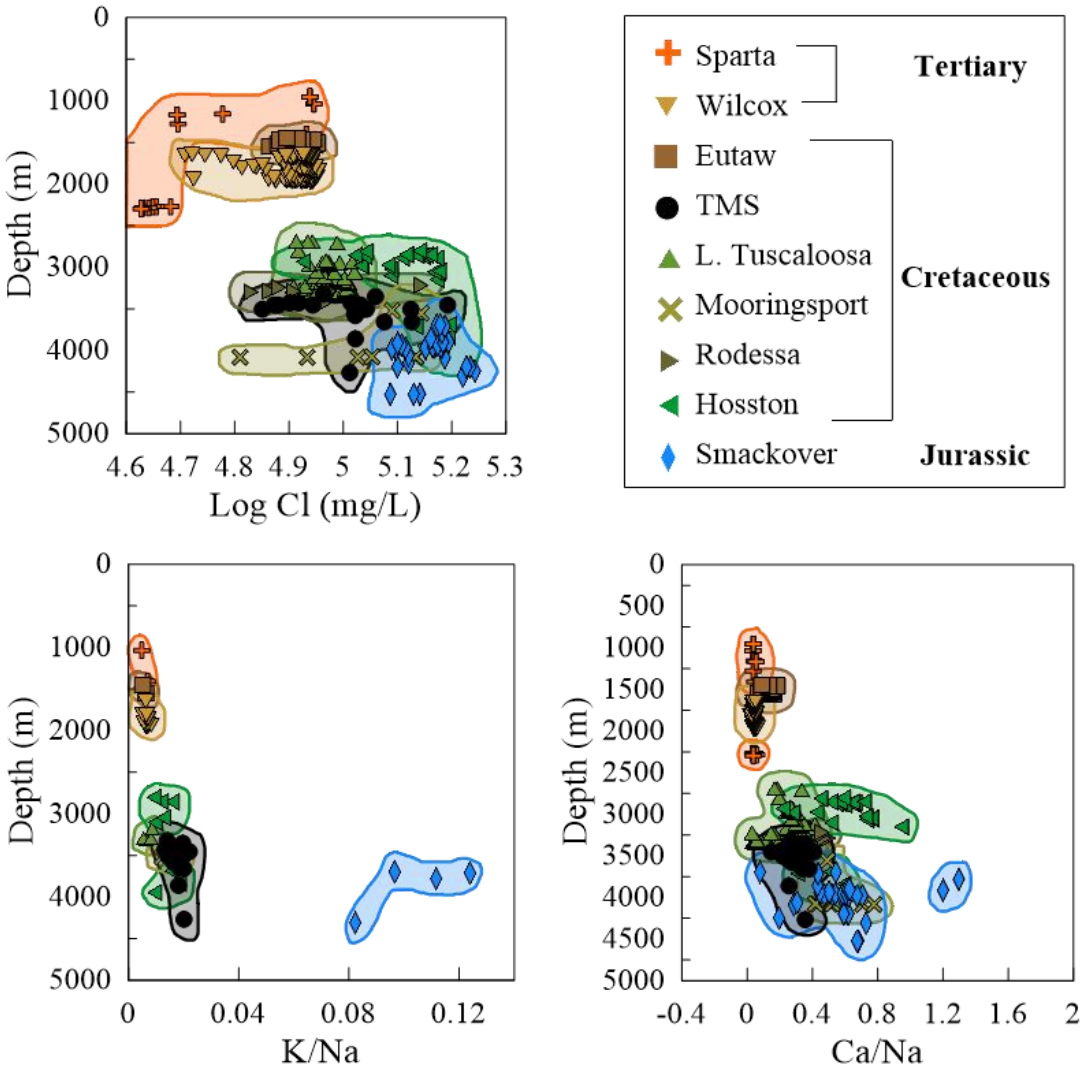

Figure 9. Graphs illustrating the relationships between well depth and the chemistry of produced waters for TMS samples and historical data from the USGS produced waters database. One sample from the Smackover formation with a Ca/Na ratio of 3.6 is not shown.

surrounding the TMS. We cannot, however, rule out the possibility that some lower salinity connate water that may have been trapped in the TMS could plays a role.

Samples from the Tertiary Sparta Formation plot to the left of the seawater evaporation line, indicating that salts in these samples were derived largely from the dissolution of NaCl, perhaps from nearby salt domes. One sample from the upper Cretaceous Eutaw Formation is shifted to the left of the mixing line of bitterns and more dilute water, suggesting this sample may also have been impacted by the dissolution of NaCl salts.

Previous studies have additionally reported high concentrations of metals such as Zn and Pb in some of the brines within the MSB (e.g., Carpenter et al. 1974 and Kharaka et al. 1987). Figure 11 compares the concentrations of Zn and Pb measured in our studies with these previous observations. Of the geologic units with sample data not previously described above, the Cotton Valley Group of Upper Jurassic age is predominately comprised of sandstone and conglomerates with inter bedded shales, mudstones and rare limestone (Kharaka et al., 1987). The Paluxy and Washita Formations of Lower Cretaceous ages are dominantly red and grey shales (Kharaka et al., 1987). The TMS tends to have much lower concentrations of Zn and Pb relative to most of the other formations in the basin (Figure 11). Concentrations of Zn are low (< 48 mg/L) in our samples and in the units from the Upper Jurassic period, but increase in the units of Cretaceous age, spiking at 367 mg/L in the Hosston Formation (Figure 11). Concentrations of Pb are roughly one third those of Zn but follow the same trend. Both previous studies attribute the high concentrations of Pb and Zn to leaching of metal-rich marine shales in environments with low amounts of H2S, such that the solubility of

sulfide minerals in the presence of large amounts of Cl is significantly increased. This suggests that brines with relatively low concentrations of Pb and Zn in the Smackover and TMS formations are reducing, with some H2S, while the fluids in many of the Cretaceous-age units with higher dissolved metal contents may have been more oxidizing. One possibility for this observation could be the presence of oxidized iron minerals in the Cretaceous red-gray shales that are absent in the TMS and Smackover. These minerals could have helped to support the oxidation of sulfide minerals.

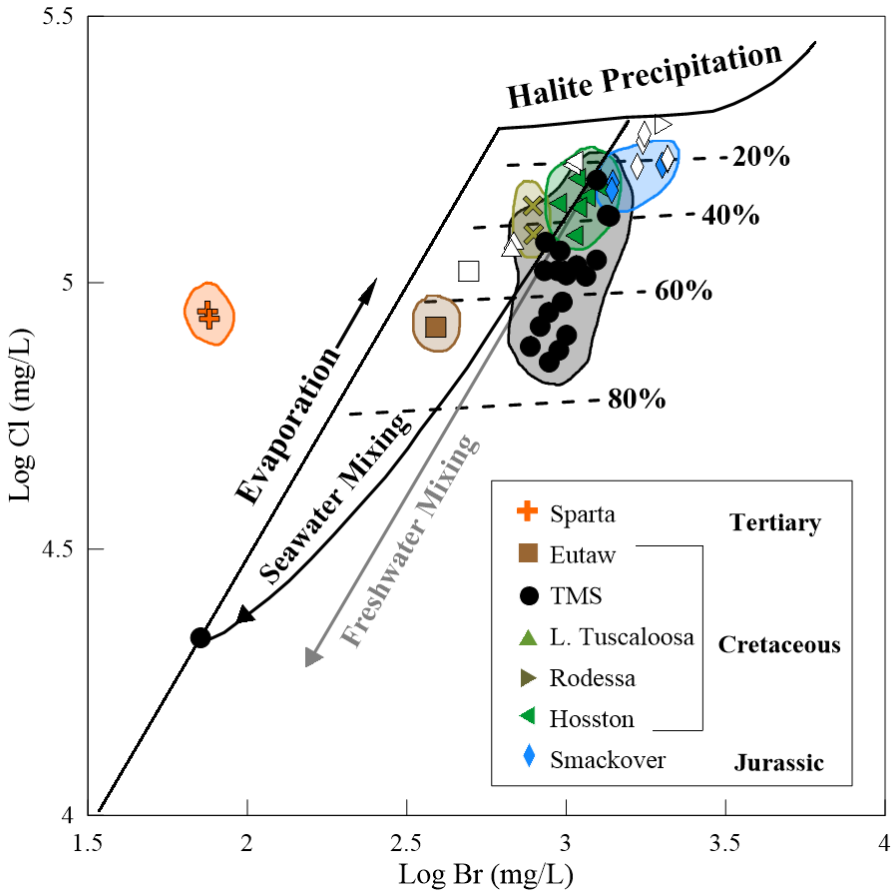

Figure 10. Log Cl vs. Log Br graph of the TMS samples, available samples from the USGS produced waters database, and data from Kharaka et al., 1987. Superimposed are lines showing the evaporation trend for seawater and possible mixing lines of bitterns with seawater and freshwater. Data from Kharaka et al. (1987) are retain the symbol shape of the relevant geologic unit but are colored white.

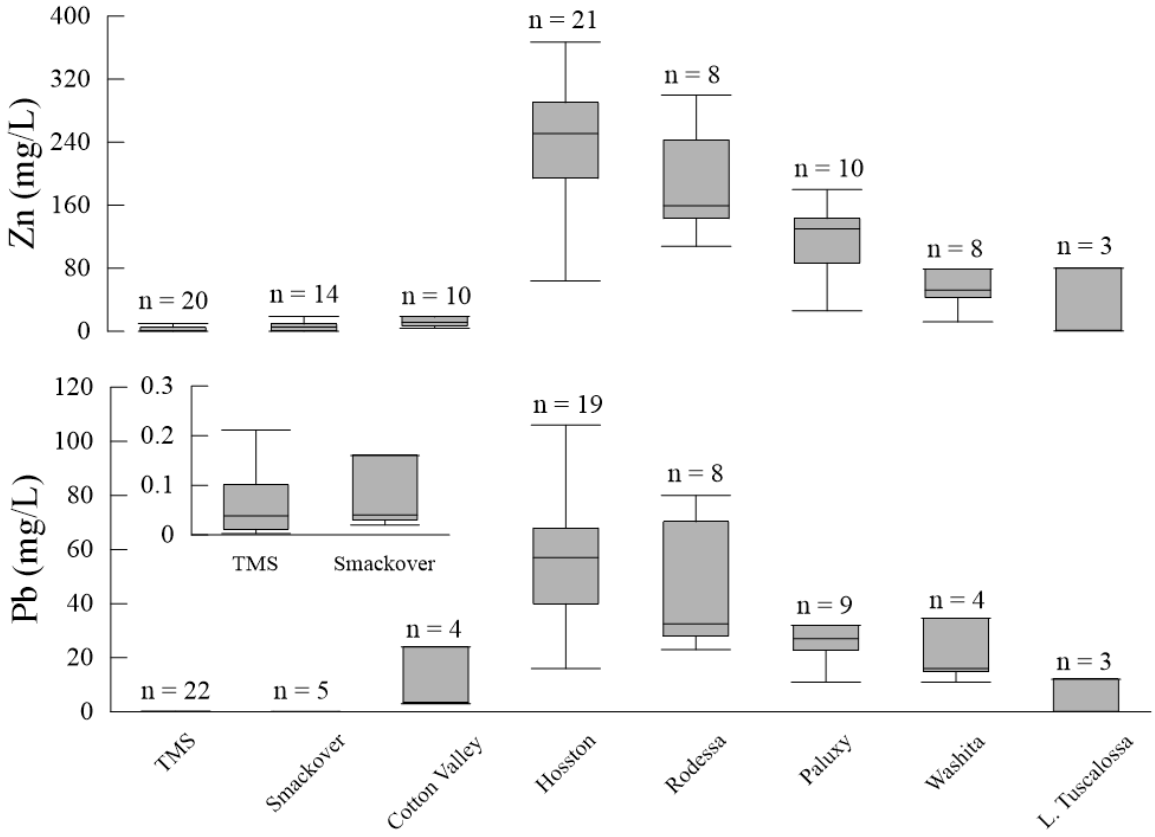

Figure 11. Box plots showing the concentrations of Zn and Pb in the TMS and various geologic units from the MSB (Carpenter et al., 1974 and Kharaka et al., 1987).

5. CONCLUSIONS

The produced waters of the TMS are highly-saline Na-Ca-Cl brines that are typical of those found in other geologic units within the Gulf of Mexico Basin. The TMS brines, however, are substantially diluted by less saline water sources, including the fracking water used in the completion of the wells. This influence of fracking water is reasonable given that the volume of water produced from all but one well is less than the volume of water used to frack that well. Moreover, the concentrations of TDS in the produced waters exhibit a moderate correlation with increases in PWV and the

PWV/FWV ratio, showing that the fluids approach the brine formation water endmember as more water is returned. The relatively small volumes of produced water for TMS wells also suggests that the TMS is a tight formation that allows for limited fluid flow over short time scales. However, it is also clear from Br and Cl systematics that the produced waters in the TMS are likely derived from Jurassic-age evaporated seawater. This suggests that brine fluids have migrated through the TMS over geologic time periods despite its low present-day permeability.

Trace elements that exhibited strong (Zn, Tl, As, Mn, Ni) or moderate (V, Co, Pb, Cu) correlations with TDS are likely more abundant in the brine endmember and were not introduced in large amounts during the fracking process. Whereas, elements that exhibited weak (Cd), absent (Se, B, Mo, Cr), or inverse correlations (P) with TDS may have been derived from other sources or processes, including fracking. Major elements exhibited moderate (Na, Ca, Sr, Cl) or weak (Mg, K, Fe) correlations with the PWV. Whereas, correlations of most trace elements with the PWV were weak or absent except for Se, As, and V. Moderate correlations for both As and V were positive, while the moderate correlation for Se was negative. The concentrations of Cu and V were moderately correlated with POV, suggesting a link between these elements and organic complexes in the hydrocarbon system. All other major and trace element exhibited weak or no correlations with POV. The concentrations of Zn and Pb in the TMS were lower than those found in produced waters previously described from surrounding formations. This observation may hint at differences in metal availability and redox conditions among the different basin strata.

ACKNOWLEDGMENTS

This manuscript was improved greatly through the suggestions of two anonymous reviewers. Kevin Gibbs and Darrell Knight of the Goodrich Petroleum Company were instrumental in the collection of the produced waters and Audrey Thompson (Missouri S&T) helped with collection of the field samples. This material is based upon work supported by the Department of Energy National Energy Technology Laboratory under Award Number DE-FE0031575 (TUSCALOOSA MARINE SHALE LABORATORY). Disclaimer: This report was prepared as an account of work sponsored by an agency of the United States Government. Neither the United States Government nor any agency thereof, nor any of their employees, makes any warranty, express or implied, or assumes any legal liability or responsibility for the accuracy, completeness, or usefulness of any information, apparatus, product, or process disclosed, or represents that its use would not infringe privately owned rights. Reference herein to any specific commercial product, process, or service by trade name, trademark, manufacturer, or otherwise does not necessarily constitute or imply its endorsement, recommendation, or favoring by the United States Government or any agency thereof. The views and opinions of authors expressed herein do not necessarily state or reflect those of the United States Government or any agency thereof.

REFERENCES

Allen Jr., J.E., Meylan, M.A., and Heitmuller, F.T., 2014. Determining hydrocarbon distribution using resistivity, Tuscaloosa Marine Shale, Southwestern Mississippi. Gulf Coast Association of Geological Societies Transactions, 64, 41-57.

Alley, B., Beebe, A., Rodgers Jr., J., and Castle, J.W., 2011. Chemical and physical characterization of produced waters from conventional and unconventional fossil fuel resources. Chemosphere, 85, 74-82. https://doi.org/10.1016/j.chemosphere.2011.05.043.

Barbot, E., Vidic, N.S., Gregory, K.B., and Vidic, R.D., 2013. Spatial and temporal correlation of water quality parameters of produced waters from Devonian-age shale following hydraulic fracturing. Environmental and Science Technology, 47 (6), 2562-2569. https://doi.org/10.1021/es304638h.

Barnaby, R.J., Oetting G.C., and Gao, G., 2004. Strontium isotopic signatures of oil-field waters: Applications for reservoir characterization. American Association of Petroleum Geologists

Bulletin, 88, 1677-1704. https://doi.org/10.1306/07130404002.

Bebie, J., Seward, T.M., and Hovey, J.K., 1998. Spectrophotometric determination of the stability of thallium (I) chloride complexes in aqueous solution up to 200°C. Geochimica et Cosmochimica Acta, 62 (9), 1643-1651. https://doi.org/10.1016/S0016-7037(98)00084-2.

Blondes, M.S., Gans, K.D., Engle, M.A., Kharaka, Y.K., Reidy, M.E., Saraswathula, V., Thordsen, J.J., Rowan, E.L., and Morrissey, E.A., 2018. U.S. Geological Survey National Produced Waters Geochemical Database (ver. 2.3n): U.S. Geological Survey data release, https://doi.org/10.5066/F7J964W8. (Accessed 22 December 2018).

Blum, M.D., Milliken, K.T., Pecha, M.A., Snedden, J.W., Frederick, B.C., and Galloway, W.E., 2017. Detrital-Zircon records of Cenomanian, Paleogene, and Oligocene Gulf of Mexico drainage integration and sediment routing: Implications for scales of basin-floor fans. Geosphere, 13 (6), 2169-2205. https://doi.org/10.1130/GES01410.1.

Borrok, D.M., Nimick, D.A., Wanty, R.B., and Ridley, W.I., 2008. Isotopic variations of dissolved copper and zinc in stream waters affected by historical mining. Geochimica et Cosmochimica Acta, 72 (2), 329-344. https://doi.org/10.1016/j.gca.2007.11.014.

Borrok, D.M., Yang, W., Wei, M., and Mokhtari, M., 2019. Heterogeneity of the mineralogy and organic content of the Tuscaloosa Marine Shale. Marine and Petroleum Geology 109, 717-731. https://doi.org/10.1016/j.marpetgeo.2019.06.056.

Carpenter, A.B., Trout, M.L., and Pickett, E.E., 1974. Preliminary report on the origin and chemical evolution of lead and zinc-rich oil field brines in Central Mississippi. Economic Geology, 69, 1991-1206. https://doi.org/10.2113/gsecongeo.69.8.1191.

Chaplin, J.B.F., and Dunning, H.N., 1960. A geochemical investigation of the Athabasca bituminous sands. Economic Geology, 55 (4), 797-804. https://doi.org/10.2113/gsecongeo.55.4.797.

Clark, C.E., and Veil, J.A., 2009. Produced water volumes and management practices in the United States, ANL/EVS/R-09/1. Prepared for the U.S. Department of Energy, National Energy Technology Laboratory, September, 64 pp.

Engle, M.A., Reyes, F.R., Varonka, M.S., Orem, W.H., Ma, L., Ianno, A.J., Schell, T.M., Xu, P., and Carrol, K.C., 2016. Geochemistry of formation waters from the Wolfcamp and "Cline" shales: Insights into brine origin, reservoir connectivity, and fluid flow in the Permian Basin, USA. Chemical Geology, 425, 76-92. https://doi.org/10.1016/j.chemgeo.2016.01.025.

Enomoto, C.B, Hackley, P.C., Valentine, B.J., Rouse, W.A., Dulong, F.T., Lohr, C.D., and Hatcherian, J.J., 2017. Geologic characterization of the hydrocarbon resource potential of the Upper Cretaceous Tuscaloosa Marine Shale in Mississippi and Louisiana, U.S.A., Gulf Coast Association of Geological Societies Transactions article #00193, 67, 95-109.

Fritz, S.J., 1986. Ideality of clay membranes in osmotic processes: A review. Clays and Clay Minerals, 34, 214-223. https://doi.org/10.1346/CCMN.1986.0340212.

Galloway, W.E., 2008. Depositional evolution of the Gulf of Mexico sedimentary basin, in: K.J. Hsu and A.D. Miall, (Eds.), The Sedimentary basins of the United States and Canada: Elsevier, pp. 505-549

Hackley, P.C., Garza, D., Valentine, B.J., Enomoto, C.B., Lohr, C.D., Hatcherian, J.J., Dulong, F.T., and Dennen, K.O., 2017. Is the Tuscaloosa marine shale self-sourced? Preliminary oil-oil and oil-source rock correlation studies in the Upper Cretaceous Tuscaloosa Group, Southern Mississippi, USA. American Association of Petroleum Geologist Search and Discovery Article 90921, Tulsa, Oklahoma, 1 p.

Haluszczak, L.O., Rose, A.W., and Kump, L.R., 2013. Geochemical evaluation of flowback brine from Marcellus gas wells in Pennsylvania, USA. Applied Geochemistry, 28, 55-61. https://doi.org/10.1016/j.apgeochem.2012.10.002.

Hanor, J.S. and McIntosh, J.C., 2007. Diverse origins and timing of formation of basinal brines in the Gulf of Mexico sedimentary basin. Geofluids, 7 (2), 227-237. https://doi.org/10.1111/j.1468-8123.2007.00177.x.

Houston, S.J., Yardley, B.W.D., Smalley, P.C., and Collins, I., 2007. Rapid fluid-rock interaction in oilfield reservoirs. Geology, 35 (12), 1143-1146. https://doi.org/10.1130/G24264A.1.

Hudec, M.R., Jackson, M.P.A., and Peel, F.J., 2013. Influence of deep Louann structure on the evolution of the northern Gulf of Mexico. American Association of Petroleum Geologists Bulletin, 97 (10), 1711-1735. https://doi.org/10.1306/04011312074.

Humphris, Jr., C.C., 1979. Salt movement on the continental slope, Northern Gulf of Mexico. American Association of Petroleum Geologists Bulletin, 63 (5), 782-798. https://doi.org/10.1306/St7399C4.

Jagtap, N., and Ramaswamy, V., 2006. Encapsulation of Co phthalocyanine in alumina pillared clays and their characterization. Clays and Clay Minerals, 54 (1), 54-61. https://doi.org/10.1346/CCMN.2006.0540107.

John, C.J., Jones, B.L., Moncrief, J.E., Bourgeois, R., and Harder, B.J., 1997. An unproven unconventional seven billion barrel oil resource - the Tuscaloosa Marine Shale: Louisiana State University Basin Research Institute Bulletin 7, Baton Rouge, 22 p.

Kamenetsky, V.S., Lygin, A.V., Foster, J.G., Meffre, S., Maas, R., Kamenetsky, M.B., Goemann, K., and Beresford, S.W., 2016. A story of olivine from the McIvor Hill complex (Tasmania, Australia): Clues to the origin of the Avebury metasomatic Ni sulfide deposit. American Mineralogist, 101 (6), 1321-1331. https://doi.org/10.2138/am-2016-5509.

Kharaka, Y.K., and Smalley, W.C., 1976. Flow of water and solutes through compacted clays. American Association of Petroleum Geologists Bulletin, 60 (6), 973-980. https://doi.org/10.1306/C1EA35F0-16C9-11D7-8645000102C1865D.

Kharaka, Y.K., Maest, A.S., Carothers, W.W., Law, L.M., Lamothe P.J., and Fries, T.L., 1987. Geochemistry of metal-rich brines from central Mississippi Salt Dome Basin, U.S.A. Applied Geochemistry, 2, 543-561. https://doi.org/10.1016/0883-2927(87)90008-4.

Kharaka, Y.K., and Hanor, J.S., 2003. Deep fluids in the continents: I. Sedimentary Basins. Treatise on Geochemistry, 1-48. https://doi.org/10.1016/B0-08-043751-6/05085-4.

Kim, S., Omur-Ozbeck, P., Dhanasekar, A., Prior, A., and Carlson, K., 2016. Temporal analysis of flowback and produced water composition from shale oil and gas operations: Impact on frac fluid characteristics. Journal of Petroleum Science and Engineering 147, 202-210. https://doi.org/10.1016/j.petrol.2016.06.019.

Kondash, A.J., Albright, E., and Vengosh, A., 2017. Quantity of flowback and produced waters from unconventional oil and gas exploration. Science of the Total Environment. 574, 314-321. https://doi.org/10.1016/j.scitotenv.2016.09.069.

Land, L.S. and Prezbindowski, D.R., 1981. The origin and evolution of saline formation water, Lower Cretaceous carbonates, south-central Texas, U.S.A. in: W. Back and R. Le´tolle (Guest-Editors), Symposium on Geochemistry of Groundwater - 26th International Geological Congress. Journal of Hydrology, 54, 51-74. https://doi.org/10.1016/0022-1694(81)90152-9.

Lester, Y., Ferrer, I., Thurman, E.M., Sitterley, K.A., Korak, J.A., Aiken, G., and Linden, K.G., 2015. Characterization of hydraulic fracturing flowback water in Colorado: Implications for water treatment. Science of the Total Environment, 512-513, 637-644. http://dx.doi.org/10.1016/j.scitotenv.2015.01.043.

Liu, K., 2005. Upper Cretaceous Sequence Stratigraphy, Sea-level fluctuations and ocean anoxic events 2 and 3, Northeastern Gulf of Mexico. Stratigraphy, 2 (2), 147-266.

Lowery, C.M., Cunningham, R., Barrie, C.D., Bralower, T., and Snedden, J.W., 2017. The Northern Gulf of Mexico during OAE2 and the relationship between water depth and black shale development. Paleoceanography, 32 (12), pa003180. https://doi.org/10.1002/2017PA003180.

Lu, J., Mickler, P.J., Nicon, J., Choi, W., Esch, W.L., and Darvari, R., 2017. Geochemical interactions of shale and brine in autoclave experiments - Understanding mineral reactions during hydraulic fracturing of Marcellus and Eagle Ford Shales. American Association of Petroleum Geologists Bulletin, 101 (10), 1567-1597. https://doi.org/10.1306/11101616026.

Mancini, E.A. and Puckett, T.M., 2003. Integrated biostratigraphic and sequence stratigraphic approach for correlation and basin interpretation. Gulf Coast Association of Geological Societies Transactions, 53, 517-526.

Mancini, E.A., Obid, J., Badali, M., Liu, K., and Parcell, W.C., 2008. Sequence-stratigraphic analysis of Jurassic and Cretaceous strata and petroleum exploration in the central and eastern Gulf coastal plain, United States. American Association of Petroleum Geologists Bulletin, 92 (12), 1655-1686. https://doi.org/10.1306/08130808046.

Murray, G.E., 1947. Cenozoic deposits of Central Gulf Coastal Plain. American Association of Petroleum Geologists Bulletin, 31 (10), 1825-1850. https://doi.org/10.1306/3D933A5B-16B1-11D7-8645000102C1865D.

Premovic, P.I., Todorovic, B.Z., and Pavlovic, M.S., 2007. Cretaceous - Paleogene boundary Fish Clay at Højerup (Stevns Klint, Denmark): Trace metals in kerogen. Bulletin de la Societe Geologique de France, 178 (5), 411-421. https://doi.org/10.2113/gssgfbull.178.5.411.

Pushie, M.J., Pratt, B.R., McDonald, T.C., George, G.N., and Pickering, I.J., 2014. Evidence for biogenic copper (hemocyanin) in the middle Cambrian arthropod marrella from the Burgess Shale. Palaios, 29 (10), 512-524. http://dx.doi.org/10.2110/palo.2014.073.

Saller, A.H. and Steuber, A.M., 2018. Evolution or formation waters in the Permian Basin, United States: Late Permian evaporated seawater and Neogene meteoric water. American Association of Petroleum Geologists Bulletin, 102 (3), 401-428. https://doi.org/10.1306/0504171612517157.

Sherwood, J.D. and Craster, B., 2000. Transport of water and ions through a clay membrane. Journal of Colloid and Interface Science, 230 (2), 349-358. https://doi.org/10.1006/jcis.2000.7100.

Spooner Jr., H.V., 1964. Basal Tuscaloosa sediments, east-central Louisiana. American Association of Petroleum Geologists Bulletin, 48 (1), pp. 1-21.

Valentine, B.J., Hackley, P.C., Enomoto, C.B., Lohr, C.D., and Scholl, O.D., 2016. Preliminary evaluation of source rock potential and burial history of the Upper Cretaceous Tuscaloosa Marine Shale in Mississippi and Louisiana, U.S.A. American Association of Petroleum Geologists Search and Discovery Article 90259, 1 p.

Veil, J., 2012. U. S. produced water volumes and management practices in 2012. Prepared for the Ground Water Protection Council, Veil Environmental, LLC, April, 119 pp.

Vengosh, A., Jackson, R.B., Warner, N., Darrah, T.H., and Kondash, A., 2014. A critical review of the risks to water resources from unconventional shale gas development and hydraulic fracturing in the United States. Environmental and Science Technology, 48 (15), 8334-8348. https://doi.org/10.1021/es405118y.

Vengosh, A., Kondash, A., Harkness, J., Lauer, N., Warner N., and Darrah, T.H., 2017. The geochemistry of hydraulic fracturing fluids. Procedia Earth and Planetary Science, 17, 21-24. https://doi.org/10.1016/j.proeps.2016.12.011.

Wilhelm, O., and Ewing, M., 1972. Geology and history of the Gulf of Mexico. Geological Society of America Bulletin, 83 (3), 575-600. https://doi.org/10.1130/0016-7606(1972)83[575:GAHOTG]2.0.CO;2.

Zhang, Y., Gable, C.W., Zyvoloski, G.A., and Walter, L.M., 2009. Hydrogeochemistry and gas compositions of the Uinta Basin: A regional-scale overview. American Association of Petroleum Geologists Bulletin, 93 (8), 1087-1118. https://doi.org/10.1306/05140909004.

Werren, E.G., Shrew, R.D., Adams, E.R., and Stancliffe, R.J., 1990. Meander-belt reservoir geology, mid-dip Tuscaloosa, Little Creek Field, Mississippi, in: J.H. Barwis, J. G. McPherson and J. R. L. Studlick, (Eds.), Sandstone petroleum reservoirs: Springer-Verlag, New York, New York, p. 85-107.

Woolf, K.S., 2012. Regional character of the lower Tuscaloosa Formation depositional systems and trends in reservoir quality [unpublished Ph.D. thesis] Austin, The University of Texas at Austin, 241 pp. http://hdl.handle.net/2152/22071.

II. EXPERIMENTAL INVESTIGATION OF HIGH-TEMPERATURE BRINE-SHALE INTERACTIONS

Anna Hoffmann, David Borrok

Department of Geoscience and Geological and Petroleum Engineering, Missouri University of Science and Technology, Rolla, MO 65409

ABSTRACT

Water injection into the deep subsurface creates disequilibrium, inducing mineral dissolution, weathering, and precipitation reactions that can influence the porosity and permeability of host rocks. These changes either enhance or retard fluid flow, impacting the success of activities such as hydrofracturing, the disposal of petroleum-produced waters, and geothermal energy production. To improve our understanding of these reactions over a broad range of salinity, pH, and chemical composition, we performed 56-day batch reaction experiments with rocks from the Tuscaloosa Marine Shale (TMS). Experiments were completed at 90°C, starting pH values of 2, 4, or 6, and salinities of <0.1%, 3.2%, and 12% TDS with NaCl or Na-Ca-Mg-K-Cl fluid compositions. The results show that the fluid chemistry and changes in the physical nature of the TMS rock were driven by a set of chemical processes, including sulfide oxidation, silicate weathering, carbonate dissolution, and the precipitation of clays, iron oxides/hydroxides, and sulfate minerals. The timing and extents of these reactions varied with changes in pH, salinity, and fluid chemistry; However, most solutions converged to similar chemistries after a month of reaction time. The injection of dilute fluids and/or fluids with low pH

tended to increase porosity initially but were followed by precipitation reactions, including barite and clay minerals, which could lead to a loss of porosity and permeability or induce scaling. The initial changes to porosity were driven by carbonate dissolution of the isolated shell fragments within the TMS. The injection of high salinity fluids at circumneutral pH values and chemical compositions closer to those of existing formation waters limited physical changes to the TMS rock. Sulfide oxidation followed by the precipitation of iron oxides or oxyhydroxides was a rapid and consistent phenomenon among the experiments.

1. INTRODUCTION

When water is injected into the deep subsurface, mineral precipitation and dissolution reactions influence the porosity and permeability of the host strata. Changes in porosity and permeability can enhance or retard fluid flow, which can have a direct impact on activities such as hydrofracking for petroleum production, the disposal of contaminated waters (often co-produced with hydrocarbons), and the efficiency of enhanced geothermal energy operations (e.g., Ali and Hascakir, 2017; Li et.al., 2017; Huang et. al., 2020; Bratcher et. al., 2021). The hydrofracturing process typically involves pumping large volumes of dilute water (often groundwater or stream water) amended with chemical treatments into a low permeability hydrocarbon source rocks at pressures exceeding the rock strength to induce fracturing and enhance fluid flow. Studies that have investigated the chemistry of fracking fluids have reported rapid changes in fracking water chemistry recorded in water returned to the surface. Within the

first few weeks of fracturing the returned fluids exhibit increases in total dissolved solids (TDS; e.g., Engle and Rowan, 2014; Balashov et al., 2015; Vengosh et al., 2017). Elements such as chloride (Cl), sodium (Na), calcium (Ca), magnesium (Mg), potassium (K), and strontium (Sr) tend to increase rapidly, while concentrations of sulfate (SO4) in the initial fracking often decrease rapidly. The loss of sulfate may be tied to the precipitation of barite or gypsum (Engle and Rowan, 2014) or the microbial reduction of sulfur perhaps leading to the precipitation of sulfide minerals (e.g., Rosnes et al., 1991; Bakke et al., 1992; McGovern-Traa et al., 1997; Machel 1998). Increases in the TDS of fracking fluids appear to be the result of a combination of mixing with formation waters and mineral dissolution reactions (Harrison et al., 2017; Lu et al., 2017a; Lu et al., 2017b; Osselin et al., 2019; Hoffmann and Borrok, 2020). For example, a study by Lu et al., (2017a) identified the dissolution of calcite, dolomite, and feldspar, and the oxidation of sulfide minerals as critical features in controlling the fluid chemistry of simulated fracking waters with NaCl compositions. Prior to their injection, fracking fluids are often modified with various amendments, including acids, which can greatly accelerate these mineral dissolution reactions.

Water rock interactions are also important for deep subsurface water disposal and enhanced geothermal systems (EGS). For example, in Lu et.al.'s 2017(a) study, they found that injection of petroleum-produced brines from the Eagle Ford into the Hosston Formation induced the dissolution of anhydrite, dolomite, feldspars, and pyrite in this sandstone unit. Despite some dissolution, there was a small but measurable decrease in porosity and permeability in the system due to the precipitation of oxides, clays, and barite. Investigations by Pandey et. al. (2014 and 2015) examined water-rock interactions

in limestone and silicate EGS reservoirs. The authors determined that dissolution and precipitation reactions were dependent on carbonate and silica saturation levels of the injected water and were further complicated by changing temperatures as fluids flowed through these systems. Limestone EGS was particularly sensitive to changes in system pressures and temperatures, as these fluctuations controlled the dissolution (at lower pressure and temperature) and precipitation (at higher pressure and temperature) of carbonate minerals.

Although substantial experimental and modeling work exists for understanding water-rock interactions in simulated deep subsurface conditions, relatively few investigations have explored these reactions over the broad ranges of pH, salinity, and brine compositions that may be encountered in different subsurface injection scenarios. Furthermore, most previous work on this topic has focused primarily on the evolution of fluid chemistry. The changes in fluid chemistry are then linked to hypothesized mineral dissolution and precipitation reactions, but direct evidence of the mineralogical changes are not typically available. To address these concerns, we performed batch reaction experiments with the Tuscaloosa Marine Shale (TMS) and fluids of widely varying salinities using mixtures of dilute water, NaCl, and simulated produced water end members. Experiments were conducted at elevated temperature (90°C) and the starting pH of the experimental solutions was varied. Both fluid chemistries and physical changes in the rocks were evaluated with the primary goal of understanding how the different salinity, chemistry, and pH conditions impacted water-rock interactions.

2. METHODS

2.1. ROCK SOURCE AND PREPARATION

The rocks used in our experiments were collected from the TMS, an unconventional hydrocarbon reservoir with productive regions found in Mississippi and Louisiana, USA (Valentine et al., 2016; Enomoto et al., 2017; Borrok et al., 2019). TMS samples were collected from drill core collected from a depth of 13,000 ft below the ground surface. The TMS contains on average 48 wt.% total clays and phyllosilicate minerals, 23% quartz, 17% calcite, 4% plagioclase, 3% pyrite, and about 5% other trace minerals (Borrok et al., 2019).

Samples chipped from the inner part of the core (to avoid possible contamination) were crushed using an agate pestle and mortar and sieved to achieve a uniform size fraction. Material between 150 and 500 μm was used in our experiments. The specific mineral composition of the homogenized TMS samples used in our experiments was evaluated using a PANalytical X'Pert Multipurpose X-ray Diffractometer (XRD) in the Materials Research Center at Missouri S&T. Larger chips of the TMS, collected prior to crushing, were mounted in epoxy resin, and polished such that the physical nature of the rock could be observed. The chips were evaluated before and after experimentation using a FEI Helios Nanolab 600 Scanning Electron Microscope with an attached Oxford X-Max 50 EDS detector in the Advanced Materials Characterization Laboratory at Missouri S&T.

2.2. EXPERIMENTS

A series of batch reaction experiments were conducted to evaluate TMS-fluid interactions at 90°C under different conditions of fluid chemistry, starting pH, and salinity. Three fluid chemistries were evaluated, (1) dilute water (DW), (2) Na-Cl composition (NaCl), and (3) Na-Ca-Mg-K-Cl composition (Mixed). The DW chemistry was chosen to simulate the dilute compositions of most fracking fluids (minus additives). The salt compositions were chosen to evaluate conditions when fracking water mixes with saline formation waters and situations where petroleum produced waters are injected into the subsurface either for disposal or reused for fracking purposes. The experimental salt solutions were created by adding the appropriate amounts of NaCl, CaCl2, MgCl2 and KCl salts to pure water solutions. The pHs of the starting experimental solutions were adjusted to values of 2, 4, or 6, using small amounts of concentrated HCl. These values were chosen because fracking fluids are frequently acidified to a pH of ~2 prior to injection, while produced waters from the TMS have a pH of around 6 (Hoffmann and Borrok, 2020). Experiments with a starting pH of 4 provide an intermediary value for comparison. The salinities of the salt-rich experimental compositions were set at 3.2% and 12% TDS. The 90°C temperature for experiments was similar to that of the subsurface TMS conditions where fracking occurs. We did not utilize elevated pressures for our experiments. Previous experimental work simulating fracking conditions has suggested that the impact of pressure is secondary to changes driven by the temperature and fluid compositions (Morel and Hering, 1993; Harrison et.al., 2017).

Kinetic experiments were conducted by adding 10 mL of the chosen electrolyte (at the given pH, composition, and salinity) to a series of Savillex reaction vessels with

1 g of crushed TMS rock that was preheated to experimental conditions. Reaction vessels were then sealed and placed in a drying oven at 90°C and sampled as a function of time at 5, 15, 30, 90, and 120 minutes and 1, 3, 7, 14, 28, and 56 days. In all, 165 individual experiments were performed.

To evaluate physical changes, mounted and polished chips of the TMS were reacted with fluids that matched the compositions of the batch experiments that used crushed TMS rock. The chips were analyzed before experimentation to establish baseline physical conditions. The gold sputtering coating that was applied to the chips for SEM imaging was removed with a light polish before being subjected to experimentation. The mounted chips were then allowed to react under the same conditions as in the batch experiments for a period of 56 days. At this point they were removed and analyzed again on the SEM for comparison to the baseline conditions.

2.3. ANALYSIS

After each experiment, the fluid was immediately separated from the crushed rock using a 0.45 μm nylon syringe filter, and the pH of each sample was collected using a pre-calibrated pH meter. A fraction of this fluid was used to measure alkalinity using a LaMotte™ test kit method and the other fraction was acidified with 0.2 mL of concentrated HNO3 and refrigerated for later analysis using ICP-MS and/or ICP-OES instruments. Analysis for the DW samples was completed using a Nex Ion 300 ICP-MS at Missouri S&T. External standards were used to assess analytical precision, with errors determined to be less than 10%. A Perkin Elmer 2000D ICP-OES at Missouri was used to analyze the concentrations of S, Si and Sr for all the experimental solutions. Calibration

for ICP-OES analyses was done with matrix-matched standards. Replicate analysis of standards run as unknowns showed that the reproducibility was ± 5%.

The rest of the samples (NaCl and mixed) were analyzed using a Horiba Ultima Expert ICP-OES with a Peak Scientific NG5000A nitrogen generator and a Thermo Fisher Scientific iCAP RQ-ICP MS in the Center for Earth and Environmental Isotope Research at UT El Paso. Water standards USGS M-178 and USGS 182 were analyzed at least 3 to 5 times during each analytical session to assess analytical precision with the ICP-OES. USGS water standard (M-217) and NIST water standard (NIST 1640a) were used to assess the accuracy of the ICP-MS analysis. Analytical errors were determined to be less than 10% for both instruments. At UT El Paso the 3.2% TDS experiments were diluted to a 1:75 ratio and the 12% TDS solutions were diluted to a 1:300 ratio. Where possible, both major elements and trace elements were measured. However, the large dilutions needed to run some of the analyses raised detection levels to the point where some trace elements were not measurable (Table S1).

Pre-experiment SE and BSE analysis of mounted shale chips was done under vacuum conditions, with an accelerating voltage of 25 kV at a working distance of 5.1-5.7 mm to record initial surface morphology and elemental spatial relationships. Post-experiment SE and BSE analyses were also done under vacuum conditions, but with an accelerating voltage of 2.00 kV at a working distance of 3.8-4.1 mm.

3. RESULTS AND DISCUSSION

3.1. TMS MINERALOGY

Results from the XRD analysis show the homogenized TMS rock used in these experiments was comprised of approximately 47% phyllosilicate and clay minerals, 35% quartz, 10% kaolinite, 5% pyrite, and 3% calcite. Observation of mounted and polished TMS samples with an optical microscope and SEM shows that calcite is primarily present within foraminifera shell fragments that occur within the rock matrix or in clumped patches within relict burrows. Pyrite framboids are frequently observed with the calcite, filling shell chambers or relict burrows. Some pyrite framboids are also disseminated throughout the fine-grained matrix.

3.2. REACTION PATHWAYS

Figure 1 illustrates the changes in pH as a function of time for all the experimental runs. Regardless of the salinity, chemical composition, or starting pH (2, 4, or 6), the chemistry of all the experimental systems ultimately evolves to a pH range between 6 and 8 by the end of the experiments. However, despite the sameness of the pH in the long-term, there are several important shorter-term geochemical changes that differentiate the experimental systems. For example, the experiments with low salinities and all NaCl composition solutions with initial pH values of 4 and 6 exhibit a rapid increase in pH to values above 8.0 before decreasing to circumneutral values later in the

experiment. In fact, experiments with the dilute water composition reached a peak pH value of 9.5. The NaCl systems peak at pH values between 8 and 9. Conversely, the experiments with mixed chemical compositions that began at pH values of 4 and 6 equilibrate at circumneutral values within five minutes of reaction time. The pH values for these experiments never increase above 7. Most of the experiments that began at pH 2 equilibrated to circumneutral ranges within a few hours of reaction time, but the DW experiment took a bit over 10 hrs to equilibrate. The differences in the pathways of pH changes highlight different chemical pathways that exist primarily between the systems that are dilute or have simple NaCl compositions relative to systems with more complex Na-Ca-Mg-K-Cl compositions. The latter composition is more indicative of basinal brines or formation fluids, which may explain why an apparent equilibrium in the mineral-fluid reactions occurs so rapidly in these systems.

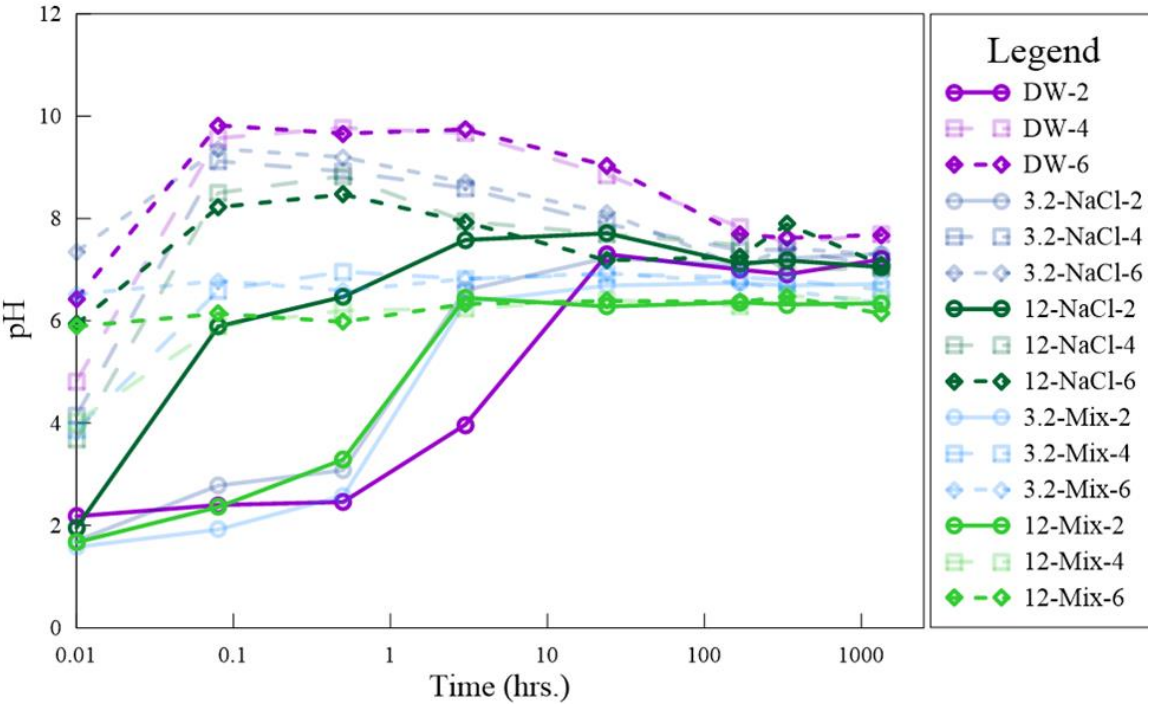

Figure 1. Changes in pH over time for all DW, NaCl, and mixed experimental solutions.

In addition to pH, we evaluated changes in the concentrations of major elements, alkalinity, and calculated saturation indices for key mineral phases to elucidate the important water-rock reaction pathways. Using these observations, we are able to define four key water-rock reaction processes that were common among the experiments: (1) Carbonate dissolution, (2) Silicate dissolution/precipitation, (3) Sulfide oxidation and dissolution, and (4) Precipitation of sulfate minerals. The timing and extents of these reactions varied measurably as a function of the starting pH, chemistry, and salinity of the experimental fluids. Below we summarize the experimental results and highlight the key reaction processes. In an effort to consolidate the enormous volume of data collected from these experiments, we have focused our discussion on differences among the experiments conducted as starting pHs of 2 and 6 and between solutions that are dilute and solutions that have the highest salinities (12% TDS). The data collected from experiments with a staring pH of 4 are generally similar to those of a starting pH of 6 and data for the 3.2% TDS experiments tended to be similar to the 12% TDS experiments. Data for all experiments (Table S2), including additional figures (Figures S1, S2, S3, etc.), can be found in the supplemental online information.

3.3. LOW PH EXPERIMENTS

Results from the experiments with DW, 12% NaCl and 12% mixed solutions at pH 2 are presented in Figures 2, 3, and 4. These figures demonstrate, in separate panels, how the pH, alkalinity, and key major elements (K, Si, Al, Na, Ca, S, Mg) and trace elements (Sr and Ba) changed over the course of the experiments. The final two panels in each figure track the calculated saturation indices for some of the most relevant

aluminosilicate, carbonate, and sulfate phases that may be dissolving or precipitating during the experiments. Note that the concentrations of the elements that comprise the high salinity electrolytes are not shown in the graphs because these were set by the initial electrolyte concentration and small variations from these large values were not measurable. The large dilutions needed to analyze the high salinity solutions caused the concentrations of some elements to be below detection limits (e.g., Si and Al; Table S1). In these cases, we used concentrations of one-quarter of the detection limit to calculate approximate saturation indices for the relevant minerals.

Concentrations of most of the major elements increased as a function of time as the low pH experiments progressed. For example, the concentrations of Na, Ca, Mg, K, and S all increased in the experiments in which these elements were measured. However, in the dilute water experiment the concentrations of Na, Ca, and Mg all dipped slightly near the end of the reaction time, suggesting that these elements were involved in precipitation reactions (Figure 2 b and c). Conversely, Ca and Mg increased throughout the entire duration of the 12% NaCl experiments (Figure 3c). Sulfate concentrations increased steadily in all the experiments (Figures 2c, 3c, and 4c), which is presumably the result of the oxidation of pyrite. Concentrations of Si tended to increase in the experiments overall, but were variable over time, which may reflect changes in the balance between dissolution and precipitation of silicate phases that occurred during the experiments. Aluminum is largely insoluble under these conditions, so concentrations for Al were low or below detection levels in most cases.

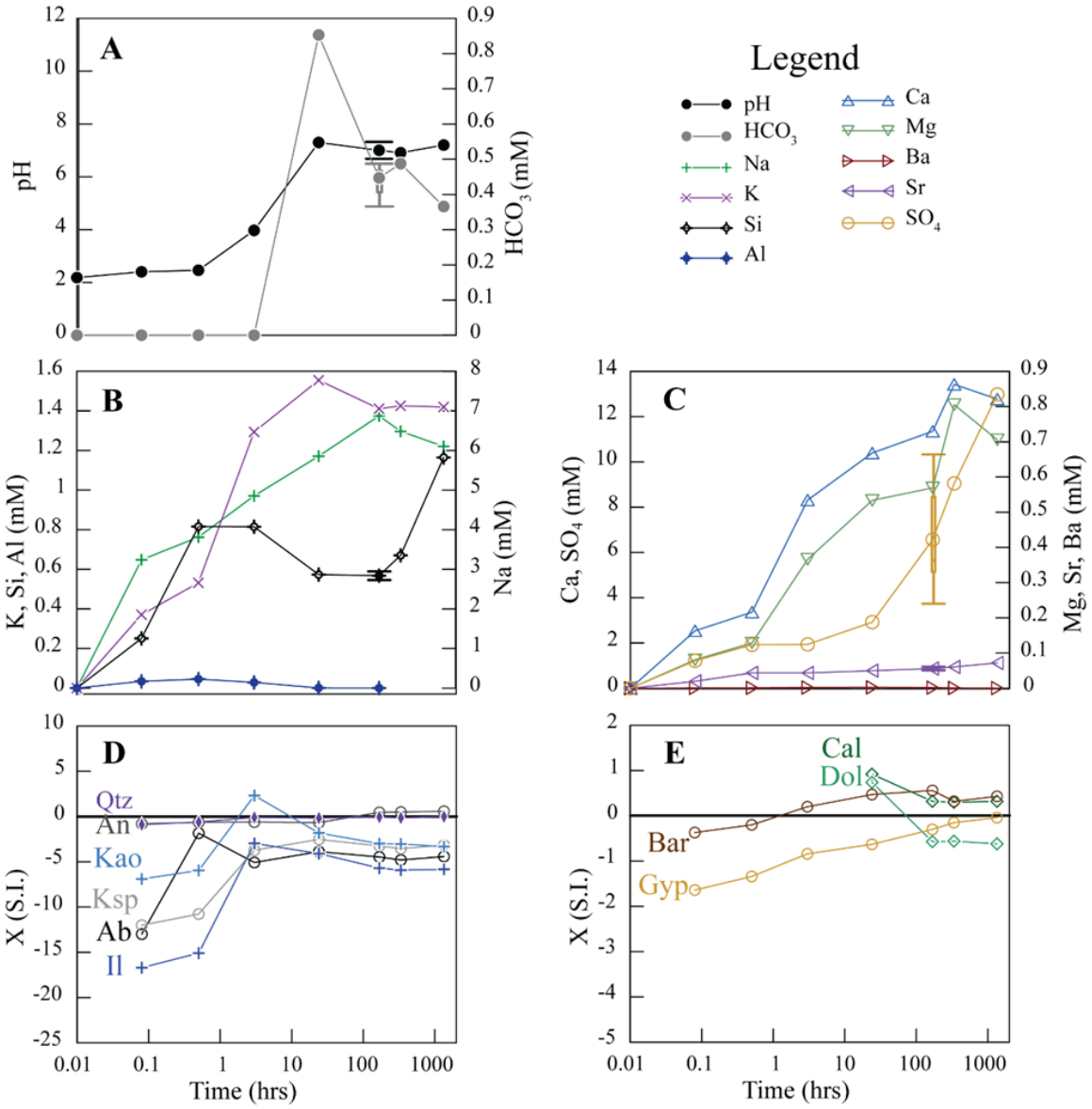

Figure 2. Changes in bulk chemistry and saturation indices for DW experimental solutions beginning at pH 2. Chemical data include HCO_3 and pH (A), concentrations of Si, Al, and K (B), concentrations of Ca, Mg, Sr, Ba, and SO_4 (C). Calculated saturation indices for quartz (Qtz), anorthite (An), kaolinite (Kao), potassium feldspar (Ksp), albite (Ab), and illite (Il) are shown in panel D, and those for calcite (Cal), dolomite (Dol), barite (Bar), and gypsum (Gyp) are shown in panel E. Error bars (1σ) for selected measurements are based on full experimental runs in completed in triplicate.

In all the solutions with initial pH values of 2, there was no carbonate alkalinity until the pH rose above about 4.0, which occurred after the first three hours of the

reaction for the NaCl and mixed electrolyte systems (Figures 3a and 4a) and after 24 hours of reaction time in the dilute water experiment (Figure 2a). The lack of carbonate alkalinity infers undersaturation of all these systems with respect to carbonate minerals early in the experiments. Once carbonate alkalinity was measurable, the saturation indices for both calcite and dolomite were initially oversaturated in the DW experiment (Figure 2e). The solution remained oversaturated with respect to calcite throughout the experiment, while the solution became undersaturated with respect to dolomite over time. In the 12% NaCl experiment, the first measured saturation index for calcite was close to equilibrium and that for dolomite was undersaturated (Figure 3e). The saturation indices for these carbonate minerals remained relatively unchanged over the duration of the experiment (Figure 3e). In the 12% mixed experiment, the first measured saturation index showed the system was undersaturated with respect to both calcite and dolomite (Figure 4e). These saturation indices increased later in the experiment, such that the solution became saturated with respect to calcite (Figure 4e).

In the experiments with dilute water, the saturation indices for common aluminosilicate minerals were below saturation initially and moved closer to saturation as the experiment progressed. The solution became saturated with respect to kaolinite briefly after 2 hours but dipped below saturation by 24 hours. This shift from oversaturation to undersaturation with respect to kaolinite corresponds with a drop in the concentrations of dissolved Si and Al, which may indicate that kaolinite or a similar phase precipitated. By the end of the experiment, the solution was saturated with respect to quartz and anorthite, but undersaturated relative to the other phases. Solutions from the experiments with 12% NaCl at pH 2 were initially saturated or oversaturated with respect

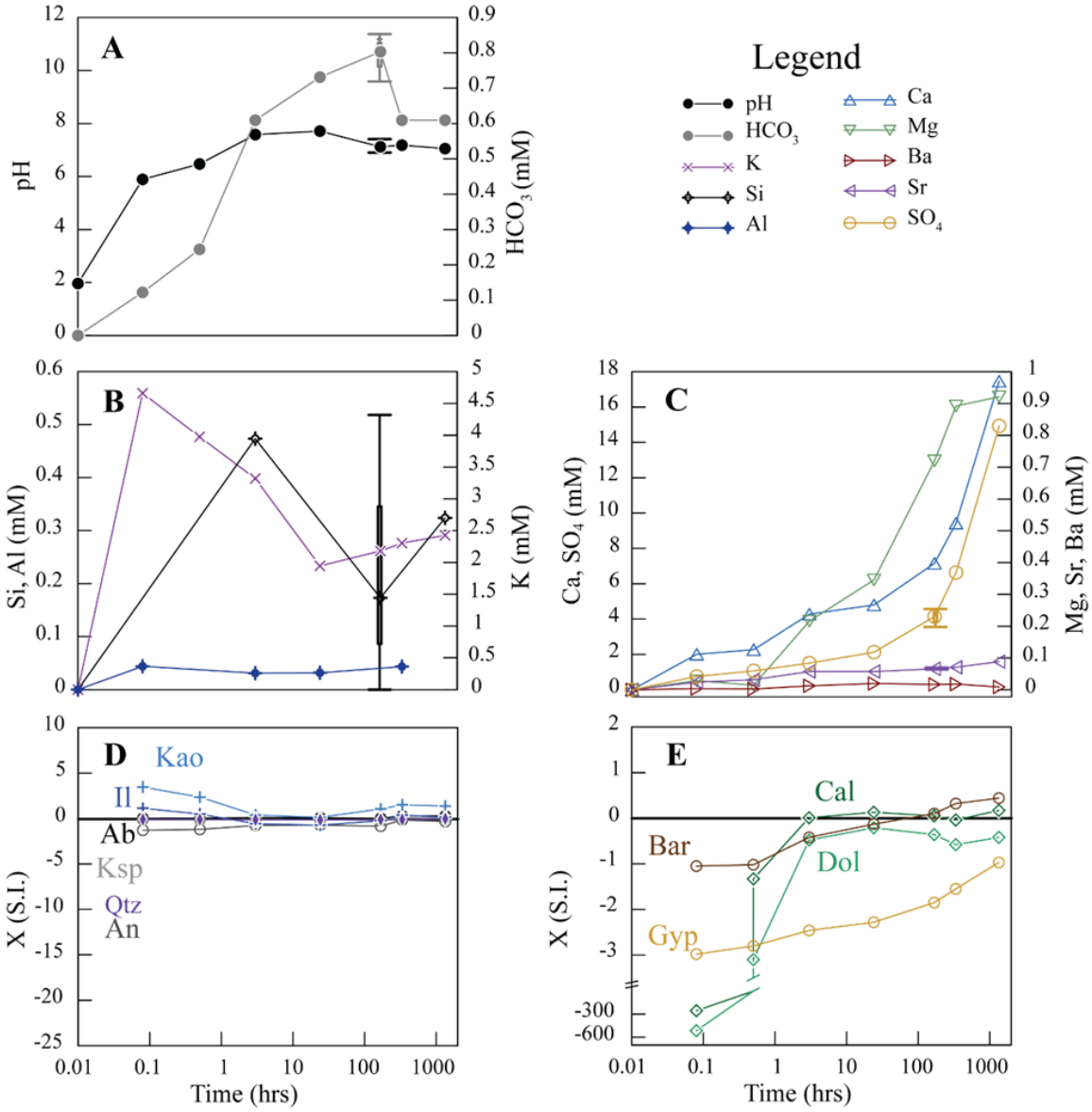

Figure 3. Changes in bulk chemistry and saturation indices for 12% TDS NaCl experimental solutions beginning at pH 2. Chemical data include HCO_3 and pH (A), concentrations of Si, Al, and K (B), concentrations of Ca, Mg, Sr, Ba, and SO_4 (C). Calculated saturation indices for quartz (Qtz), anorthite (An), kaolinite (Kao), potassium feldspar (Ksp), albite (Ab), and illite (Il) are shown in panel D, and those for calcite (Cal), dolomite (Dol), barite (Bar), and gypsum (Gyp) are shown in panel E. Error bars (1σ) for selected measurements are based on full experimental runs in completed in triplicate.

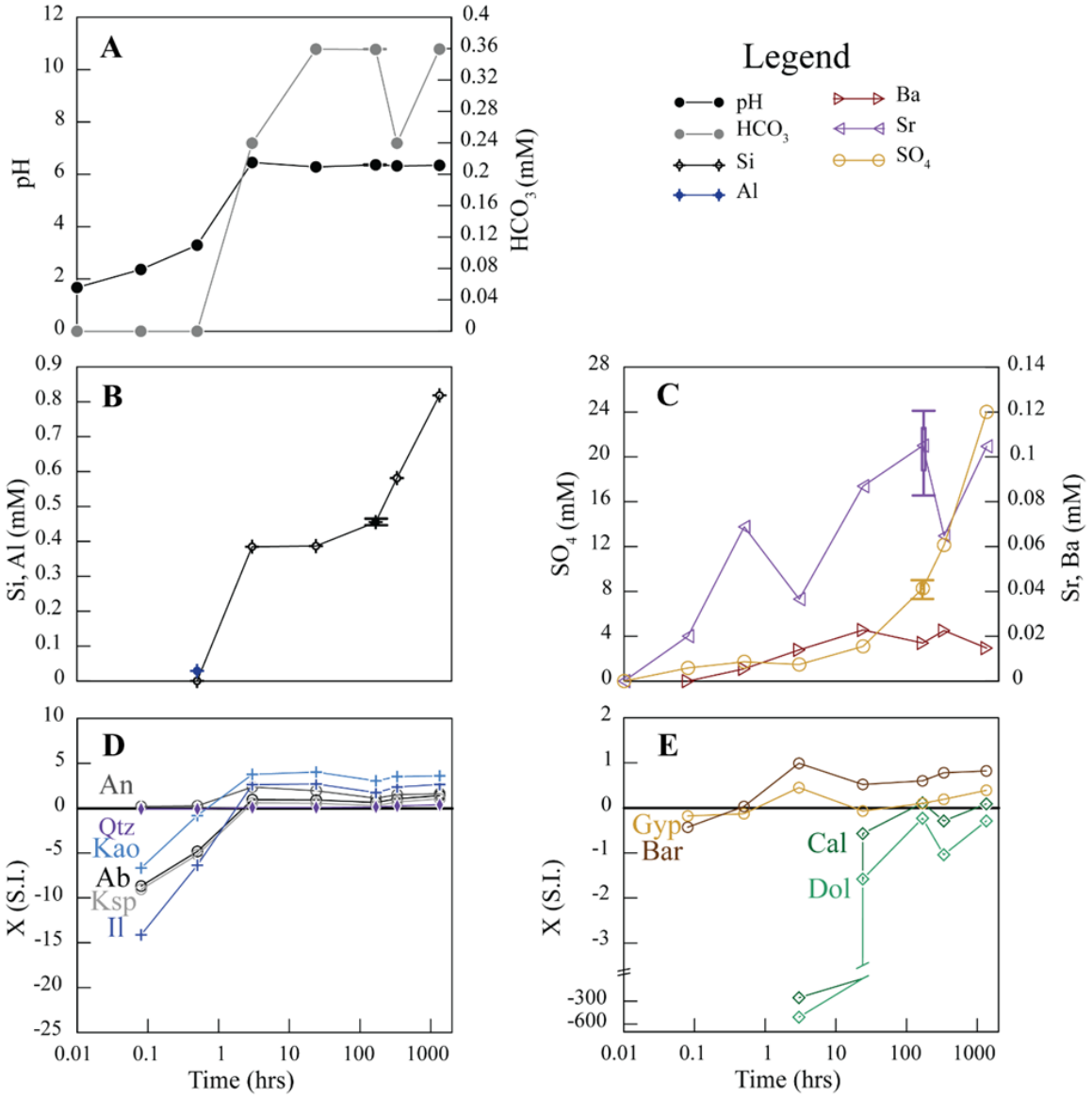

Figure 4. Changes in bulk chemistry and saturation indices for 12% TDS mixed composition experimental solutions beginning at pH 2. Chemical data include HCO_3 and pH (A), concentrations of Si, Al, and K (B), concentrations of Ca, Mg, Sr, Ba, and SO_4 (C). Calculated saturation indices for quartz (Qtz), anorthite (An), kaolinite (Kao), potassium feldspar (Ksp), albite (Ab), and illite (Il) are shown in panel D, and those for calcite (Cal), dolomite (Dol), barite (Bar), and gypsum (Gyp) are shown in panel E. Error bars (1σ) for selected measurements are based on full experimental runs in completed in triplicate.

to most of the aluminosilicate phases we evaluated (Figure 3b). The saturation indices for most of these silicate mineral phases dipped slightly during the experiments, ending near

the point of saturation. However, the solution remained oversaturated with respect to kaolinite. These trends likely reflect some early precipitation of aluminosilicate phases during experiments. Solutions from the experiments with 12% mixed electrolytes at pH 2 were initially undersaturated with respect to all phases but anorthite and quartz. However, within 2 hours the solution became oversaturated with respect to all the tested minerals.

The release of sulfate in these experiments is attributable to the oxidation of reduced sulfur in pyrite. This process is also reflected in the release of dissolved iron, which when oxidized, rapidly forms iron oxide/oxyhydroxide precipitates (Nordstrom and Southam, 1997). Figure 5a illustrates the release of Fe in these experiments. The concentrations of Fe peak early in the experiments before dropping to background levels. The concentrations of dissolved Fe in solution are limited because the reaction rate for the transformation of Fe(II) to Fe(III) increases rapidly with increasing pH and Fe(III) is highly insoluble in circumneutral pH conditions (e.g., Nordstrom and Southam, 1997; Bigham and Nordstrom, 2000; Rimstidt and Vaughan, 2003; Fernandes and Borrok, 2009). Based on the timing of the appearance of low concentrations of several trace elements such as Cu and Co (Table S1), it is also likely that these were associated with sulfide phases (probably pyrite) in the TMS samples. The release of sulfate from sulfide oxidation during the experiments can also lead to sulfate mineral precipitation reactions. Solutions from the dilute water and 12% NaCl experiments at pH 2 are initially undersaturated with respect to barite but become oversaturated with barite during the experiments by 2 hrs and 100 hrs, respectively (Figures 2e and 3e). The solutions remain undersaturated with respect to gypsum throughout the duration of the experiments, although the dilute water solution approaches equilibrium for gypsum by 1000 hours.

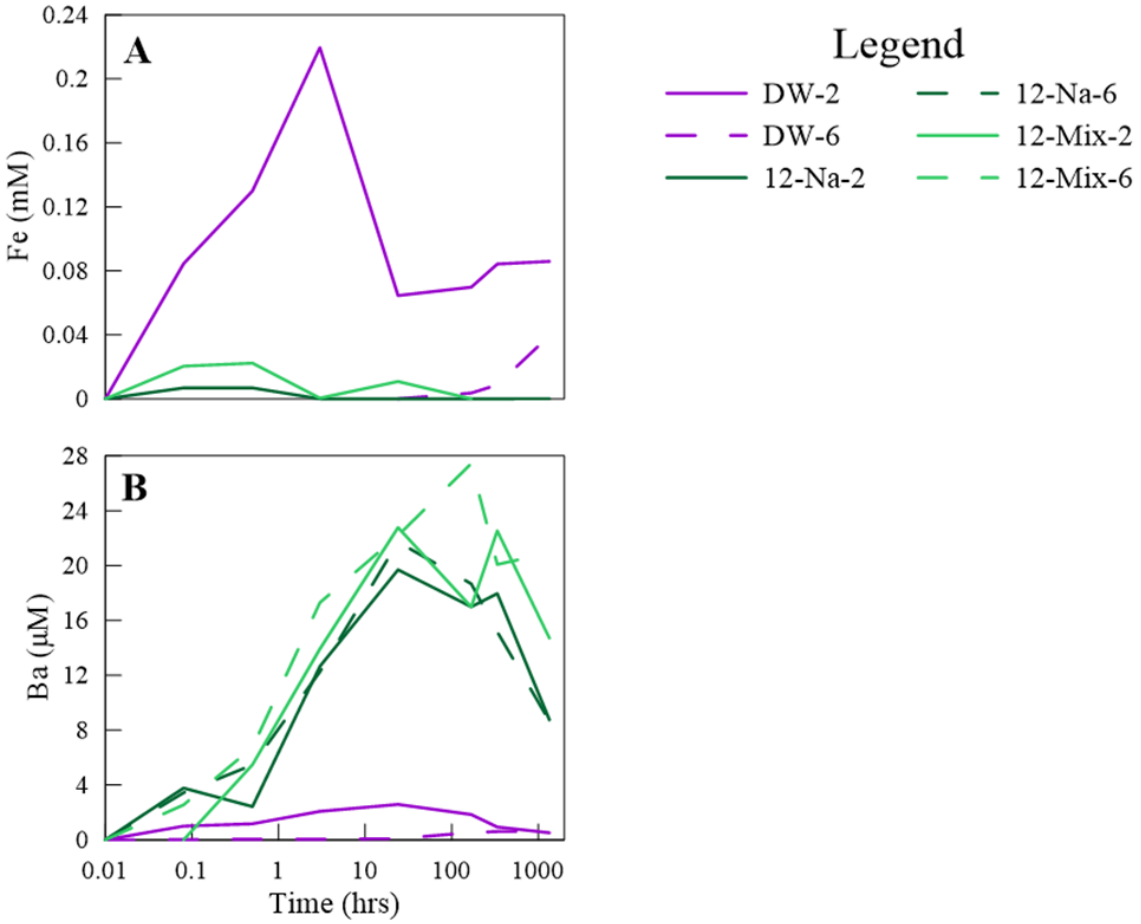

Figure 5. Concentrations of dissolved Fe (A) and Ba (B) for experiments with DIW, NaCl, and mixed experimental solutions initiated at pH 2 and pH 6.

Conversely, the solutions from the 12% mixed electrolyte experiment are initially undersaturated with respect to barite and gypsum but quickly become saturated with respect to these phases and remain so through the duration of the experiment (Figure 4e).

The fact that the concentrations of dissolved Ba in the 12% NaCl and mixed electrolyte experiments decrease near the end of these experiments (Figure 5b), suggests that small amounts of barite did precipitate in these systems. Concentrations of Ba in the dilute water experiment, however, were very low throughout. This suggests that the highly saline NaCl or mixed electrolyte solutions leached more Ba from the TMS rock.

We speculate that Ba may have been released from clay minerals via ion exchange reactions. The lack of Ba in the dilute water experiment limited the possible production of barite. This is likely why, instead of barite, we found gypsum crystals forming at the end of the experiments with dilute water.

3.4. CIRCUMNEUTRAL PH EXPERIMENTS

Results from the experiments with dilute water, 12% NaCl and 12% mixed solutions at pH 6.0 are presented in Figures 6, 7, and 8. These figures follow the same format as those illustrating the initial pH 2.0 experiments. Like in the pH 2.0 experiments, Si and Al data missing due to high dilution is assumed to be one-quarter of the instrument's detection limits for the purposes of calculating saturation indices (Table S1). Data for all measured elements are included in Table S2. Carbonate alkalinity in both the dilute water and 12% NaCl experiments followed similar increasing trends throughout the experiment but decreased after reaching a peak concentration at 10 hrs and 100hrs, respectively (Figures 6a and 7a). The initial increase in alkalinity in these experimental systems is also accompanied by an initial increase in pH. In fact, the pH of the dilute water experiment quickly increased to a value of 9.5 before decreasing back to circumneutral values by the end of the experiment (Figure 6a). The rapid increase in alkalinity and pH at the beginning of these experiments probably reflects carbonate dissolution, while the decreases in pH and alkalinity near the end of the experiments likely reflect mineral precipitation reactions. These patterns in pH and alkalinity are also reflected in the saturation indices for calcite and dolomite, which suggest that the solution

is undersaturated with respect to these phases initially but becomes oversaturated near the end of the experiment. On the other hand, the pH in the 12% mixed electrolyte

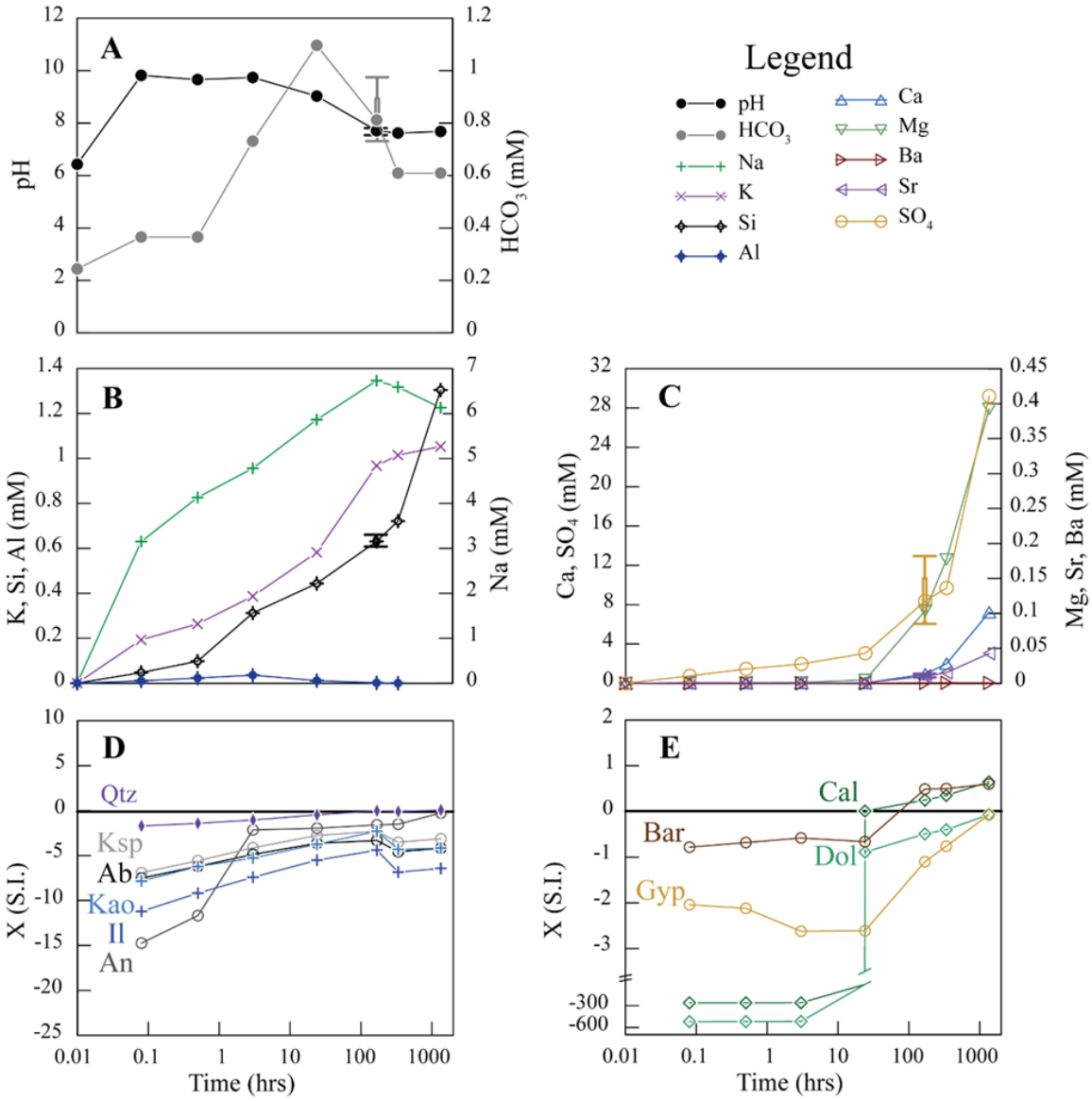

Figure 6. Changes in bulk chemistry and saturation indices for DW experimental solutions beginning at pH 6. Chemical data include HCO_3 and pH (A), concentrations of Si, Al, and K (B), concentrations of Ca, Mg, Sr, Ba, and SO_4 (C). Calculated saturation indices for quartz (Qtz), anorthite (An), kaolinite (Kao), potassium feldspar (Ksp), albite (Ab), and illite (Il) are shown in panel D, and those for calcite (Cal), dolomite (Dol), barite (Bar), and gypsum (Gyp) are shown in panel E. Error bars (1σ) for selected measurements are based on full experimental runs in completed in triplicate.

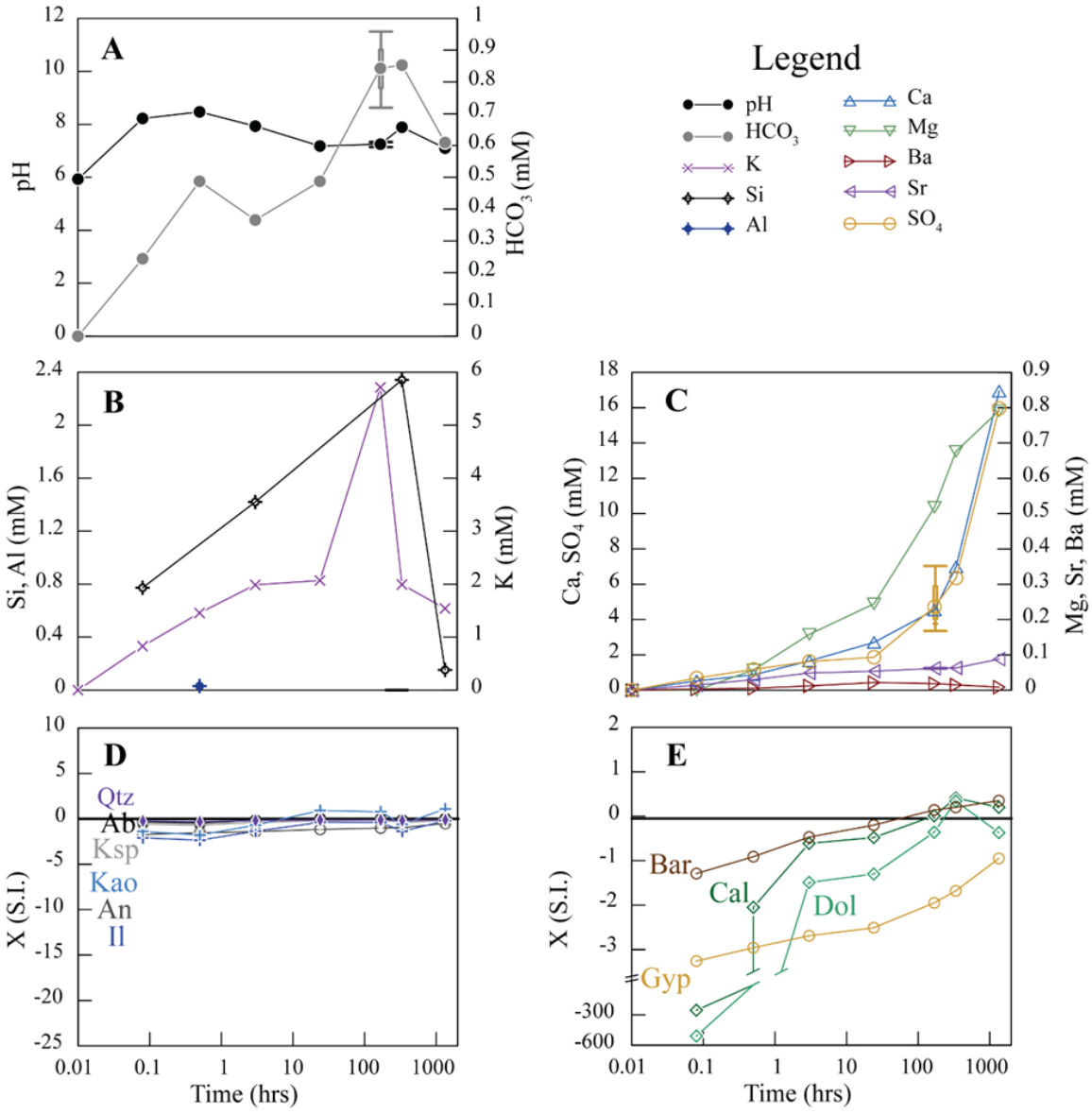

Figure 7. Changes in bulk chemistry and saturation indices for 12% TDS NaCl experimental solutions beginning at pH 6. Chemical data include HCO_3 and pH (A), concentrations of Si, Al, and K (B), concentrations of Ca, Mg, Sr, Ba, and SO_4 (C). Calculated saturation indices for quartz (Qtz), anorthite (An), kaolinite (Kao), potassium feldspar (Ksp), albite (Ab), and illite (Il) are shown in panel D, and those for calcite (Cal), dolomite (Dol), barite (Bar), and gypsum (Gyp) are shown in panel E. Error bars (1σ) for selected measurements are based on full experimental runs in completed in triplicate.

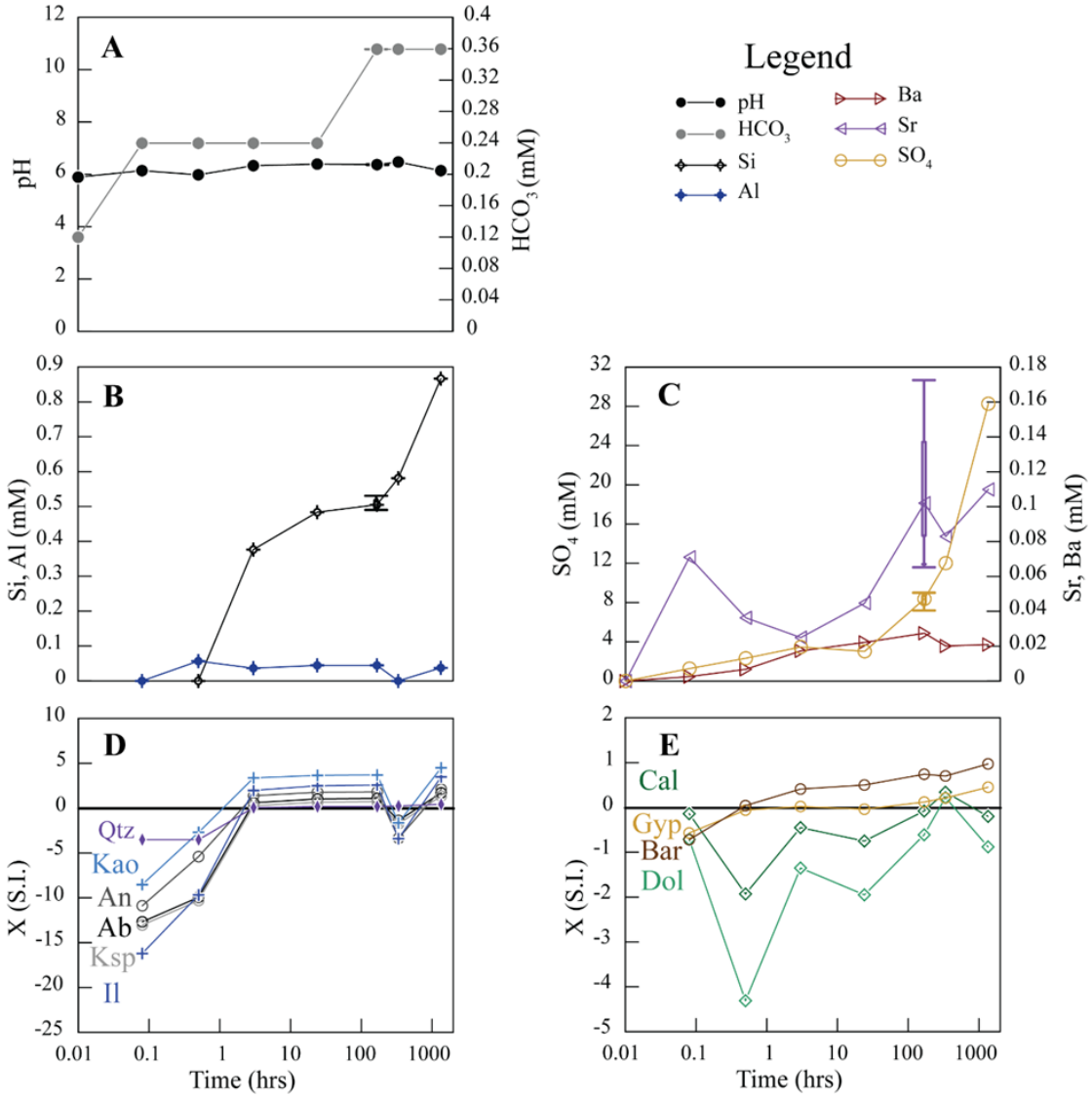

Figure 8. Changes in bulk chemistry and saturation indices for 12% TDS mixed composition experimental solutions beginning at pH 6. Chemical data include HCO_3 and pH (A), concentrations of Si, Al, and K (B), concentrations of Ca, Mg, Sr, Ba, and SO_4 (C). Calculated saturation indices for quartz (Qtz), anorthite (An), kaolinite (Kao), potassium feldspar (Ksp), albite (Ab), and illite (Il) are shown in panel D, and those for calcite (Cal), dolomite (Dol), barite (Bar), and gypsum (Gyp) are shown in panel E. Error bars (1σ) for selected measurements are based on full experimental runs in completed in triplicate.

experiment did not change significantly throughout the experiment (Figure 8a).

Moreover, the alkalinity of the solution increased to only about half the levels of the other

experiments and did not show a drop at the end of the experiment (Figures 5a and 8a). The saturation indices for calcite and dolomite in the 12% mixed electrolyte experiment did suggest the solution was undersaturated with respect to these phases for much of the experiment (Figure 8e), but the pH and alkalinity data suggest carbonate dissolution and precipitation reactions were limited relative to the other experimental systems.

As observed in the low pH experiments, most of the major elements increased as a function of time as the circumneutral pH experiments progressed. However, after an initial increase, the concentrations of Na and Al dropped slightly around 200 and 24 hours, respectively, in the dilute water experiment, suggesting that these elements may have been involved in precipitation reactions (Figure 6 b and d). Concentrations of Si generally increased over time in the dilute water and mixed electrolyte experiments (Figures 6b and 8b) but dropped substantially over the latter part of the NaCl experiment (Figure 7b). The trends in the saturation indices for the evaluated aluminosilicate phases were generally similar for the pH 2 and pH 6 experiments in that the solutions were undersaturated with respect to aluminosilicates initially but moved toward saturation and even oversaturation by the end of the experiments (Figures 6d and 8d). The dilute water system was substantially undersaturated with respect to aluminosilicates initially and became saturated with respect to quartz by the end (Figure 6d). Solutions in the 12% NaCl experiment were only weakly undersaturated with respect to a number of mineral phases initially and then became weakly oversaturated by the end of the experiment (Figure 7d an e). Solutions in the 12% mixed electrolyte experiment fluctuated from weakly undersaturated with respect to all the mineral phases at the start of the experiment to substantially oversaturated by the end (Figure 8d and e).

The trends in sulfate concentrations in all the pH 6 experiments were generally similar to their respective counterparts in the pH 2 experiments (Figures 6c, 7c, and 8c). The release of sulfate suggests that the oxidation of pyrite is a consistent phenomenon regardless of the tested salinity and pH when using experimental fluids that incorporate atmospheric levels of oxygen. Although the oxidation of pyrite is also reflected in the release of dissolved Fe(II) as illustrated in the pH 2 experiments (Figure 5a), the concentrations of Fe were all below detection in the pH 6 experiments. This is because at pHs much above 2 the oxidation from Fe(II) to Fe(III) is rapid and Fe(III) is highly insoluble under these conditions (e.g., Nordstrom and Southam, 1997; Bigham and Nordstrom, 2000; Rimstidt and Vaughan, 2003; Fernandes and Borrok, 2009).

Trends in the concentration of Ba among the pH 6 experiments also closely mirrored those in the pH 2 experiments (Figure 5b). A drop in the concentrations of Ba in the 12% NaCl and mixed electrolyte experiments at pH 6, suggests that small amounts of barite did precipitate in these systems. As in the pH 2 dilute water experiments, Ba concentrations were negligible in the dilute water experiments at pH 6. This reinforces the idea that high salinity fluids were required to leach Ba from the TMS rocks. We did not, however, observe gypsum precipitates in the dilute water pH 6 experiments.

3.5. PHYSICAL CHANGES IN THE TMS ROCK

Many of the mineral precipitation and dissolution reactions described above could also be seen visually in photomicrographs or SEM images of the polished TMS rock chips. These physical changes are important because they can influence the porosity and permeability of the rock and therefore fluid flow in the subsurface. The results of sulfide

oxidation/dissolution and carbonate dissolution can be seen in Figure 9. Here a photomicrograph of the polished TMS rock shows pyrite framboids clustered within a carbonate shell fragment prior to experimentation (Figure 9a). After experimentation, another photomicrograph shows that the pyrite has weathered and oxidised, and dark void spaces are present around the boundaries of the shell fragment (Figure 9b). An SEM image of the same region further illustrates that the individual pyrite grains have been weathered into a mass (presumably of oxidized iron minerals) and that porosity has been created around the shell margins (Figure 9c).

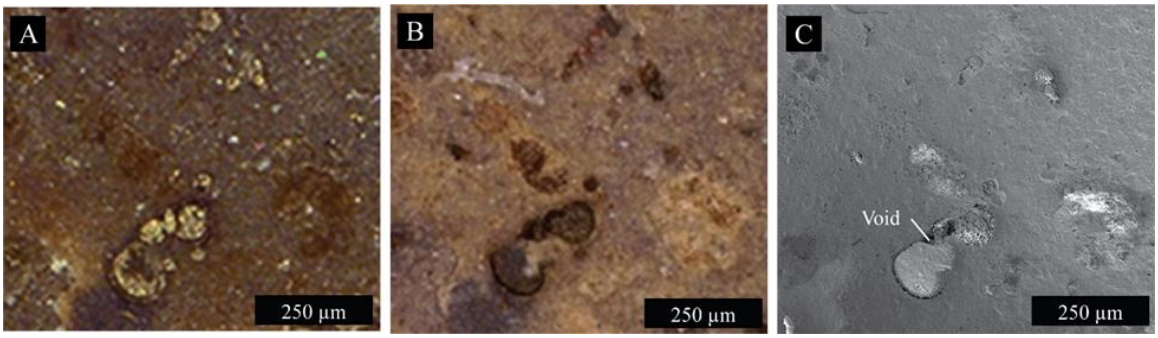

Figure 9. Physical changes in TMS rock chips exposed to the DW-2 experimental solution for 56 days. Images include reflected light photomicrographs taken before (A) and after exposure (B) and SEM images after exposure (C).

To further investigate the degree of carbonate weathering in the experiment with 12% mixed electrolyte at pH 6, we evaluated TMS chips before and after interaction with these fluids (Figure 10). The stable pH, and modest changes in alkalinity associated with these experiments (Figure 8a) suggested that carbonate dissolution was limited. Element mapping before and after experimentation shows that Ca was not substantially leached from the shell fragments in these experiments (Figure 10a and b). Moreover, the SEM image of the rock after experimentation does not show the generation of porosity around

the shell fragment (Figure 10c), as was observed in other experiments. This confirms the idea that carbonate dissolution was absent or limited in the pH 6 mixed experiments.

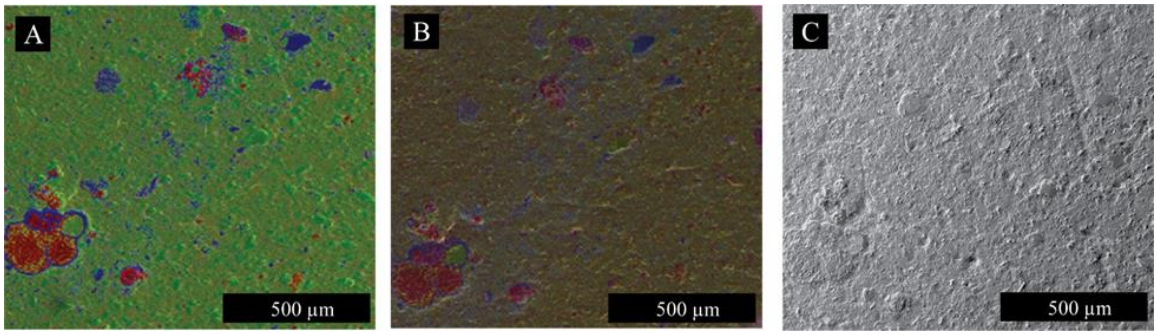

Figure 10. Physical changes in TMS rock chips exposed to the high salinity mixed-6 experimental solution. SEM images include false color EDS elemental maps of Ca, Fe, Al, Si, and K before (A) and after (B) 56 days of exposure and an image of change to the TMS morphology after exposure (C).

4. CONCLUSIONS

Our experimental results suggest that the TMS underwent a series of well-defined chemical reactions that varied in their extents and timing with different combinations of pH, salinity, and fluid chemistry. Despite these differences the fluids from all the experiments generally converged to a similar overall chemistry after several weeks of reaction time. As seen in similar experimental systems (Harrison et al., 2017; Li et.al., 2017; Lu et al., 2017a; Lu et al., 2017b; Osselin et al., 2019; Huang et. al., 2020; Bratcher et. al., 2021), the most important chemical processes included sulfide oxidation, silicate weathering, carbonate dissolution, and the precipitation of clays, iron oxides/hydroxides, and sulfate minerals. Sulfide oxidation, as measured by increasing concentrations of SO4, is a significant and consistent reaction among the experiments. This is because all the

experiments had in common small amounts of dissolved oxygen from the atmosphere that could drive these reactions. The rates of subsequent oxidation and precipitation of the Fe released from pyrite, however, occurred at different rates, depending upon the pH of the system (e.g., Nordstrom and Southam, 1997; Bigham and Nordstrom, 2000; Todd et al., 2003; Fernandez and Borrok, 2009). Silicate weathering was harder to track, but available data for dissolved Si and calculated saturation indices suggest that these reactions occurred quickly in most experiments and were likely followed by the precipitation of small amounts of secondary aluminosilicate phases. Carbonate dissolution was a significant but more inconsistent reaction with release rates of Ca and Mg changing with the initial pH of the solutions, the salinity, and chemical complexity. Generally, the lower pHs increase the rates of carbonate dissolution, while the higher salinities appeared to suppress carbonate dissolution. This was particularly so for high salinity solutions that contained Ca and Mg in addition to Na. In solutions with initial pH values higher than 4, the release of Ca is delayed and mirrors or overlaps with the timing of the release of SO4 ions. This correlation may suggest that carbonate dissolution in the higher pH solutions is linked to the small amounts of acidity created during sulfide oxidation. The dissolution of sulfides and carbonates created substantial porosity in the TMS shales. However, the spatially isolated nature of the carbonate shell fragments and pyrite framboids suggests that there may have been little increase in permeability.

In addition to Fe-oxides and -oxyhydroxides and secondary aluminosilicates, our data suggest that barite and sometimes gypsum minerals precipitated in our experiments. Although not observed directly, most experiments became oversaturated with respect to barite and the dissolved concentrations of Ba did begin to drop by the end of the

experiments. In the DW solutions, less Ba was leached from the TMS (presumably through clay minerals), which allowed for the precipitation of gypsum instead of barite. Gypsum crystals were observed in the DW pH 2 experiment (Figure S11).

These findings suggest that using fluids with pHs, salinities, and compositions that are similar to those of formation waters would be the best choice for subsurface applications where changes in the character of the host rock are not desired. Mineral dissolution and subsequent precipitation reactions are limited in this case because the fluids are already near equilibrium with the mineral compositions within the host rock. On the other hand, although low pH fluids may generate some new porosity, this is also followed in the longer term by the precipitation of secondary phases that may reduce porosity or induce scaling in wells. It is also less desirable to inject fluids that contain SO4 (or substantial amounts of dissolved oxygen which will generate SO4 via sulfide oxidation reactions). The presence of dissolved SO4 in our experiments always led to the precipitation of barite or gypsum, which would be undesirable if it leads to reducing porosity and permeability. Future investigations of these water-rock interactions should additionally examine the role of pressure in affecting mineral dissolution and precipitation under elevated temperature conditions.

REFERENCES

Ali, Maaz, and Berna Hascakir, 2017, Water/Rock Interaction for Eagleford, Marcellus, Green River, and Barnett Shale samples and Implications for Hydraulic-Fracturing-Fluid Engineering. SPE Journal, 177304.

Bakke, R., B.Rivedal, S. Mehan,, 1992, Oil reservoir biofouling control, Biofouling. v. 6,p. 53-60.

Balashov, Victor N., Terry Engelder, Xin Gu, Matthew S. Fantle, Susan L. Brantley, 2015, A model describing flowback chemistry changes with time after Marcellus Shale hydraulic fracturing. AAPG Bulletin, vol. 99, no. 1, pp. 143-154.

Bigham, J.M., D.K. Nordstrom, 2000, Iron and aluminum hydroxysulfides from acid sulfate waters. Rev. Mineral. Geochem. v. 40, p. 351-403.

Borrok, David M., Wan Yang, Mingzhen Wei, Mehdi Moktari, 2019, Heterogeneity of the mineralogy and organic content of the Tuscaloosa Marine Shale. Marine and Petroleum Geology. V. 109, p717-731.

Bratcher, Jordan C., John P. Kaszuba, Ryan J. Herz-Thyhsen, Janet C. Dewey, 2021, Ionic Strength and pH Effects on Water-Rock Interaction in an Unconventional Siliceous Reservoir: On the Use of Formation water in Hydraulic Fracturing. Energy Fuels, v. 35, p. 18414-18429.

Enomoto, C.B, Hackley, P.C., Valentine, B.J., Rouse, W.A., Dulong, F.T., Lohr, C.D., and Hatcherian, J.J., 2017. Geologic characterization of the hydrocarbon resource potential of the Upper Cretaceous Tuscaloosa Marine Shale in Mississippi and Louisiana, U.S.A., Gulf Coast Association of Geological Societies Transactions article #00193, 67, 95-109.

Engle, Mark and Elisabeth L. Rowan, 2014, Geochemical evolution of produced waters from hydraulic fracturing of the Marcellus Shale, northern Appalachian Basin: A multivariate compositional data analysis approach. International Journal of Coal Geology, vol. 126, pp. 45-56.

Fernandez, Alvaro, David M. Borrok, 2009. Fractionation of Cu, Fe, and Zn isotopes during the oxidative weathering of sulfide-rich rocks. Chemical Geology, v. 264, p. 1-12.

Harrison, Anna L., Adam D. Jew, Megan K. Dustin, Dana L. Thomas, Claresta M. Joe-Wong, John R. Bargar, Natalie Johnson, Gordon E. Brown Jr., Katherine Maher, 2017, Element release and reaction-induced porosity alteration during shale-hydraulic fracturing fluid interactions. Applied Geochemistry, vol. 82, pp 47-62.

Hoffmann, A.A., D.M. Borrok, 2020, The geochemistry of produced waters from the Tuscaloosa Marine Shale, USA. Applied Geochemistry, vol. 116, 104568.

Huang, Tianming, Zhenbin Li, Bernhard Mayer, Michael Nightengale, Xiao Li, Guanfang Li, Yin Long, Zhonghe Pang, 2020, Identification of Geochemical Processes During Hydraulic Fracturing of a Shale Gas Reservoir: A Controlled Field and Laboratory Water-Rock Interaction Experiment. Geophysical Research Letters, 47, e2020GL090420

Li, Yiman, Tianming Huang, Zhonghe Pang, Chai Jin, 2017, Geochemical processes during hydraulic fracturing: a water-rock interaction experiment and field test study. Geosciences Journal, v. 21, no. 5, p. 753-763.

Lu, Jeimin, Roxana Darvari, Jean-Philippe Nicot, Patrick Mickler, Sayyed A. Hosseini, 2017(a), Geochemical impact of injection of Eagle Ford brine on Hosston sandstone formation – Observations of autoclave water-rock interaction experiments. Applied Geochemistry, vol. 84, pp 26-40.

Lu, Jeimin, Patrick J. Mickler, Jean-Philippe Nicon, Wanjoo Choi, Willian L. Esch and Roxana Darvari, 2017(b), Geochemical interactions of shale and brine in autoclave experiments - Understanding mineral reactions during hydraulic fracturing of Marcellus and Eagle Ford Shales. AAPG Bulletin, v. 101, no. 10, pp. 1567-1597.

Machel, H.G., 1998, Bacterial and thermochemical sulfate reduction in diagenetic settings – old and new insights. Sedimentary Geology, v. 140, p. 143-175.

McGovern-Traa, Caroline, Jyh-Yih Leu, W. Allan Hamilton, Iain S.C. Spark, Ian T.M. Patey, 1997, The presence of sulfate-reducing bacteria in live drilling muds, core materials and reservoir formation brine from new oilfields. Petroleum Geology of the Irish Sea and Adjacent areas, Geological Society Special Publication No. 124, p.229-239.

Morel, F.M.M., J.G. Herring, 1993, Principles and Applications of Aquatic Chemistry. Wiley-Interscience, New York, p. 588.

Nordstrom, D.K., Southam G., 1997, Geomicrobiology of sulfate mineral oxidation. Rev. Mineral. Geochem, v. 35, p. 361-390.

Osselin, F., S. Saad, M. Nightengale, G. Hearn, A-M. Desaulty, E.C. Gaucher, C.R. Clarkson, W. Kloppmann, B. Mayer, 2019, Geochemical and sulfate isotopic evolution of flowback and produced waters reveals water-rock interactions following hydraulic fracturing of a tight hydrocarbon reservoir. Science of the Total Environment, vol. 687, pp. 1389-1400.

Pandey, S.N., A. Chaudhuri, S. Kelkar, V.R. Sandeep, H. Rajaram, 2014, Investigation of permeability alteration of fractured limestone reservoir due to geothermal heat extraction using three-dimensional thermo-hydro-chemical (THC) model. Geothermics, vol. 51, pp. 46-62.

Pandey, S.N., A. Chaudhuri, H. Rajaram, S. Kelkar, 2015, Fracture transmissivity evolution due to silica dissolution/precipitation during geothermal heat extraction. Geothermics, vol. 57, pp. 111-126.

Rimstidt, J. Donald, David J. Vaughan, 2003, Pyrite oxidation: a state-of-the-art assessment of the reaction mechanism. Geochemica et Cosmochimica Acta, v. 67, p. 873-880.

Rosnes, J.T., Arne Graue, Torlelv Lien, 1991, Activity of sulfate-reducing bacteria under simulated reservoir conditions. SPE Production Engineering, p. 217-220

Todd, E.C., D.M. Sherman, J.A. Purton, 2003, Surface oxidation of chalcopyrite (CuFeS2) under ambient and atmospheric and aqueous (pH 2-10) conditions: Cu, Fe L-and O K-edge X-ray absorption spectroscopy. Geochem. Cosmochem. Acta., v. 67, p. 2137-2146.

Valentine, B.J., Hackley, P.C., Enomoto, C.B., Lohr, C.D., and Scholl, O.D., 2016. Preliminary evaluation of source rock potential and burial history of the Upper Cretaceous Tuscaloosa Marine Shale in Mississippi and Louisiana, U.S.A. American Association of Petroleum Geologists Search and Discovery Article 90259, 1 p.

Vengosh, Avner, Andrew Kondash, Jennie Harkness, Nancy Lauer, Nathaniel Warner and Thomas H. Darrah, 2017. The geochemistry of hydraulic fracturing fluids. Procedia Earth and Planetary Science, v. 17, pp. 21-24.

SECTION

2. CONCLUSIONS AND RECOMMENDATIONS

2.1. CONCLUSIONS

The produced waters of the TMS are highly saline Na-Ca-(Mg-K)-Cl brines resulting from the dilution of Jurassic age evaporated seawater by less saline water sources, likely fracking water used in well completion. Moderate correlations between the concentration of TDS and PWV suggest the fluids approach the formation water endmember over the duration of production. Strong correlations of trace elements Zn, Tl, As, Mn, and Ni and moderate correlations of V, Co, Pb, and Cu concentrations to TDS indicate these elements were primarily sourced in the formation waters. Moderate correlations to PWV are also observed in major elements Na, Ca, Sr, and Cl, suggesting the same formation water source. Weak correlations of Mg, K, Fe, and Cd, or absent correlations of Se, B, Mo, and Cr, suggest a primary source other than the formation waters. A moderate correlation of Cu and V concentrations with POV suggests a link between these elements and the organic complexes in the hydrocarbon system. Lastly, lower concentrations of Zn and Pb in the PW of the TMS compared to adjacent formations suggest a difference in metal availability and redox conditions within the shale unit.

Water-shale interaction experiments reveal a series of well-defined chemical reactions, which vary in extent and timing due to variations in pH, salinity, and fluid chemistry combinations, but ultimately converge to similar overall chemistry. Primary

chemical processes include sulfide oxidation, silicate weathering, carbonate dissolution, and the precipitation of clays, iron oxides/hydroxides, and sulfate minerals. Sulfide oxidation is a significant and consistent reaction in all the experiments due to the presence of atmospheric oxygen in initial fluids to drive the reactions. Pyrite oxidation occurs at different rates, depending on the system's pH. Silicate weathering occurred quickly in most experiments and was likely followed by the precipitation of small amounts of secondary aluminosilicate phases. Carbonate dissolution was a significant but inconsistent reaction, with Ca and Mg release rates varying with initial pH, salinity, and chemical complexity. Lower pHs increased the dissolution rates, while higher salinities and the presence of Ca and Mg in the initial solution suppressed the rates. In experiments with initial pH over 4, the release of Ca and Mg is delayed and mirrors or overlaps the timing of release for SO_4 ions, suggesting carbonate dissolution in these experiments is tied to small amounts of acidity created during sulfide oxidation. The dissolution of carbonates creates increased porosity in the TMS shales, but the carbonate shell fragments' isolated nature suggests little permeability increase. Increases in porosity due to carbonate dissolution are potentially reversed by the precipitation of sulfides in barite and gypsum.

Results suggest that fracking fluids with pHs, salinities, and compositions similar to local formation waters would be the best choice where reaction-based physical changes of host rock are not desired. Such near-equilibrium conditions between fluids and solids limit mineral dissolution and subsequent precipitation reactions. Results also expand on the effects of sulfide oxidation in the subsurface due to a substantial amount of dissolved oxygen in fracking fluid.

2.2. RECOMMENDATIONS

Future investigations of such water-rock interactions should expand to evaluate how the role of pressure affects mineral dissolution and precipitation under elevated temperature conditions. Consideration should also be given to methods of SO_4 removal before reuse or during cycling. If investigations into brine (re)cycling in other formations are conducted, experiments should be expanded to reflect water-rock reactions in those formations. These should include fluid compositions and host rock types encountered, such as tight sandstones, limestones, and transitional compositions for petroleum systems or igneous variations for EGS.

APPENDIX A

SUPPLEMENTAL TABLE FOR PAPER I: THE GEOCHEMISTRY OF PRODUCED WATERS OF THE TUSCALOOSA MARINE SHALE, USA

Table A1. Production and chemistry data by Well Number.				
Well Number	Production Time	Fracking Water	Produced Oil	Produced Water
	Months	gal	bbl	bbl
1	56	Not Avail.	72,479	99,108
2	34	11,756,137	111,064	54,636
3	32	12,606,739	118,800	38,518
4	31	11,653,719	99,989	40,327
5	42	7,880,215	254,368	68,521
6	50	11,282,275	279,567	89,178
7	43	8,286,340	251,124	63,551
8	59	10,884,999	166,166	99,210
9	48	12,570,429	122,367	147,564
10	48	14,984,701	233,333	169,316
11	43	7,135,558	192,629	186,951
12	45	10,604,759	130,560	165,828
13	63	13,731,383	243,993	253,210
14	57	Not Avail.	49,582	23,823
15	51	12,162,701	77,321	66,885
16	34	11,511,201	98,506	74,510
17	36	Not Avail.	110,881	59,891
18	45	13,223,708	205,381	193,808
19	45	13,307,631	286,049	314,772
FB stg. 1.1				
FB stg. 1.1				
FB stg. 2.1				
FB stg 2.2				
R^2 for POV				
R^2 for PWV				

Table A1. Production and chemistry data by Well Number. (Cont.)						
Well Number	Produced Gas	Cl	Br	SO_4	HCO_3	Na
	Mcf	mg/L	mg/L	mg/L	mg/L	mg/L
1	24,485	133,200	1369.7	<DL	60	48,276
2	49,483	70,914	884.0	<DL	280	29,014
3	37,000	74,640	947.6	<DL	240	40,796
4	35,828	75,873	771.2	953.1	380	33,441
5	75,881	87,872	881.1	<DL	260	34,761
6	66,384	110,288	1244.3	<DL	100	48,318
7	66,484	104,956	988.4	<DL	200	41,348
8	58,034	82,760	828.1	<DL	180	38,049
9	38,115	91,936	971.6	<DL	180	41,542
10	106,650	103,357	1000.6	<DL	160	41,635
11	65,895	79,656	1002.6	<DL	120	44,362
12	54,738	114,643	956.7	683.0	60	45,076
13	222,528	133,825	1345.2	825.5	100	45,318
14	178,138	102,789	1152.6	<DL	180	36,753
15	49,135	105,297	938.6	687.6	180	34,612
16	54,741	105,244	853.9	634.0	220	33,384
17	72,400	119,057	861.0	<DL	100	41,368
18	185,176	107,557	1080.2	<DL	60	43,687
19	342,013	155,764	1247.6	587.4	40	47,123
FB stg. 1.1		34,090	1	150	525	20,710
FB stg. 1.1		41,210	19	150	280	23,330
FB stg. 2.1		55,510	120	105	595	29,170
FB stg 2.2		54,700	130	92	575	29,750
R^2 for POV		0.08	0.09	NA	0.09	0.20
R^2 for PWV		0.36	0.26	NA	0.43	0.37

Table A1. Production and chemistry data by Well Number. (Cont.)								
Well Number	Ca	Mg	K	Sr	Fe	Ba	TDS	Mn
	mg/L	mg/L	mg/L	mg/L	mg/L	mg/L	%	mg/L
1	16,878	1303.7	844.5	650.9	122.8	17.4	20.27	21.46
2	6,524	574.9	426.8	422.6	129.6	34.8	10.92	3.65
3	9,283	888.5	679.3	503.8	98.4	42.4	12.81	6.60
4	4,886	461.3	498.7	344.7	83.8	45.1	11.77	1.34
5	6,849	657.1	561.6	414.2	144.8	37.1	13.24	3.23
6	14,970	1214.7	803.2	549.7	112.6	45.4	17.76	13.24
7	10,670	961.5	727.8	548.5	134.9	75.0	16.06	9.91
8	8,180	768.9	447.4	547.7	157.2	71.3	13.20	3.12
9	11,144	1017.6	603.5	730.0	71.9	61.7	14.83	11.30
10	11,145	966.0	569.2	660.1	67.1	39.4	15.96	11.36
11	11,524	967.0	568.2	737.1	87.0	42.9	13.91	12.55
12	15,863	1251.9	760.1	715.6	193.8	89.9	18.03	
13	17,080	1413.0	870.5	856.0	274.6	109.2	20.20	
14	13,443	972.5	746.4	638.3	130.2	97.2	15.69	
15	8,825	909.8	651.7	88.9	133.4	64.8	15.24	
16	9,144	831.2	546.3	679.3	93.0	80.0	15.17	
17	13,876	1249.1	811.9	661.2	161.3	93.1	17.82	
18	15,701	1241.7	792.4	769.9	128.3	88.1	17.11	
19	18,431	1332.3	963.9	824.6	175.1	140.3	22.66	
FB stg. 1.1	105	11	58		30	0		
FB stg. 1.1	985	79	72		68	4		
FB stg. 2.1	2,820	225	150		200	52		
FB stg 2.2	3,200	235	170		205	51		
R^2 for POV	0.08	0.08	0.08	0.11	0.06	0.04	0.11	0.00
R^2 for PWV	0.42	0.38	0.22	0.47	0.17	0.27	0.42	0.25

Table A1. Production and chemistry data by Well Number. (Cont.)								
Well Number	B	Cu	Zn	P	Ni	Se	As	V
	mg/L	mg/L	mg/L	mg/L	mg/L	mg/L	mg/L	mg/L
1	14.76	7.95	6.67	1.44	0.39	0.95	0.49	0.33
2	15.19	3.84	0.04	4.66	0.16	0.66	0.24	0.18
3	14.39	6.21	0.11	4.66	0.23	0.81	0.33	0.24
4	14.21	7.40	0.25	14.28	0.17	0.57	0.30	0.23
5	15.55	8.97	0.34	5.12	0.22	0.66	0.35	0.26
6	16.46	15.39	0.89	1.22	0.51	0.46	0.66	0.46
7	16.45	11.42	<DL	2.02	0.33	0.60	0.47	0.34
8	13.66	9.35	0.14	0.61	0.25	0.37	0.37	0.28
9	15.51	10.59	<DL	1.03	0.37	0.40	0.46	0.36
10	16.45	9.99	0.21	1.37	0.32	0.33	0.45	0.33
11	16.13	10.99	0.31	0.67	0.33	0.29	0.47	0.34
12	16.13	10.83		0.55	0.46		0.56	0.37
13	14.22	11.64		2.88	1.63		0.57	0.38
14	14.98	8.94		0.96	0.37		0.44	0.31
15	26.08	8.28		9.07	0.48		0.39	0.28
16	18.46	5.69		5.19	0.25		0.31	0.24
17	13.84	6.89		3.01	0.35		0.39	0.28
18	13.40	11.07		0.46	0.52		0.56	0.38
19	15.43	10.55		0.40	0.50		0.56	0.38
FB stg. 1.1								
FB stg. 1.1								
FB stg. 2.1								
FB stg 2.2								
R^2 for POV	0.03	0.45	0.17	0.13	0.11	0.20	0.29	0.30
R^2 for PWV	0.02	0.24	0.00	0.22	0.32	0.45	0.39	0.36

Table A1. Production and chemistry data by Well Number. (Cont.)						
Well Number	Pb	Tl	Cr	Co	Cd	Mo
	µg/L	µg/L	µg/L	µg/L	µg/L	µg/L
1	105.49	98.94	16.13	28.82	13.16	4.54
2	<DL	13.09	39.96	13.27	<DL	8.77
3	26.40	39.72	25.69	15.90	<DL	<DL
4	3.81	20.00	29.51	12.10	<DL	11.20
5	2.68	20.17	74.27	16.26	<DL	8.50
6	49.62	136.37	41.08	74.42	42.49	32.86
7	7.05	25.59	29.69	26.40	6.93	11.43
8	10.27	26.95	18.20	22.82	4.75	14.11
9	27.64	53.87	39.50	44.11	19.64	43.51
10	69.24	60.81	27.69	23.64	5.08	22.43
11	70.01	62.77	26.03	23.37	4.01	15.97
12	25.65	92.51	8.98	30.22	4.16	6.05
13	751.83	122.88	246.03	41.74	5.56	31.04
14	<DL	74.62	161.52	24.34	<DL	<DL
15	262.79	43.69	39.14	20.31	<DL	6.20
16	11.40	39.89	<DL	15.92	<DL	<DL
17	1213.25	183.32	39.64	21.91	18.25	4.74
18	211.56	121.55	28.93	33.02	5.27	8.91
19	367.59	176.68	8.77	41.58	47.15	<DL
FB stg. 1.1						
FB stg. 1.1						
FB stg. 2.1						
FB stg 2.2						
R^2 for POV	0.00	0.08	0.00	0.26	0.15	0.16
R^2 for PWV	0.04	0.29	0.00	0.19	0.04	0.18

APPENDIX B

SUPPLEMENTAL TABLES FOR PAPER II: EXPERIMENTAL PHYSIOCHEMICAL INVESTIGATION OF HIGH-TEMPERATURE BRINE-SHALE INTERACTIONS

Table B1. List of instrument detection limits by component, source, and dilution.							
Source	MST			UTEP			
Dilution	Base	1:5	1:10	Base	1:75	1:300	1:350
Si (µM)	0.07	0.36	0.71	0.36	27.00	108.00	126.00
Al (µM)	0.04	0.19		0.08	0.01	24.00	28.00
Fe (µM)	0.72	3.58		0.01	0.00	4.00	4.67
K (µM)	0.51	2.56		5.12	383.63	1534.50	1790.25
Ca (µM)	1.00	4.99		3.99	299.25	1197.00	1396.50
Na (µM)	0.02	0.09					
Mg (µM)	0.05	0.27		1.23	92.25	369.00	430.50
S (µM)	15.59	77.97	155.93	0.31	23.25	93.00	108.50
Ti (nM)	8.36	41.78					
Ba (nM)	1.46	7.28		0.06	4.40	17.60	20.53
Mn (nM)	7.28	36.40		0.19	14.00	56.00	65.33
P (µM)	0.43	2.15		0.24	18.00	72.00	84.00
Sr (nM)	11.41	0.06	0.11	0.20	15.00	60.00	70.00
HCO3 (µM)	327.80			327.80			
Ni (nM)				1.19	89.00	356.00	415.33
Co (nM)	6.79	0.03		0.05	4.00	16.00	18.67
Zn (nM)	7.65	38.24		22.67	1700.00	6800.00	7933.33
Pb (nM)	4.83	24.13		0.00	0.01	0.05	0.06
Cu (nM)	12.59	62.94		0.19	14.00	56.00	65.33
As (nM)	13.35	66.74		0.08	6.00	24.00	28.00
Li (µM)	0.14	0.72					
B (µM)	0.19	0.93		0.05	4.00	16.00	18.67

Table B2a. Measurements of pH and element component concentration by the experimental run.						
	Time (hrs.)	pH	Si (mM)	Al (mM)	Fe (mM)	K (mM)
DIW-2-0.08h	0.08	2.4	0.251	0.034	0.084	0.371
DIW-2-0.25h	0.25	2.3	-	0.041	0.100	0.426
DIW-2-0.5h	0.5	2.46	0.816	0.045	0.130	0.532
DIW-2-1.5h	1.5	3.37	-	0.051	0.255	0.864
DIW-2-1.5h-R	1.5	3.3	-	0.055	0.260	0.845
DIW-2-3h	3	3.97	0.815	0.029	0.219	1.293
DIW-2-1d	24	7.3	0.573	0.001	0.065	1.555
DIW-2-3d	72	7.48	-	BDL	0.067	1.473
DIW-2-7d	168	7.32	0.570	BDL	0.070	1.411
DIW-2-7d-R	168	7.02	0.589	BDL	0.074	1.437
DIW-2-7d-R2	168	6.68	0.545	-	-	-
DIW-2-14d	336	6.91	0.670	BDL	0.084	1.426
DIW-2-28d	672	7.19	-	BDL	0.101	1.357
DIW-2-56d	1344	7.2	1.165	BDL	0.086	1.419
DIW-4-0.08h	0.08	9.57	0.038	BDL	BDL	0.172
DIW-4-0.25h	0.25	9.72	-	BDL	BDL	0.228
DIW-4-0.5h	0.5	9.77	0.116	BDL	BDL	0.256
DIW-4-1.5h	1.5	9.76	-	0.035	BDL	0.330
DIW-4-1.5h-R	1.5	9.73	-	0.044	0.004	0.319
DIW-4-3h	3	9.67	0.298	0.035	BDL	0.357
DIW-4-1d	24	8.85	0.523	0.010	BDL	0.596
DIW-4-3d	72	8.27	-	0.001	BDL	0.828
DIW-4-7d	168	7.97	0.656	0.001	BDL	0.978
DIW-4-7d-R	168	7.9	0.654	BDL	BDL	1.013
DIW-4-7d-R2	168	7.61	0.680	-	-	-
DIW-4-14d	336	7.52	0.773	BDL	0.009	1.066
DIW-4-28d	672	7.6	-	BDL	0.020	1.141
DIW-4-56d	1344	7.69	1.258	BDL	0.037	1.120
DIW-6-0.08h	0.08	9.82	0.047	0.010	BDL	0.193
DIW-6-0.25h	0.25	9.77	-	0.015	BDL	0.245
DIW-6-0.5h	0.5	9.66	0.097	0.023	BDL	0.264
DIW-6-1.5h	1.5	9.67	-	0.036	BDL	0.331
DIW-6-1.5h-R	1.5	9.8	-	0.045	BDL	0.336
DIW-6-3h	3	9.74	0.312	0.036	BDL	0.387
DIW-6-1d	24	9.03	0.443	0.011	BDL	0.582
DIW-6-3d	72	8.31	-	0.002	BDL	0.837

Table B2a. Measurements of pH and element component concentration by the experimental run. (Cont)						
	Time (hrs.)	pH	Si (mM)	Al (mM)	Fe (mM)	K (mM)
DIW-6-7d	168	7.71	0.623	0.001	0.004	0.968
DIW-6-7d-R	168	7.81	0.608	0.001	BDL	0.984
DIW-6-7d-R2	168	7.54	0.660	-	-	-
DIW-6-14d	336	7.62	0.721	BDL	0.009	1.015
DIW-6-28d	672	7.71	0.623	0.001	0.004	0.968
DIW-6-56d	1344	7.68	1.305	BDL	0.039	1.053
3.2-Na-2-0.08h	0.08	2.78	0.117	0.162	0.066	2.190
3.2-Na-2-0.5h	0.5	3.08	0.246	0.166	0.081	2.642
3.2-Na-2-3h	3	6.6	0.204	0.009	0.002	3.465
3.2-Na-2-1d	24	7.23	0.238	0.009	BDL	3.513
3.2-Na-2-7d	168	7.22	0.318	0.011	0.011	2.544
3.2-Na-2-7dR	168	7.04	0.314	-	-	-
3.2-Na-2-7dR2	168	6.98	0.312	-	-	-
3.2-Na-2-14d	336	7.22	0.422	0.007	BDL	2.798
3.2-Na-2-56d	1344	7.31	0.724	0.013	0.050	2.5442
3.2-Na-4-0.08h	0.08	9.12	0.248	0.017	0.086	1.172
3.2-Na-4-0.5h	0.5	8.92	0.067	0.022	0.080	1.873
3.2-Na-4-3h	3	8.59	0.096	0.025	BDL	2.636
3.2-Na-4-1d	24	7.89	0.507	0.008	BDL	2.679
3.2-Na-4-7d	168	7.29	0.291	0.011	0.002	2.747
3.2-Na-4-7dR	168	7.47	0.283	-	-	-
3.2-Na-4-7dR2	168	7.38	0.284	-	-	-
3.2-Na-4-14d	336	7.39	0.443	0.009	BDL	2.780
3.2-Na-4-56d	1344	7.06	0.521	BDL	BDL	2.8124
3.2-Na-6-0.08h	0.08	9.36	0.000	0.010	BDL	1.202
3.2-Na-6-0.5h	0.5	9.2	0.152	0.016	BDL	1.902
3.2-Na-6-3h	3	8.7	0.104	0.022	BDL	2.670
3.2-Na-6-1d	24	8.11	0.222	0.011	BDL	2.783
3.2-Na-6-7d	168	7	0.324	0.006	BDL	2.777
3.2-Na-6-7dR	168	6.84	0.311	-	-	-
3.2-Na-6-7dR2	168	7.34	0.345	-	-	-
3.2-Na-6-14d	336	7.42	0.539	0.008	BDL	2.820
3.2-Na-6-56d	1344	7.29	0.681	0.007	0.001	2.862
12-Na-2-0.08h	0.08	5.89	BDL	0.044	0.007	4.661
12-Na-2-0.5h	0.5	6.47	BDL	BDL	0.007	3.976
12-Na-2-3h	3	7.58	0.473	0.031	BDL	3.320

Table B2a. Measurements of pH and element component concentration by the experimental run. (Cont)						
	Time (hrs.)	pH	Si (mM)	Al (mM)	Fe (mM)	K (mM)
12-Na-2-1d	24	7.71	BDL	0.032	BDL	1.945
12-Na-2-7d	168	7.41	0.518	BDL	BDL	2.180
12-Na-2-7dR	168	6.9	BDL	-	-	-
12-Na-2-7dR2	168	7.06	BDL	-	-	-
12-Na-2-14d	336	7.18	BDL	0.043	BDL	2.304
12-Na-2-56d	1344	7.05	0.324	BDL	BDL	2.427
12-Na-4-0.08h	0.08	8.5	1.757	0.040	BDL	4.460
12-Na-4-0.5h	0.5	8.83	0.323	BDL	BDL	2.735
12-Na-4-3h	3	7.94	BDL	0.030	BDL	2.621
12-Na-4-1d	24	7.7	BDL	BDL	BDL	2.417
12-Na-4-7d	168	7.77	BDL	0.029	BDL	4.982
12-Na-4-7dR	168	7.39	BDL	BDL	-	-
12-Na-4-7dR2	168	7.28	BDL	BDL	-	-
12-Na-4-14d	336	6.99	BDL	BDL	BDL	1.997
12-Na-4-56d	1344	7.03	BDL	BDL	BDL	1.802
12-Na-6-0.25h	0.08	8.22	0.773	BDL	BDL	0.829
12-Na-6-0.5h	0.5	8.47	BDL	0.030	BDL	1.456
12-Na-6-3h	3	7.93	1.420	BDL	BDL	1.987
12-Na-6-1d	24	7.18	BDL	BDL	BDL	2.069
12-Na-6-7d	168	7.28	BDL	BDL	BDL	5.716
12-Na-6-7dR	168	7.14	BDL	-	-	-
12-Na-6-7dR2	168	7.33	BDL	-	-	-
12-Na-6-14d	336	7.89	2.342	BDL	BDL	1.993
12-Na-6-56d	1344	7.1	0.152	BDL	BDL	1.541
3.2-Mix-2-0.08h	0.08	1.92	0.151	0.110	0.064	-
3.2-Mix-2-0.5h	0.5	2.58	0.378	0.131	0.114	-
3.2-Mix-2-3h	3	6.36	0.474	BDL	0.001	-
3.2-Mix-2-1d	24	6.69	0.494	BDL	0.012	-
3.2-Mix-2-7d	168	6.8	0.521	BDL	0.002	-
3.2-Mix-2-7dR	168	6.71	0.509	-	-	-
3.2-Mix-2-7dR2	168	6.72	0.524	-	-	-
3.2-Mix-2-14d	336	6.69	0.603	BDL	BDL	-
3.2-Mix-2-56d	1344	6.72	1.033	BDL	0.002	-
3.2-Mix-4-0.08h	0.08	6.59	BDL	NDL	BDL	-
3.2-Mix-4-0.5h	0.5	6.96	0.108	0.007	BDL	-
3.2-Mix-4-3h	3	6.82	0.330	BDL	BDL	-

Table B2a. Measurements of pH and element component concentration by the experimental run. (Cont)						
	Time (hrs.)	pH	Si (mM)	Al (mM)	Fe (mM)	K (mM)
3.2-Mix-4-1d	24	6.91	0.469	BDL	BDL	-
3.2-Mix-4-7d	168	6.91	0.538	BDL	BDL	-
3.2-Mix-4-7dR	168	6.86	0.554	-	-	-
3.2-Mix-4-7dR2	168	6.79	0.531	-	-	-
3.2-Mix-4-14d	336	6.8	0.690	0.013	BDL	-
3.2-Mix-4-56d	1344	6.61	1.110	BDL	BDL	-
3.2-Mix-6-0.08h	0.08	6.78	BDL	BDL	BDL	-
3.2-Mix-6-0.5h	0.5	6.59	0.097	BDL	BDL	-
3.2-Mix-6-3h	3	6.82	0.310	BDL	BDL	-
3.2-Mix-6-1d	24	6.93	0.448	BDL	BDL	-
3.2-Mix-6-7d	168	6.73	0.520	BDL	BDL	-
3.2-Mix-6-7dR	168	6.77	0.537	-	-	-
3.2-Mix-6-7dR2	168	6.76	0.549	-	-	-
3.2-Mix-6-14d	336	6.59	0.714	BDL	BDL	-
3.2-Mix-6-56d	1344	6.34	1.101	BDL	0.001	-
12-Mix-2-0.08h	0.08	2.36	BDL	BDl	0.020	-
12-Mix-2-0.5h	0.5	3.29	BDL	0.029	0.022	-
12-Mix-2-3h	3	6.45	0.385	BDl	BDL	-
12-Mix-2-1d	24	6.28	0.387	BDL	0.011	-
12-Mix-2-7d	168	6.37	0.446	BDL	BDL	-
12-Mix-2-7dR	168	6.35	0.454	-	-	-
12-Mix-2-7dR2	168	6.36	0.465	-	-	-
12-Mix-2-14d	336	6.32	0.581	BDL	BDL	-
12-Mix-2-56d	1344	6.34	0.819	BDL	BDL	-
12-Mix-4-0.08h	0.08	5.9	BDL	0.038	BDL	-
12-Mix-4-0.5h	0.5	6.2	BDL	BDL	BDL	-
12-Mix-4-3h	3	6.24	0.311	BDL	BDL	-
12-Mix-4-1d	24	6.41	0.887	0.213	0.008	-
12-Mix-4-7d	168	6.23	0.499	0.104	0.014	-
12-Mix-4-7dR	168	6.32	0.506	BDL	BDL	-
12-Mix-4-7dR2	168	6.33	0.446	-	-	-
12-Mix-4-14d	336	6.49	0.523	-	-	-
12-Mix-4-56d	1344	6.41	0.787	BDL	BDL	-
12-Mix-6-0.08h	0.08	6.14	BDL	BDL	BDL	-
12-Mix-6-0.5h	0.5	5.98	BDL	0.057	BDL	-
12-Mix-6-3h	3	6.33	0.376	0.036	BDL	-

Table B2a. Measurements of pH and element component concentration by the experimental run. (Cont.)						
	Time (hrs.)	pH	Si (mM)	Al (mM)	Fe (mM)	K (mM)
12-Mix-6-1d	24	6.39	0.484	0.044	BDL	-
12-Mix-6-7d	168	6.38	0.490	0.044	BDL	-
12-Mix-6-7dR	168	6.36	0.496	-	-	-
12-Mix-6-7dR2	168	6.36	0.531	-	-	-
12-Mix-6-14d	336	6.47	0.581	BDL	BDL	-
12-Mix-6-56d	1344	6.14	0.867	0.037	BDL	-

Table B2b. Measurements of pH and element component concentration by the experimental run.						
	Ca (mM)	Na (mM)	Mg (mM)	S (mM)	Ti (uM)	Ba (uM)
DIW-2-0.08h	2.537	3.239	0.081	1.214	0.538	1.002
DIW-2-0.25h	2.895	3.346	0.095	-	0.653	1.076
DIW-2-0.5h	3.361	3.812	0.129	1.920	BDL	1.171
DIW-2-1.5h	5.352	4.748	0.267	-	0.957	1.676
DIW-2-1.5h-R	5.407	4.732	0.269	-	1.080	1.655
DIW-2-3h	8.315	4.854	0.366	1.938	1.514	2.075
DIW-2-1d	10.394	5.856	0.534	2.920	2.678	2.583
DIW-2-3d	11.189	6.934	0.582	-	BDL	2.013
DIW-2-7d	11.353	6.873	0.569	3.734	2.868	1.848
DIW-2-7d-R	12.230	6.537	0.733	5.640	2.737	1.363
DIW-2-7d-R2	-	-	-	10.330	-	-
DIW-2-14d	13.425	6.484	0.805	9.049	3.269	0.937
DIW-2-28d	15.541	6.292	0.813	-	4.586	0.606
DIW-2-56d	12.777	6.103	0.706	12.981	3.286	0.517
DIW-4-0.08h	0.049	3.071	0.002	0.850	0.224	0.021
DIW-4-0.25h	0.029	3.864	0.001	-	0.256	0.020
DIW-4-0.5h	0.018	4.197	0.002	1.430	0.265	0.039
DIW-4-1.5h	0.011	4.813	0.003	-	0.280	0.049
DIW-4-1.5h-R	BDL	4.858	0.004	-	0.301	0.044
DIW-4-3h	BDL	5.159	0.002	1.887	0.268	0.044
DIW-4-1d	0.037	6.537	0.006	2.969	0.291	0.089
DIW-4-3d	0.269	7.129	0.031	-	0.482	0.277
DIW-4-7d	0.778	7.187	0.088	5.408	0.788	0.531
DIW-4-7d-R	0.828	7.230	0.092	5.456	0.789	0.550
DIW-4-7d-R2	-	-	-	8.626	-	-
DIW-4-14d	1.978	6.949	0.179	8.764	1.291	0.608
DIW-4-28d	4.065	6.664	0.277	-	1.967	0.424
DIW-4-56d	6.817	6.162	0.369	23.350	3.171	0.629
DIW-6-0.08h	0.033	3.151	0.001	0.754	0.276	0.027
DIW-6-0.25h	0.036	4.003	0.001	-	0.272	0.036
DIW-6-0.5h	0.033	4.131	0.001	1.459	0.278	0.042
DIW-6-1.5h	0.013	4.720	0.001	-	0.261	0.054
DIW-6-1.5h-R	0.012	4.644	0.001	-	0.261	0.056
DIW-6-3h		4.781	0.001	1.961	0.270	0.045
DIW-6-1d	0.039	5.864	0.005	3.054	0.319	0.108
DIW-6-3d	0.302	6.723	0.031	-	0.520	0.334

Table B2b. Measurements of pH and element component concentration by the experimental run. (Cont.)						
	Ca (mM)	Na (mM)	Mg (mM)	S (mM)	Ti (uM)	Ba (uM)
DIW-6-7d	0.929	6.731	0.104	6.053	0.841	0.652
DIW-6-7d-R	0.895	6.625	0.097	6.137	0.874	0.604
DIW-6-7d-R2	-	-	-	12.942	-	-
DIW-6-14d	1.996	6.589	0.177	9.691	1.316	0.738
DIW-6-28d	0.929	6.731	0.104	6.053	0.841	0.652
DIW-6-56d	7.227	6.135	0.393	29.209	3.241	0.629
3.2-Na-2-0.08h	6.344	-	BDL	0.840	-	3.501
3.2-Na-2-0.5h	7.972	-	0.185	1.436	-	3.945
3.2-Na-2-3h	11.377	-	0.346	1.977	-	9.281
3.2-Na-2-1d	12.897	-	0.592	2.856	-	14.245
3.2-Na-2-7d	14.596	-	0.867	5.540	-	9.465
3.2-Na-2-7dR	-	-	-	7.548	-	-
3.2-Na-2-7dR2	-	-	-	9.350	-	-
3.2-Na-2-14d	19.723	-	1.129	10.314	-	4.552
3.2-Na-2-56d	34.843	-	1.268	23.590	-	3.502
3.2-Na-4-0.08h	5.576	-	0.151	1.100	-	1.655
3.2-Na-4-0.5h	5.913	-	0.154	1.656	-	2.790
3.2-Na-4-3h	2.844	-	0.114	2.047	-	7.691
3.2-Na-4-1d	4.117	-	0.305	2.882	-	10.689
3.2-Na-4-7d	7.354	-	0.697	6.202	-	7.371
3.2-Na-4-7dR	-	-	-	5.970	-	-
3.2-Na-4-7dR2	-	-	-	7.864	-	-
3.2-Na-4-14d	9.661	-	0.781	9.243	-	6.020
3.2-Na-4-56d	22.343	-	1.003	22.369	-	2.696
3.2-Na-6-0.08h	1.198	-	0.037	0.950	-	2.367
3.2-Na-6-0.5h	1.665	-	0.065	1.476	-	3.297
3.2-Na-6-3h	2.713	-	0.123	1.981	-	8.960
3.2-Na-6-1d	3.855	-	0.339	2.868	-	11.489
3.2-Na-6-7d	7.120	-	0.731	6.410	-	7.343
3.2-Na-6-7dR	-	-	-	6.271	-	-
3.2-Na-6-7dR2	-	-	-	8.405	-	-
3.2-Na-6-14d	9.798	-	0.818	9.350	-	5.405
3.2-Na-6-56d	22.717	-	1.058	22.526	-	3.073
12-Na-2-0.08h	2.008	-	BDL	0.753	-	3.776
12-Na-2-0.5h	2.270	-	BDL	1.070	-	2.424
12-Na-2-3h	4.279	-	BDL	1.507	-	12.647

Table B2b. Measurements of pH and element component concentration by the experimental run. (Cont.)						
	Ca (mM)	Na (mM)	Mg (mM)	S (mM)	Ti (uM)	Ba (uM)
12-Na-2-1d	4.803	-	BDL	2.129	-	19.695
12-Na-2-7d	7.161	-	0.720	4.312	-	16.996
12-Na-2-7dR	-	-	-	3.550	-	-
12-Na-2-7dR2	-	-	-	4.572	-	-
12-Na-2-14d	9.431	-	0.893	6.638	-	17.956
12-Na-2-56d	17.465	-	0.921	14.934	-	8.753
12-Na-4-0.08h	0.786	-	BDL	0.699	-	3.520
12-Na-4-0.5h	1.310	-	BDL	1.168	-	4.660
12-Na-4-3h	1.747	-	BDL	1.561	-	10.404
12-Na-4-1d	2.882	-	BDL	1.998	-	19.674
12-Na-4-7d	4.628	-	0.605	3.908	-	18.566
12-Na-4-7dR	-	-	-	3.308	-	-
12-Na-4-7dR2	-	-	-	4.654	-	-
12-Na-4-14d	10.479	-	0.734	9.400	-	11.029
12-Na-4-56d	16.592	-	0.907	15.000	-	7.606
12-Na-6-0.25h	0.524	-	BDL	0.688	-	3.435
12-Na-6-0.5h	0.873	-	BDL	1.179	-	5.462
12-Na-6-3h	1.659	-	BDL	1.627	-	12.257
12-Na-6-1d	2.707	-	BDL	1.867	-	21.719
12-Na-6-7d	4.541	-	0.518	3.766	-	18.672
12-Na-6-7dR	-	-	-	3.362	-	-
12-Na-6-7dR2	-	-	-	7.039	-	-
12-Na-6-14d	6.986	-	0.677	6.354	-	15.169
12-Na-6-56d	16.941	-	0.792	15.961	-	8.658
3.2-Mix-2-0.08h	-	-	-	0.773	-	2.185
3.2-Mix-2-0.5h	-	-	-	1.437	-	4.518
3.2-Mix-2-3h	-	-	-	1.828	-	14.664
3.2-Mix-2-1d	-	-	-	3.557	-	17.002
3.2-Mix-2-7d	-	-	-	9.893	-	5.858
3.2-Mix-2-7dR	-	-	-	8.747	-	-
3.2-Mix-2-7dR2	-	-	-	8.196	-	-
3.2-Mix-2-14d	-	-	-	15.069	-	8.251
3.2-Mix-2-56d	-	-	-	23.325	-	4.301
3.2-Mix-4-0.08h	-	-	-	1.201	-	1.452
3.2-Mix-4-0.5h	-	-	-	1.660	-	4.134
3.2-Mix-4-3h	-	-	-	0.381	-	12.651

Table B2b. Measurements of pH and element component concentration by the experimental run. (Cont.)						
	Ca (mM)	Na (mM)	Mg (mM)	S (mM)	Ti (uM)	Ba (uM)
3.2-Mix-4-1d	-	-	-	2.979	-	16.400
3.2-Mix-4-7d	-	-	-	8.759	-	11.751
3.2-Mix-4-7dR	-	-	-	7.976	-	-
3.2-Mix-4-7dR2	-	-	-	8.277	-	-
3.2-Mix-4-14d	-	-	-	7.964	-	10.651
3.2-Mix-4-56d	-	-	-	24.453	-	5.676
3.2-Mix-6-0.08h	-	-	-	1.330	-	1.784
3.2-Mix-6-0.5h	-	-	-	1.736	-	4.075
3.2-Mix-6-3h	-	-	-	1.887	-	12.621
3.2-Mix-6-1d	-	-	-	3.337	-	17.472
3.2-Mix-6-7d	-	-	-	8.372	-	13.583
3.2-Mix-6-7dR	-	-	-	8.802	-	-
3.2-Mix-6-7dR2	-	-	-	12.376	-	-
3.2-Mix-6-14d	-	-	-	12.743	-	10.385
3.2-Mix-6-56d	-	-	-	25.244	-	6.093
12-Mix-2-0.08h	-	-	-	1.169	-	0.000
12-Mix-2-0.5h	-	-	-	1.720	-	5.484
12-Mix-2-3h	-	-	-	1.479	-	13.919
12-Mix-2-1d	-	-	-	3.096	-	22.773
12-Mix-2-7d	-	-	-	8.487	-	16.980
12-Mix-2-7dR	-	-	-	9.000	-	-
12-Mix-2-7dR2	-	-	-	7.319	-	-
12-Mix-2-14d	-	-	-	12.134	-	22.527
12-Mix-2-56d	-	-	-	24.002	-	14.706
12-Mix-4-0.08h	-	-	-	1.369	-	2.915
12-Mix-4-0.5h	-	-	-	0.888	-	4.169
12-Mix-4-3h	-	-	-	1.938	-	13.096
12-Mix-4-1d	-	-	-	5.046	-	21.816
12-Mix-4-7d	-	-	-	8.009	-	24.391
12-Mix-4-7dR	-	-	-	6.453	-	-
12-Mix-4-7dR2	-	-	-	6.706	-	-
12-Mix-4-14d	-	-	-	12.169	-	20.051
12-Mix-4-56d	-	-	-	24.631	-	18.351
12-Mix-6-0.08h	-	-	-	1.269	-	2.552
12-Mix-6-0.5h	-	-	-	2.320	-	6.739
12-Mix-6-3h	-	-	-	3.470	-	17.292

Table B2b. Measurements of pH and element component concentration by the experimental run. (Cont.)						
	Ca (mM)	Na (mM)	Mg (mM)	S (mM)	Ti (uM)	Ba (uM)
12-Mix-6-1d	-	-	-	3.025	-	22.193
12-Mix-6-7d	-	-	-	7.185	-	27.431
12-Mix-6-7dR	-	-	-	9.002	-	-
12-Mix-6-7dR2	-	-	-	8.930	-	-
12-Mix-6-14d	-	-	-	12.016	-	20.080
12-Mix-6-56d	-	-	-	28.270	-	20.931

Table B2c. Measurements of pH and element component concentration by the experimental run. (Cont.)						
	Mn (uM)	P (mM)	Sr (uM)	HCO3 (mM)	Ni (uM)	Co (uM)
DIW-2-0.08h	5.776	0.043	19.694	BDL	-	0.218
DIW-2-0.25h	6.929	0.041	-	BDL	-	0.330
DIW-2-0.5h	8.006	0.036	43.691	BDL	-	0.460
DIW-2-1.5h	12.400	0.027	-	BDL	-	0.721
DIW-2-1.5h-R	12.500	0.028	-	BDL	-	0.739
DIW-2-3h	15.804	BDL	43.555	BDL	-	0.674
DIW-2-1d	10.484	BDL	49.983	0.853	-	0.074
DIW-2-3d	10.509	BDL	-	0.609	-	0.070
DIW-2-7d	6.995	BDL	51.027	0.487	-	0.054
DIW-2-7d-R	12.110	BDL	54.459	0.366	-	0.083
DIW-2-7d-R2	-	-	61.197	0.487	-	-
DIW-2-14d	10.512	BDL	60.559	0.487	-	0.078
DIW-2-28d	7.495	BDL	-	0.366	-	0.074
DIW-2-56d	3.588	BDL	71.914	0.366	-	0.070
DIW-4-0.08h	BDL	BDL	0.780	0.244	-	BDL
DIW-4-0.25h	BDL	BDL	-	0.366	-	BDL
DIW-4-0.5h	BDL	BDL	0.459	0.487	-	BDL
DIW-4-1.5h	BDL	BDL	-	0.609	-	BDL
DIW-4-1.5h-R	BDL	BDL	-	0.853	-	BDL
DIW-4-3h	BDL	BDL	0.382	0.853	-	BDL
DIW-4-1d	BDL	BDL	0.899	1.218	-	BDL
DIW-4-3d	0.132	BDL	-	1.097	-	BDL
DIW-4-7d	0.479	BDL	7.597	0.609	-	BDL
DIW-4-7d-R	0.518	BDL	8.205	0.731	-	BDL
DIW-4-7d-R2	-	-	11.895	0.731	-	-
DIW-4-14d	0.975	BDL	16.150	0.731	-	BDL
DIW-4-28d	1.376	BDL	-	0.487	-	BDL
DIW-4-56d	1.526	BDL	41.613	0.487	-	BDL
DIW-6-0.08h	BDL	BDL	0.633	0.366	-	BDL
DIW-6-0.25h	BDL	BDL	-	0.366	-	BDL
DIW-6-0.5h	BDL	BDL	0.683	0.366	-	BDL
DIW-6-1.5h	BDL	BDL	-	0.609	-	BDL
DIW-6-1.5h-R	BDL	BDL	-	0.609	-	BDL
DIW-6-3h	BDL	BDL	0.324	0.731	-	BDL
DIW-6-1d	BDL	BDL	0.874	1.097	-	BDL
DIW-6-3d	0.175	BDL	-	1.097	-	BDL

Table B2c. Measurements of pH and element component concentration by the experimental run. (Cont.)						
	Mn (uM)	P (mM)	Sr (uM)	HCO3 (mM)	Ni (uM)	Co (uM)
DIW-6-7d	0.609	BDL	8.752	0.731	-	BDL
DIW-6-7d-R	0.607	BDL	8.457	0.975	-	BDL
DIW-6-7d-R2	-	-	13.743	0.731	-	-
DIW-6-14d	1.146	BDL	15.333	0.609	-	BDL
DIW-6-28d	0.609	BDL	-	0.731	-	BDL
DIW-6-56d	1.441	BDL	42.852	0.609	-	BDL
3.2-Na-2-0.08h	13.455	0.019	24.393	BDL	0.301	0.354
3.2-Na-2-0.5h	15.933	0.019	39.899	BDL	1.288	0.616
3.2-Na-2-3h	14.400	BDL	63.038	0.366	0.249	0.264
3.2-Na-2-1d	16.754	BDL	75.351	1.097	0.187	0.079
3.2-Na-2-7d	14.639	BDL	76.446	0.487	0.422	0.124
3.2-Na-2-7dR	-	-	84.036	0.719	-	-
3.2-Na-2-7dR2	-	-	86.824	0.719	-	-
3.2-Na-2-14d	19.598	BDL	93.681	0.731	3.484	0.065
3.2-Na-2-56d	12.889	BDL	114.915	0.487	0.364	0.168
3.2-Na-4-0.08h	1.042	BDL	16.870	0.122	BDL	0.078
3.2-Na-4-0.5h	0.970	BDL	28.235	0.366	BDL	0.067
3.2-Na-4-3h	1.239	BDL	48.405	0.487	BDL	0.008
3.2-Na-4-1d	3.944	BDL	57.721	0.609	0.302	0.005
3.2-Na-4-7d	7.504	BDL	64.939	0.731	BDL	0.039
3.2-Na-4-7dR	-	-	62.239	0.719	-	-
3.2-Na-4-7dR2	-	-	67.111	0.719	-	-
3.2-Na-4-14d	7.706	BDL	70.300	0.731	0.354	0.035
3.2-Na-4-56d	8.116	BDL	102.234	0.609	BDL	0.031
3.2-Na-6-0.08h	0.075	BDL	18.120	0.122	0.103	BDL
3.2-Na-6-0.5h	0.220	BDL	29.496	0.244	0.513	0.005
3.2-Na-6-3h	0.917	BDL	52.833	0.366	BDL	0.020
3.2-Na-6-1d	3.752	BDL	60.657	0.609	0.098	0.024
3.2-Na-6-7d	7.785	BDL	68.397	0.731	BDL	0.022
3.2-Na-6-7dR	-	-	70.412	0.719	-	-
3.2-Na-6-7dR2	-	-	77.322	0.719	-	-
3.2-Na-6-14d	8.274	BDL	73.442	0.731	BDL	0.032
3.2-Na-6-56d	7.964	BDL	100.022	0.609	3.121	0.036
12-Na-2-0.08h	5.932	BDL	24.105	0.122	BDL	BDL
12-Na-2-0.5h	5.398	BDL	31.613	0.244	BDL	BDL
12-Na-2-3h	6.002	BDL	57.596	0.609	BDL	BDL

Table B2c. Measurements of pH and element component concentration by the experimental run. (Cont.)						
	Mn (uM)	P (mM)	Sr (uM)	HCO3 (mM)	Ni (uM)	Co (uM)
12-Na-2-1d	9.592	BDL	57.452	0.731	BDL	BDL
12-Na-2-7d	15.942	BDL	65.795	0.853	1.102	BDL
12-Na-2-7dR	-	-	63.682	0.719	-	-
12-Na-2-7dR2	-	-	69.616	0.839	-	-
12-Na-2-14d	14.759	BDL	70.725	0.609	BDL	BDL
12-Na-2-56d	11.892	BDL	88.461	0.609	BDL	BDL
12-Na-4-0.08h	0.421	BDL	15.807	0.244	BDL	BDL
12-Na-4-0.5h	0.502	BDL	33.408	0.366	7.844	BDL
12-Na-4-3h	1.301	BDL	51.991	0.244	BDL	BDL
12-Na-4-1d	3.849	BDL	54.867	0.487	BDL	BDL
12-Na-4-7d	8.680	BDL	52.200	0.853	BDL	BDL
12-Na-4-7dR	-	-	53.232	0.839	-	-
12-Na-4-7dR2	-	-	56.103	0.839	-	-
12-Na-4-14d	11.061	BDL	75.223	0.853	BDL	BDL
12-Na-4-56d	10.996	BDL	87.733	0.609	BDL	BDL
12-Na-6-0.25h	0.124	BDL	14.514	0.244	BDL	BDL
12-Na-6-0.5h	0.389	BDL	29.996	0.487	BDL	BDL
12-Na-6-3h	1.101	BDL	48.914	0.366	BDL	BDL
12-Na-6-1d	3.147	BDL	53.760	0.487	BDL	0.046
12-Na-6-7d	8.702	BDL	60.870	0.853	BDL	0.022
12-Na-6-7dR	-	-	62.293	0.958	-	-
12-Na-6-7dR2	-	-	62.903	0.719	-	-
12-Na-6-14d	10.310	BDL	63.214	0.853	BDL	0.018
12-Na-6-56d	11.585	BDL	88.228	0.609	BDL	0.022
3.2-Mix-2-0.08h	13.878	BDL	0.000	BDL	0.355	0.364
3.2-Mix-2-0.5h	27.171	BDL	10.075	BDL	0.994	1.085
3.2-Mix-2-3h	34.416	BDL	49.746	0.359	0.865	0.839
3.2-Mix-2-1d	50.702	BDL	34.801	0.479	0.544	0.559
3.2-Mix-2-7d	71.606	BDL	49.581	0.479	0.595	0.394
3.2-Mix-2-7dR	-	-	45.760	0.479	-	-
3.2-Mix-2-7dR2	-	-	49.104	0.359	-	-
3.2-Mix-2-14d	68.664	BDL	73.024	0.479	0.095	0.290
3.2-Mix-2-56d	48.018	BDL	81.890	0.599	0.165	0.177
3.2-Mix-4-0.08h	0.957	BDL	0.000	0.240	BDL	0.046
3.2-Mix-4-0.5h	1.528	BDL	15.897	0.240	BDL	0.070
3.2-Mix-4-3h	8.027	BDL	5.784	0.359	BDL	0.124

Table B2c. Measurements of pH and element component concentration by the experimental run. (Cont.)						
	Mn (uM)	P (mM)	Sr (uM)	HCO3 (mM)	Ni (uM)	Co (uM)
3.2-Mix-4-1d	30.563	BDL	26.395	0.359	0.134	0.189
3.2-Mix-4-7d	47.292	BDL	30.240	0.479	0.134	0.252
3.2-Mix-4-7dR	-	-	18.826	0.479	-	-
3.2-Mix-4-7dR2	-	-	24.072	0.479	-	-
3.2-Mix-4-14d	43.275	BDL	43.747	0.479	0.184	0.217
3.2-Mix-4-56d	38.541	BDL	61.586	0.479	BDL	0.161
3.2-Mix-6-0.08h	0.747	BDL	0.000	0.240	BDL	0.041
3.2-Mix-6-0.5h	1.573	BDL	17.723	0.240	BDL	0.075
3.2-Mix-6-3h	7.648	BDL	9.217	0.359	0.147	0.119
3.2-Mix-6-1d	30.160	BDL	30.215	0.359	BDL	0.176
3.2-Mix-6-7d	47.815	BDL	33.237	0.479	0.094	0.256
3.2-Mix-6-7dR	-	-	27.522	0.479	-	-
3.2-Mix-6-7dR2	-	-	36.593	0.479	-	-
3.2-Mix-6-14d	42.419	BDL	40.289	0.479	0.209	0.204
3.2-Mix-6-56d	41.314	BDL	79.678	0.479	0.094	0.175
12-Mix-2-0.08h	7.496	BDL	20.051	BDL	BDL	0.188
12-Mix-2-0.5h	10.866	BDL	68.797	BDL	0.417	0.488
12-Mix-2-3h	19.329	BDL	36.548	0.240	3.598	0.855
12-Mix-2-1d	45.689	BDL	86.925	0.359	2.410	0.996
12-Mix-2-7d	68.348	BDL	82.774	0.359	BDL	0.761
12-Mix-2-7dR	-	-	112.449	0.359	-	-
12-Mix-2-7dR2	-	-	120.540	0.359	-	-
12-Mix-2-14d	67.727	BDL	64.778	0.240	0.879	0.556
12-Mix-2-56d	74.234	BDL	104.679	0.359	BDL	0.423
12-Mix-4-0.08h	1.363	BDL	43.049	0.240	0.639	0.077
12-Mix-4-0.5h	1.581	BDL	68.722	0.240	0.432	0.148
12-Mix-4-3h	10.033	BDL	46.221	0.240	BDL	0.369
12-Mix-4-1d	38.273	BDL	39.574	0.240	2.250	0.567
12-Mix-4-7d	63.144	BDL	67.651	0.359	4.158	0.748
12-Mix-4-7dR	-	-	81.692	0.359	-	-
12-Mix-4-7dR2	-	-	51.140	0.359	-	-
12-Mix-4-14d	64.772	BDL	47.946	0.359	1.695	0.566
12-Mix-4-56d	71.138	BDL	68.907	0.359	1.213	0.461
12-Mix-6-0.08h	1.054	BDL	71.011	0.240	0.233	0.063
12-Mix-6-0.5h	2.476	BDL	36.268	0.240	0.441	0.171
12-Mix-6-3h	11.447	BDL	24.929	0.240	0.257	0.452

Table B2c. Measurements of pH and element component concentration by the experimental run. (Cont.)						
	Mn (uM)	P (mM)	Sr (uM)	HCO3 (mM)	Ni (uM)	Co (uM)
12-Mix-6-1d	38.473	BDL	44.695	0.240	0.211	0.584
12-Mix-6-7d	38.473	BDL	172.540	0.359	0.303	0.104
12-Mix-6-7dR	-	-	65.201	0.359	-	-
12-Mix-6-7dR2	-	-	66.980	0.359	-	-
12-Mix-6-14d	63.139	BDL	82.915	0.359	BDL	BDL
12-Mix-6-56d	70.531	BDL	109.873	0.359	0.058	0.519

Table B2d. Measurements of pH and element component concentration by the experimental run.						
	Zn (uM)	Pb (uM)	Cu (uM)	As (uM)	Li (mM)	B (mM)
DIW-2-0.08h	1.201	0.098	0.924	BDL	0.002	0.003
DIW-2-0.25h	0.968	0.112	0.868	BDL	0.001	0.005
DIW-2-0.5h	0.947	0.138	0.928	BDL	0.003	0.007
DIW-2-1.5h	0.976	0.153	0.897	BDL	0.011	0.015
DIW-2-1.5h-R	1.002	0.158	0.882	BDL	0.010	0.015
DIW-2-3h	1.129	0.103	0.566	BDL	0.020	0.027
DIW-2-1d	BDL	BDL	BDL	BDL	0.034	0.036
DIW-2-3d	BDL	BDL	0.040	BDL	0.037	0.038
DIW-2-7d	BDL	0.027	0.049	BDL	0.037	0.039
DIW-2-7d-R	0.899	BDL	0.059	BDL	0.039	0.040
DIW-2-7d-R2	-	-	-	-	-	-
DIW-2-14d	BDL	0.027	0.063	BDL	0.040	0.038
DIW-2-28d	BDL	0.033	0.083	BDL	0.042	0.036
DIW-2-56d	0.528	0.047	0.086	0.117	0.040	0.033
DIW-4-0.08h	BDL	BDL	BDL	BDL	0.001	0.003
DIW-4-0.25h	BDL	BDL	BDL	BDL	0.002	0.007
DIW-4-0.5h	BDL	BDL	BDL	BDL	0.002	0.011
DIW-4-1.5h	BDL	BDL	BDL	BDL	0.004	0.020
DIW-4-1.5h-R	BDL	BDL	BDL	0.115	0.004	0.023
DIW-4-3h	BDL	BDL	BDL	0.145	0.005	0.028
DIW-4-1d	BDL	BDL	BDL	0.163	0.015	0.033
DIW-4-3d	BDL	BDL	BDL	BDL	0.022	0.036
DIW-4-7d	0.612	BDL	BDL	BDL	0.027	0.039
DIW-4-7d-R	0.059	BDL	BDL	BDL	0.028	0.038
DIW-4-7d-R2	-	-	-	-	-	-
DIW-4-14d	1.239	BDL	BDL	BDL	0.031	0.039
DIW-4-28d	0.085	BDL	0.071	BDL	0.036	0.036
DIW-4-56d	4.167	0.030	0.090	BDL	0.035	0.033
DIW-6-0.08h	BDL	BDL	BDL	BDL	BDL	0.004
DIW-6-0.25h	BDL	BDL	BDL	BDL	0.002	0.007
DIW-6-0.5h	BDL	BDL	BDL	BDL	0.002	0.010
DIW-6-1.5h	BDL	BDL	BDL	0.111	0.004	0.024
DIW-6-1.5h-R	BDL	BDL	BDL	0.111	0.003	0.024
DIW-6-3h	BDL	BDL	BDL	0.125	0.006	0.027
DIW-6-1d	BDL	BDL	BDL	0.157	0.012	0.033
DIW-6-3d	BDL	BDL	BDL	BDL	0.022	0.036

Table B2d. Measurements of pH and element component concentration by the experimental run. (Cont.)						
	Zn (uM)	Pb (uM)	Cu (uM)	As (uM)	Li (mM)	B (mM)
DIW-6-7d	BDL	BDL	BDL	BDL	0.029	0.037
DIW-6-7d-R	BDL	BDL	BDL	BDL	0.028	0.037
DIW-6-7d-R2	-	-	-	-	-	-
DIW-6-14d	1.559	BDL	BDL	BDL	0.031	0.038
DIW-6-28d	BDL	BDL	BDL	BDL	BDL	BDL
DIW-6-56d	BDL	0.028	0.090	BDL	0.038	0.034
3.2-Na-2-0.08h	4.068	0.129	1.560	0.134	-	0.016
3.2-Na-2-0.5h	7.888	0.144	1.480	0.117	-	0.034
3.2-Na-2-3h	3.117	BDL	1.042	0.096	-	0.070
3.2-Na-2-1d	2.349	BDL	0.768	0.077	-	0.087
3.2-Na-2-7d	5.473	BDL	0.977	0.057	-	0.086
3.2-Na-2-7dR	-	-	-	-	-	-
3.2-Na-2-7dR2	-	-	-	-	-	-
3.2-Na-2-14d		BDL	0.397	0.020	-	0.098
3.2-Na-2-56d	10.540	BDL	1.148	0.298	-	0.093
3.2-Na-4-0.08h	10.087	BDL	0.967	0.643	-	0.010
3.2-Na-4-0.5h	7.886	BDL	0.823	0.485	-	0.026
3.2-Na-4-3h	3.516	BDL	0.441	BDL	-	0.058
3.2-Na-4-1d	BDL	BDL	0.070	BDL	-	0.075
3.2-Na-4-7d	3.210	BDL	0.759	BDL	-	0.082
3.2-Na-4-7dR	-	-	-	-	-	-
3.2-Na-4-7dR2	-	-	-	-	-	-
3.2-Na-4-14d	BDL	BDL	0.421	BDL	-	0.079
3.2-Na-4-56d	BDL	BDL	BDL	BDL	-	0.097
3.2-Na-6-0.08h	BDL	BDL	0.142	0.020	-	0.004
3.2-Na-6-0.5h	BDL	BDL	0.160	0.017	-	0.020
3.2-Na-6-3h	BDL	BDL	0.263	0.046	-	0.061
3.2-Na-6-1d	BDL	BDL	0.269	0.054	-	0.086
3.2-Na-6-7d	BDL	BDL	0.383	0.057	-	0.091
3.2-Na-6-7dR	-	-	-	-	-	-
3.2-Na-6-7dR2	-	-	-	-	-	-
3.2-Na-6-14d		BDL	0.222	0.039	-	0.088
3.2-Na-6-56d	BDL	BDL	0.543	0.066	-	0.100
12-Na-2-0.08h	1.374	BDL	0.466	BDL	-	BDL
12-Na-2-0.5h	BDL	BDL	BDL	BDL	-	BDL
12-Na-2-3h	5.021	BDL	BDL	BDL	-	0.045

Table B2d. Measurements of pH and element component concentration by the experimental run. (Cont.)						
	Zn (uM)	Pb (uM)	Cu (uM)	As (uM)	Li (mM)	B (mM)
12-Na-2-1d	BDL	BDL	BDL	BDL	-	0.049
12-Na-2-7d	BDL	BDL	1.024	BDL	-	0.064
12-Na-2-7dR	-	-	-	-	-	-
12-Na-2-7dR2	-	-	-	-	-	-
12-Na-2-14d	BDL	BDL	1.668	BDL	-	0.056
12-Na-2-56d	BDL	BDL	1.964	0.052	-	0.070
12-Na-4-0.08h	BDL	BDL	1.102	0.057	-	BDL
12-Na-4-0.5h	BDL	BDL	2.883	BDL	-	BDL
12-Na-4-3h	BDL	BDL	2.136	0.063	-	0.028
12-Na-4-1d	BDL	BDL	1.979	0.104	-	0.062
12-Na-4-7d	BDL	BDL	2.289	0.073	-	0.054
12-Na-4-7dR	-	-	-	-	-	-
12-Na-4-7dR2	-	-	-	-	-	-
12-Na-4-14d	BDL	BDL	1.020	0.052	-	0.053
12-Na-4-56d	BDL	BDL	0.266	0.063	-	0.085
12-Na-6-0.25h	BDL	BDL	0.730	BDL	-	BDL
12-Na-6-0.5h	BDL	BDL	0.159	0.052	-	BDL
12-Na-6-3h	BDL	BDL	0.716	BDL	-	0.033
12-Na-6-1d	BDL	BDL	7.455	BDL	-	0.055
12-Na-6-7d	BDL	BDL	1.267	BDL	-	0.067
12-Na-6-7dR	-	-	-	-	-	-
12-Na-6-7dR2	-	-	-	-	-	-
12-Na-6-14d	BDL	BDL	1.037	BDL	-	0.075
12-Na-6-56d	BDL	BDL	0.260	BDL	-	0.072
3.2-Mix-2-0.08h	3.119	0.255	2.218	BDL	-	0.014
3.2-Mix-2-0.5h	2.652	0.482	2.260	BDL	-	0.036
3.2-Mix-2-3h	2.267	0.115	2.781	BDL	-	0.052
3.2-Mix-2-1d	BDL	0.041	1.526	BDL	-	0.047
3.2-Mix-2-7d	BDL	0.156	1.614	BDL	-	0.068
3.2-Mix-2-7dR	-	-	-	-	-	-
3.2-Mix-2-7dR2	-	-	-	-	-	-
3.2-Mix-2-14d	BDL	BDL	0.132	BDL	-	0.064
3.2-Mix-2-56d	BDL	BDL	0.802	BDL	-	0.072
3.2-Mix-4-0.08h	BDL	BDL	BDL	BDL	-	0.001
3.2-Mix-4-0.5h	BDL	BDL	BDL	BDL	-	0.012
3.2-Mix-4-3h	BDL	BDL	BDL	BDL	-	0.039

Table B2d. Measurements of pH and element component concentration by the experimental run. (Cont.)						
	Zn (uM)	Pb (uM)	Cu (uM)	As (uM)	Li (mM)	B (mM)
3.2-Mix-4-1d	BDL	0.116	0.306	BDL	-	0.039
3.2-Mix-4-7d	BDL		0.210	BDL	-	0.065
3.2-Mix-4-7dR	-	-	-	-	-	-
3.2-Mix-4-7dR2	-	-	-	-	-	-
3.2-Mix-4-14d	BDL	0.020	0.458	BDL	-	0.057
3.2-Mix-4-56d	BDL	BDL	BDL	BDL	-	0.064
3.2-Mix-6-0.08h	BDL	BDL	BDL	BDL	-	BDL
3.2-Mix-6-0.5h	BDL	BDL	0.338	BDL	-	0.023
3.2-Mix-6-3h	BDL	0.018	0.726	BDL	-	0.042
3.2-Mix-6-1d	BDL	BDL	0.062	BDL	-	0.055
3.2-Mix-6-7d	BDL	BDL	0.058	BDL	-	0.070
3.2-Mix-6-7dR	-	-	-	-	-	-
3.2-Mix-6-7dR2	-	-	-	-	-	-
3.2-Mix-6-14d	BDL	BDL	0.918	BDL	-	0.065
3.2-Mix-6-56d	BDL	BDL	0.096	BDL	-	0.070
12-Mix-2-0.08h	BDL	BDL	BDL	BDL	-	BDL
12-Mix-2-0.5h	BDL	0.092	1.153	BDL	-	0.030
12-Mix-2-3h	BDL	1.290	3.096	BDL	-	0.019
12-Mix-2-1d	BDL	1.961	3.435	BDL	-	0.026
12-Mix-2-7d	BDL	BDL	BDL	BDL	-	0.025
12-Mix-2-7dR	-	-	-	-	-	-
12-Mix-2-7dR2	-	-	-	-	-	-
12-Mix-2-14d	BDL	0.528	2.089	BDL	-	0.024
12-Mix-2-56d	BDL	BDL	BDL	BDL	-	0.043
12-Mix-4-0.08h	BDL	BDL	1.348	BDL	-	BDL
12-Mix-4-0.5h	BDL	BDL	BDL	BDL	-	BDL
12-Mix-4-3h	BDL	BDL	BDL	BDL	-	BDL
12-Mix-4-1d	BDL	1.347	4.210	BDL	-	0.036
12-Mix-4-7d	BDL	3.585	6.064	BDL	-	0.019
12-Mix-4-7dR	-	-	-	-	-	-
12-Mix-4-7dR2	-	-	-	-	-	-
12-Mix-4-14d	BDL	1.370	2.150	BDL	-	BDL
12-Mix-4-56d	BDL	0.388	2.697	BDL	-	0.023
12-Mix-6-0.08h	BDL	BDL	1.188	BDL	-	BDL
12-Mix-6-0.5h	BDL	BDL	3.074	BDL	-	BDL
12-Mix-6-3h	BDL	BDL	1.782	BDL	-	0.033

Table B2d. Measurements of pH and element component concentration by the experimental run. (Cont.)						
	Zn (uM)	Pb (uM)	Cu (uM)	As (uM)	Li (mM)	B (mM)
12-Mix-6-1d	BDL	BDL	1.680	BDL	-	0.022
12-Mix-6-7d	BDL	BDL	1.050	BDL	-	0.039
12-Mix-6-7dR	-	-	-	-	-	-
12-Mix-6-7dR2	-	-	-	-	-	-
12-Mix-6-14d	BDL	BDL	BDL	BDL	-	0.006
12-Mix-6-56d	BDL	BDL	BDL	BDL	-	0.020

APPENDIX C

SUPPLEMENTAL FIGURES FOR PAPER II: EXPERIMENTAL PHYSIOCHEMICAL INVESTIGATION OF HIGH-TEMPERATURE BRINE-SHALE INTERACTIONS

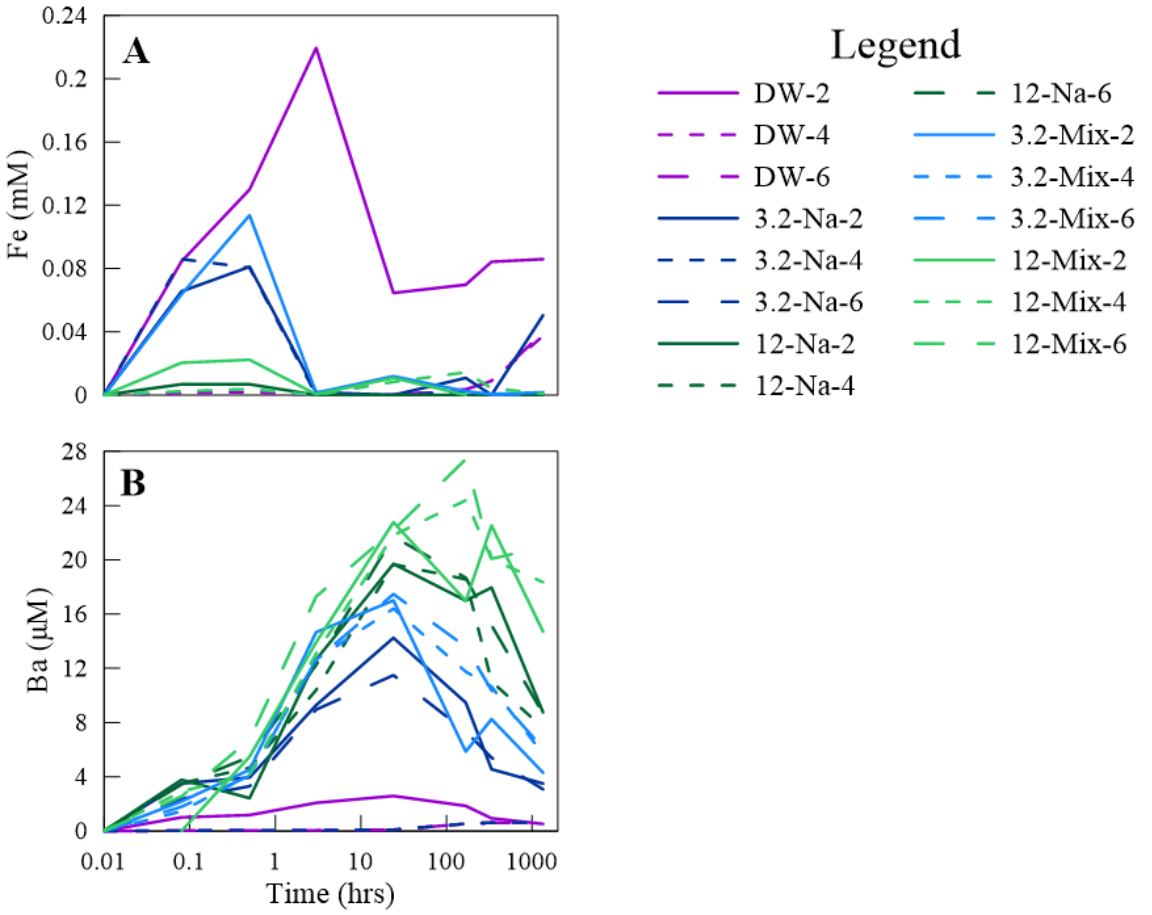

Figure C1. Concentrations of dissolved Fe (A) and Ba (B) for all experiments.

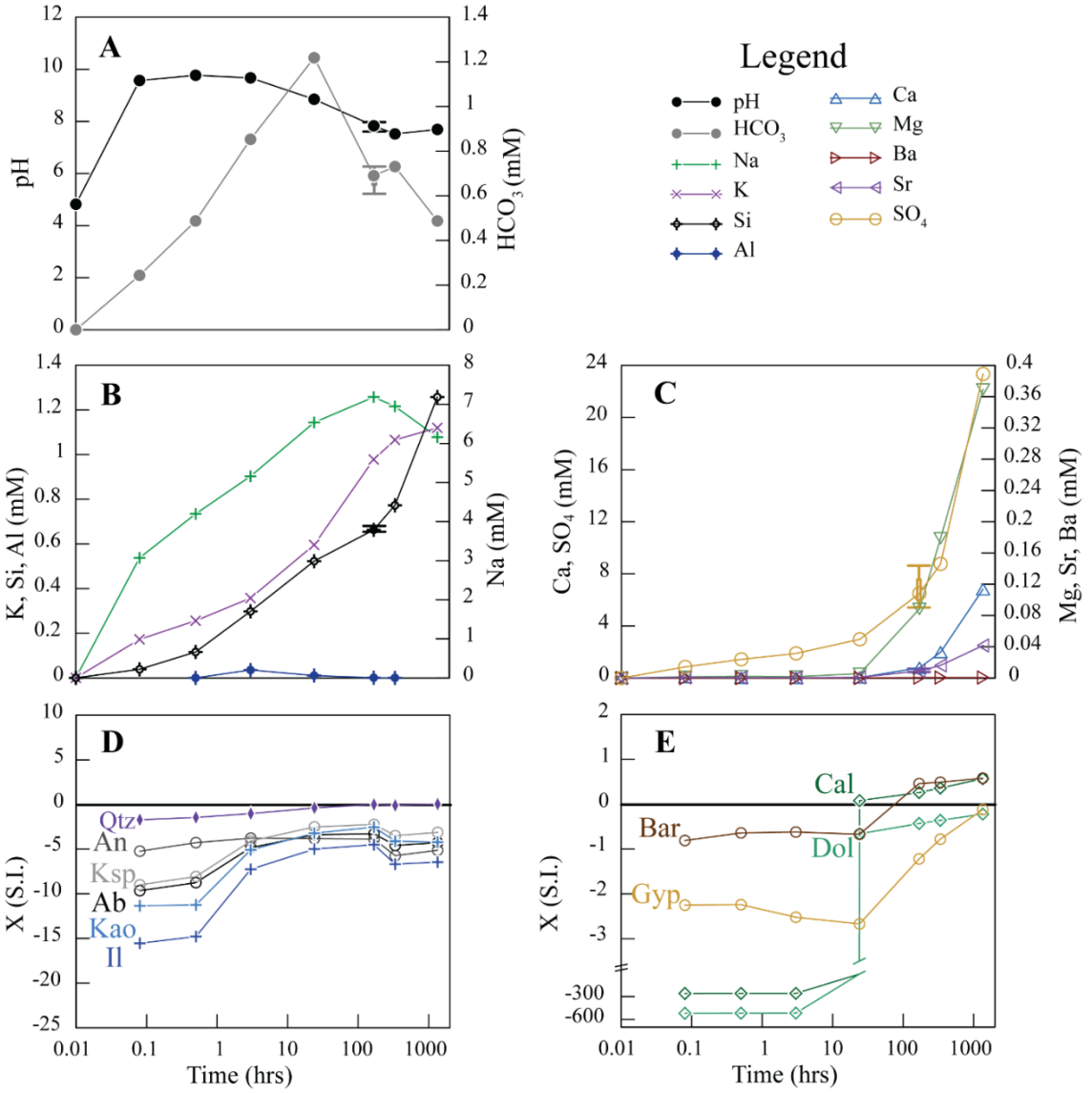

Figure C2. Changes in bulk chemistry and saturation indices for DW experimental solutions beginning at pH 4. Chemical data include HCO_3 and pH (A), concentrations of Si, Al, and K (B), concentrations of Ca, Mg, Sr, Ba, and SO_4 (C). Calculated saturation indices for quartz (Qtz), anorthite (An), kaolinite (Kao), potassium feldspar (Ksp), albite (Ab), and illite (Il) are shown in panel D, and those for calcite (Cal), dolomite (Dol), barite (Bar), and gypsum (Gyp) are shown in panel E. Error bars (1σ) for selected measurements are based on full experimental runs in completed in triplicate.

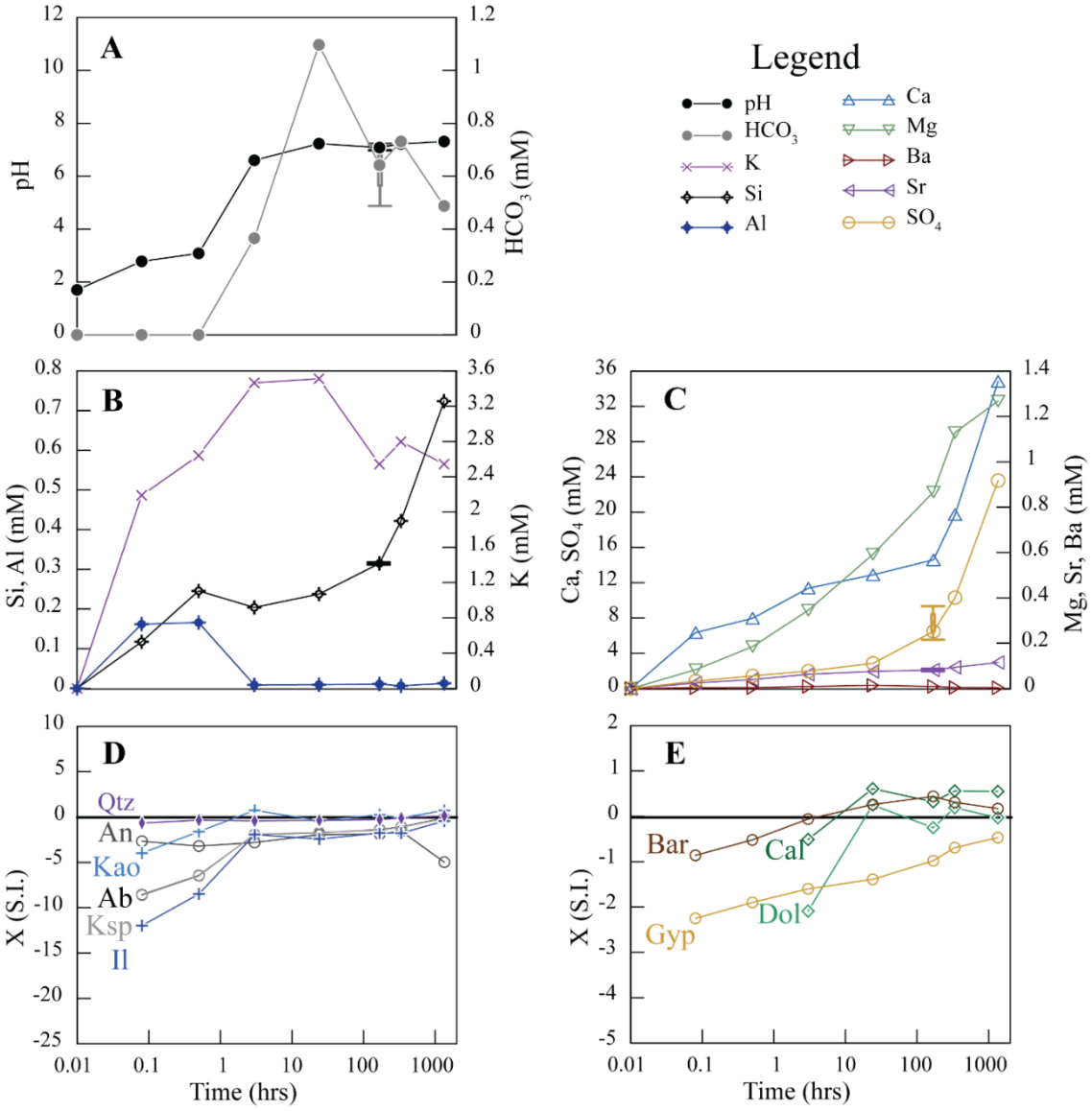

Figure C3. Changes in bulk chemistry and saturation indices for 3.2% TDS NaCl experimental solutions beginning at pH 2. Chemical data include HCO_3 and pH (A), concentrations of Si, Al, and K (B), concentrations of Ca, Mg, Sr, Ba, and SO_4 (C). Calculated saturation indices for quartz (Qtz), anorthite (An), kaolinite (Kao), potassium feldspar (Ksp), albite (Ab), and illite (Il) are shown in panel D, and those for calcite (Cal), dolomite (Dol), barite (Bar), and gypsum (Gyp) are shown in panel E. Error bars (1σ) for selected measurements are based on full experimental runs in completed in triplicate.

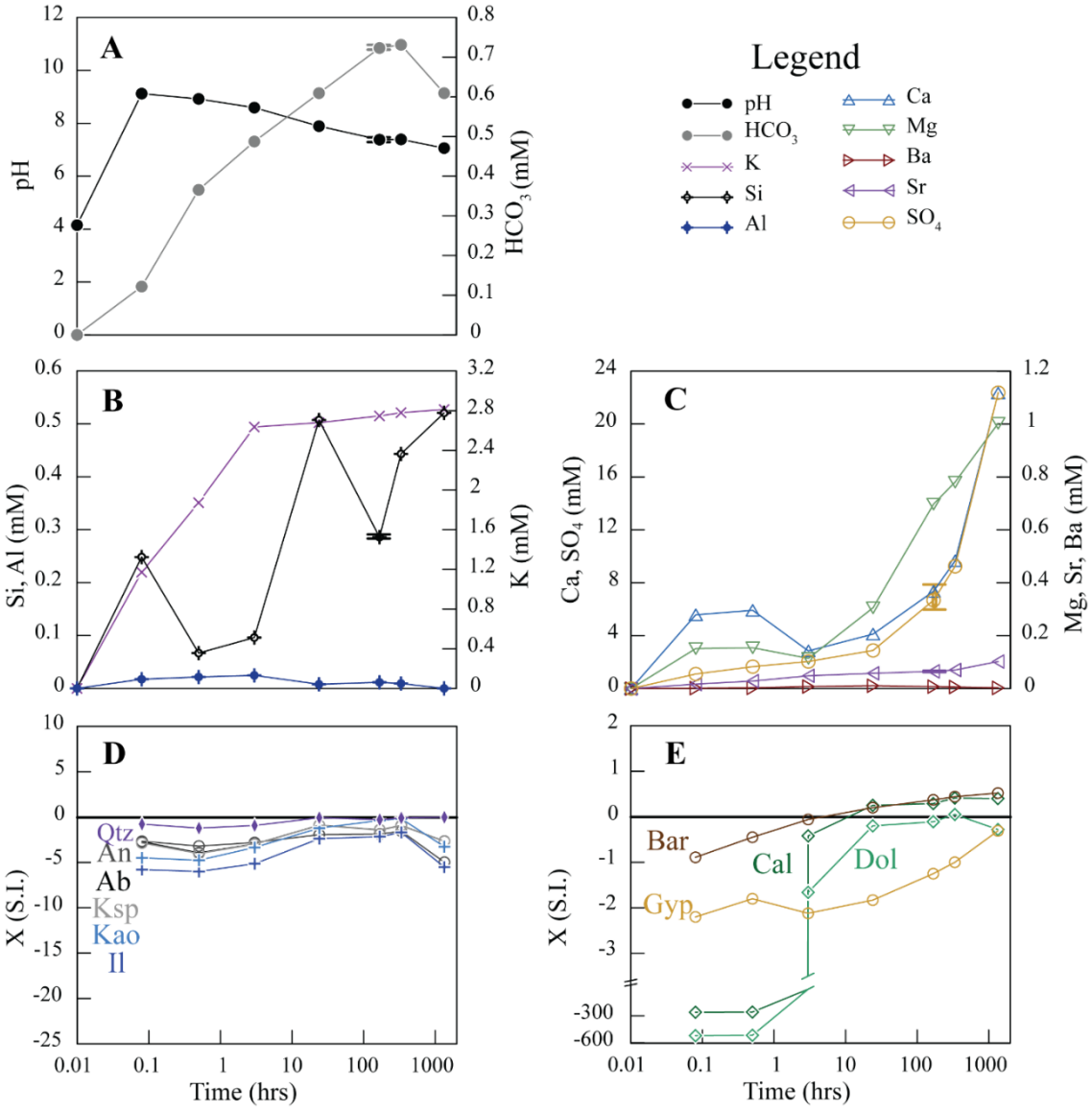

Figure C4. Changes in bulk chemistry and saturation indices for 3.2% TDS NaCl experimental solutions beginning at pH 4. Chemical data include HCO_3 and pH (A), concentrations of Si, Al, and K (B), concentrations of Ca, Mg, Sr, Ba, and SO_4 (C). Calculated saturation indices for quartz (Qtz), anorthite (An), kaolinite (Kao), potassium feldspar (Ksp), albite (Ab), and illite (Il) are shown in panel D, and those for calcite (Cal), dolomite (Dol), barite (Bar), and gypsum (Gyp) are shown in panel E. Error bars (1σ) for selected measurements are based on full experimental runs in completed in triplicate.

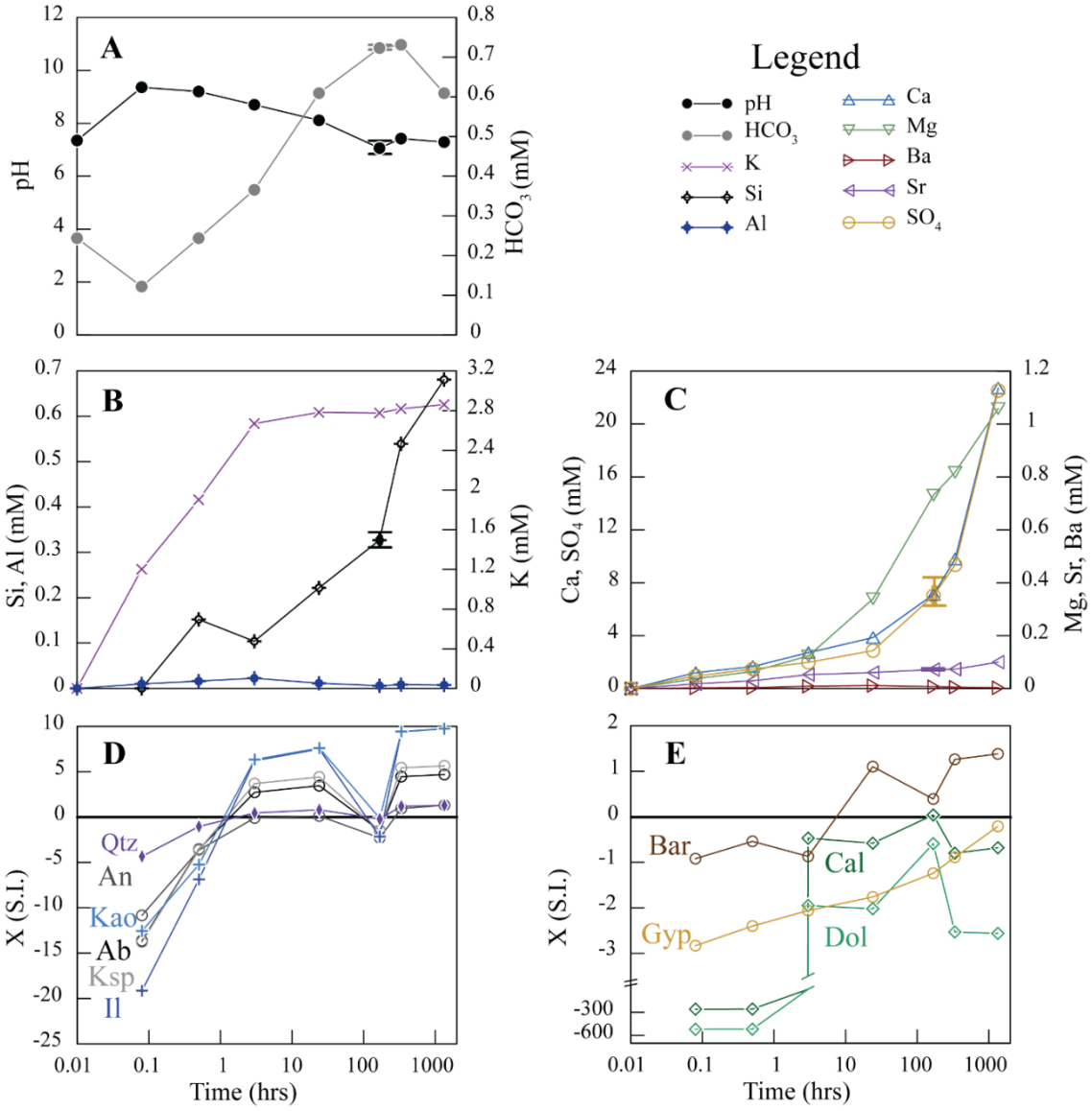

Figure C5. Changes in bulk chemistry and saturation indices for 3.2% TDS NaCl experimental solutions beginning at pH 6. Chemical data include HCO_3 and pH (A), concentrations of Si, Al, and K (B), concentrations of Ca, Mg, Sr, Ba, and SO_4 (C). Calculated saturation indices for quartz (Qtz), anorthite (An), kaolinite (Kao), potassium feldspar (Ksp), albite (Ab), and illite (Il) are shown in panel D, and those for calcite (Cal), dolomite (Dol), barite (Bar), and gypsum (Gyp) are shown in panel E. Error bars (1σ) for selected measurements are based on full experimental runs in completed in triplicate.

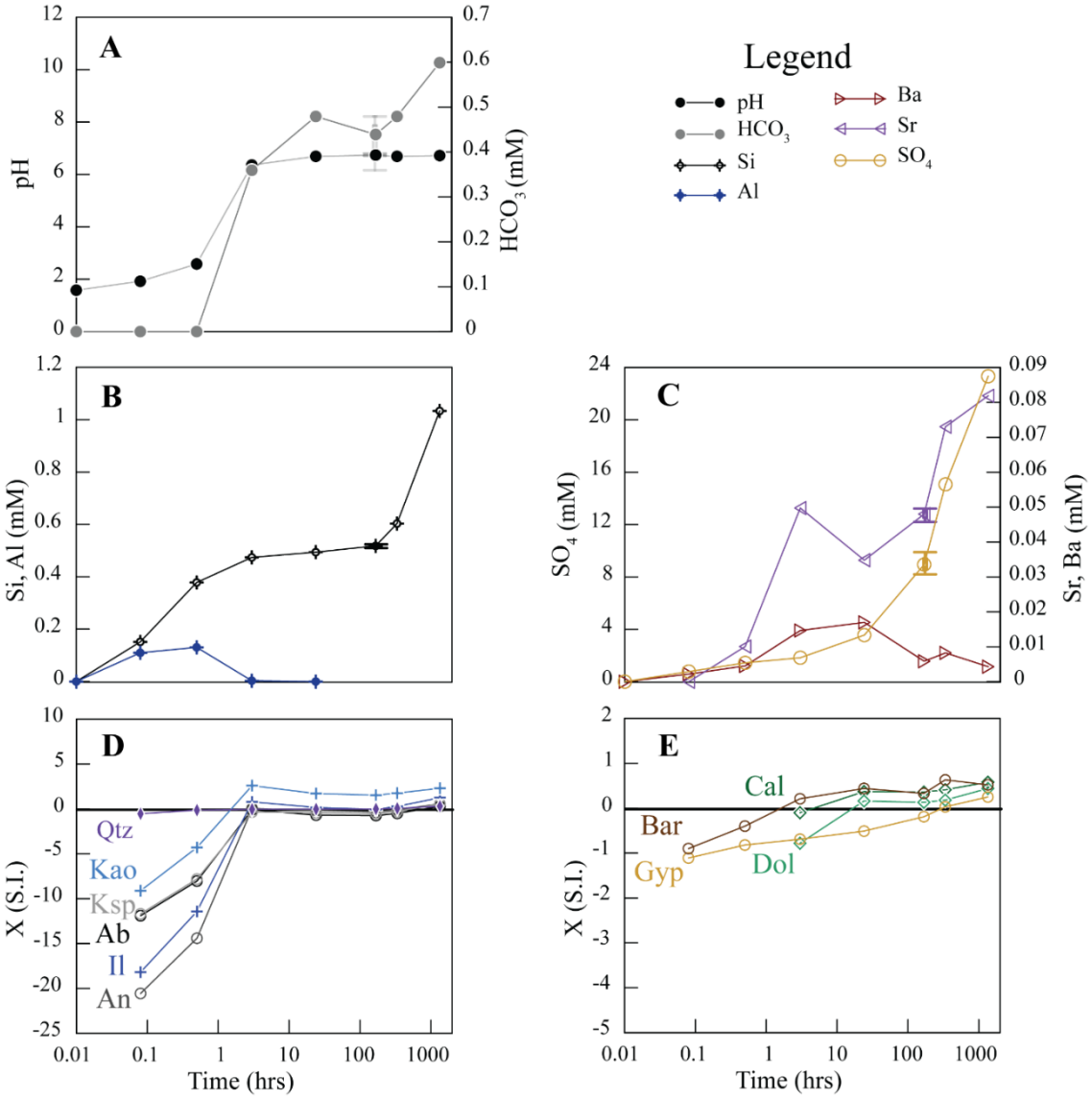

Figure C6. Changes in bulk chemistry and saturation indices for 3.2% TDS mixed composition experimental solutions beginning at pH 2. Chemical data include HCO_3 and pH (A), concentrations of Si, Al, and K (B), concentrations of Ca, Mg, Sr, Ba, and SO_4 (C). Calculated saturation indices for quartz (Qtz), anorthite (An), kaolinite (Kao), potassium feldspar (Ksp), albite (Ab), and illite (Il) are shown in panel D, and those for calcite (Cal), dolomite (Dol), barite (Bar), and gypsum (Gyp) are shown in panel E. Error bars (1σ) for selected measurements are based on full experimental runs in completed in triplicate.

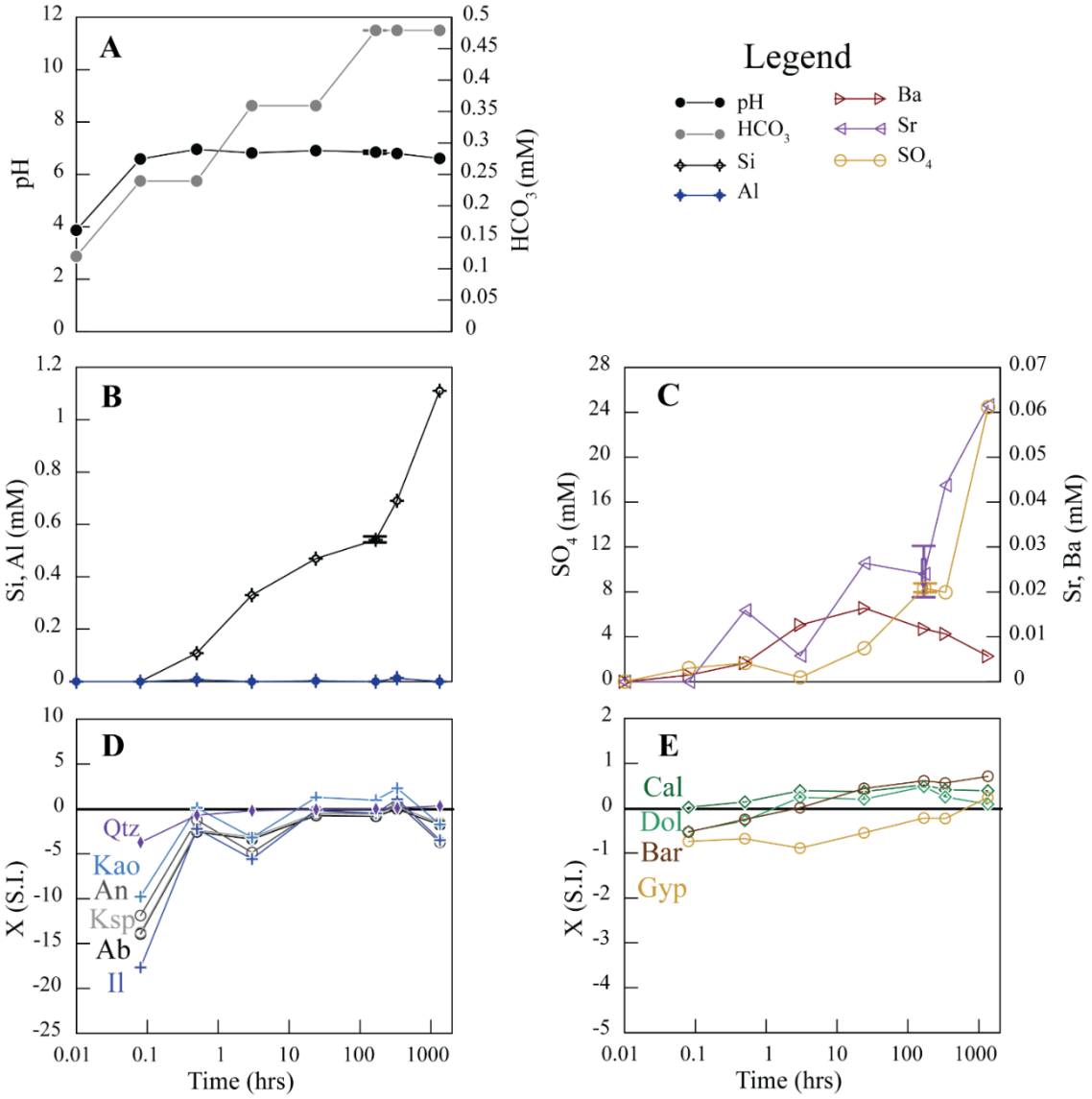

Figure C7. Changes in bulk chemistry and saturation indices for 3.2% TDS mixed composition experimental solutions beginning at pH 4. Chemical data include HCO_3 and pH (A), concentrations of Si, Al, and K (B), concentrations of Ca, Mg, Sr, Ba, and SO_4 (C). Calculated saturation indices for quartz (Qtz), anorthite (An), kaolinite (Kao), potassium feldspar (Ksp), albite (Ab), and illite (Il) are shown in panel D, and those for calcite (Cal), dolomite (Dol), barite (Bar), and gypsum (Gyp) are shown in panel E. Error bars (1σ) for selected measurements are based on full experimental runs in completed in triplicate.

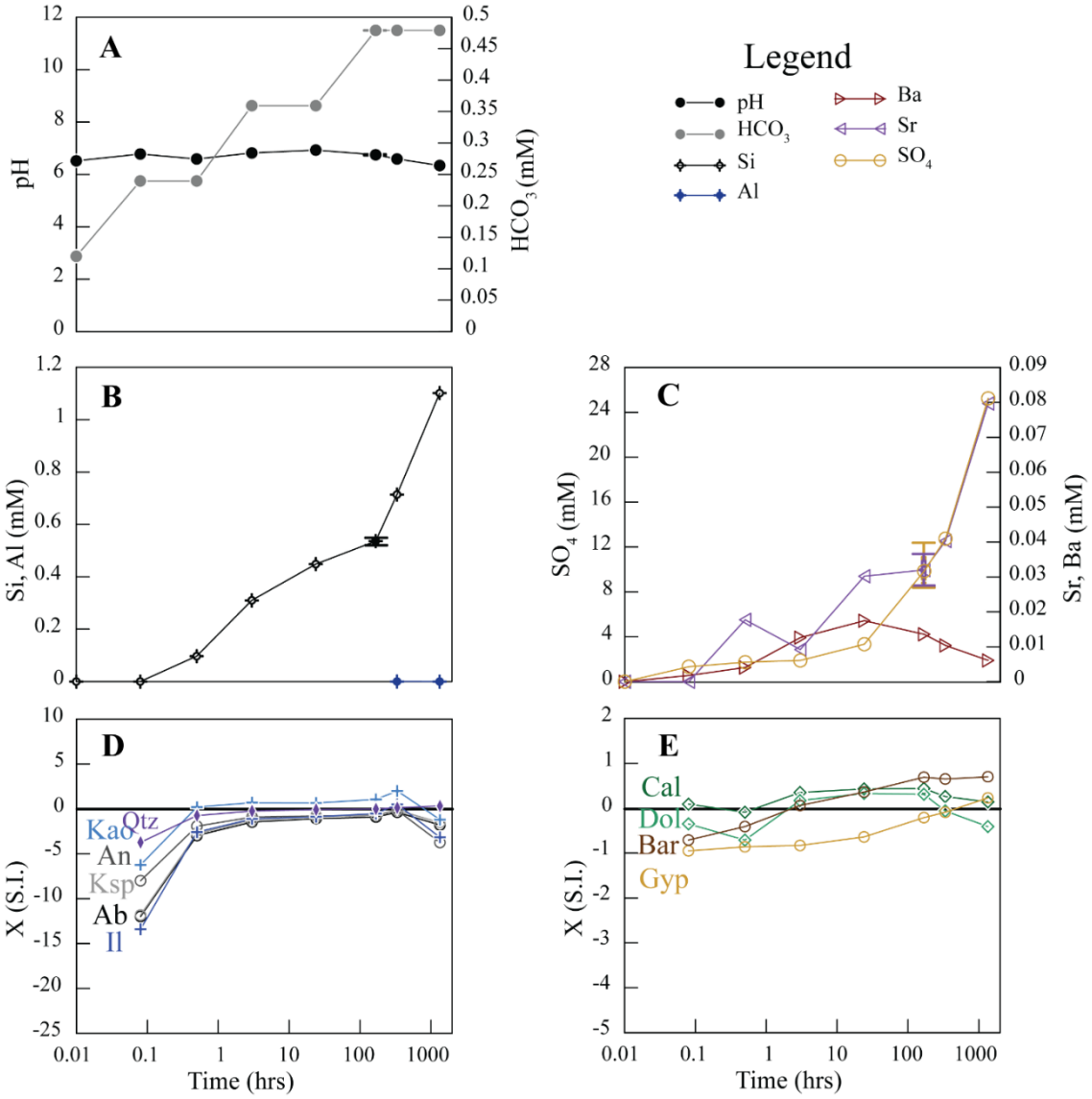

Figure C8. Changes in bulk chemistry and saturation indices for 3.2% TDS mixed composition experimental solutions beginning at pH 6. Chemical data include HCO_3 and pH (A), concentrations of Si, Al, and K (B), concentrations of Ca, Mg, Sr, Ba, and SO_4 (C). Calculated saturation indices for quartz (Qtz), anorthite (An), kaolinite (Kao), potassium feldspar (Ksp), albite (Ab), and illite (Il) are shown in panel D, and those for calcite (Cal), dolomite (Dol), barite (Bar), and gypsum (Gyp) are shown in panel E. Error bars (1σ) for selected measurements are based on full experimental runs in completed in triplicate.

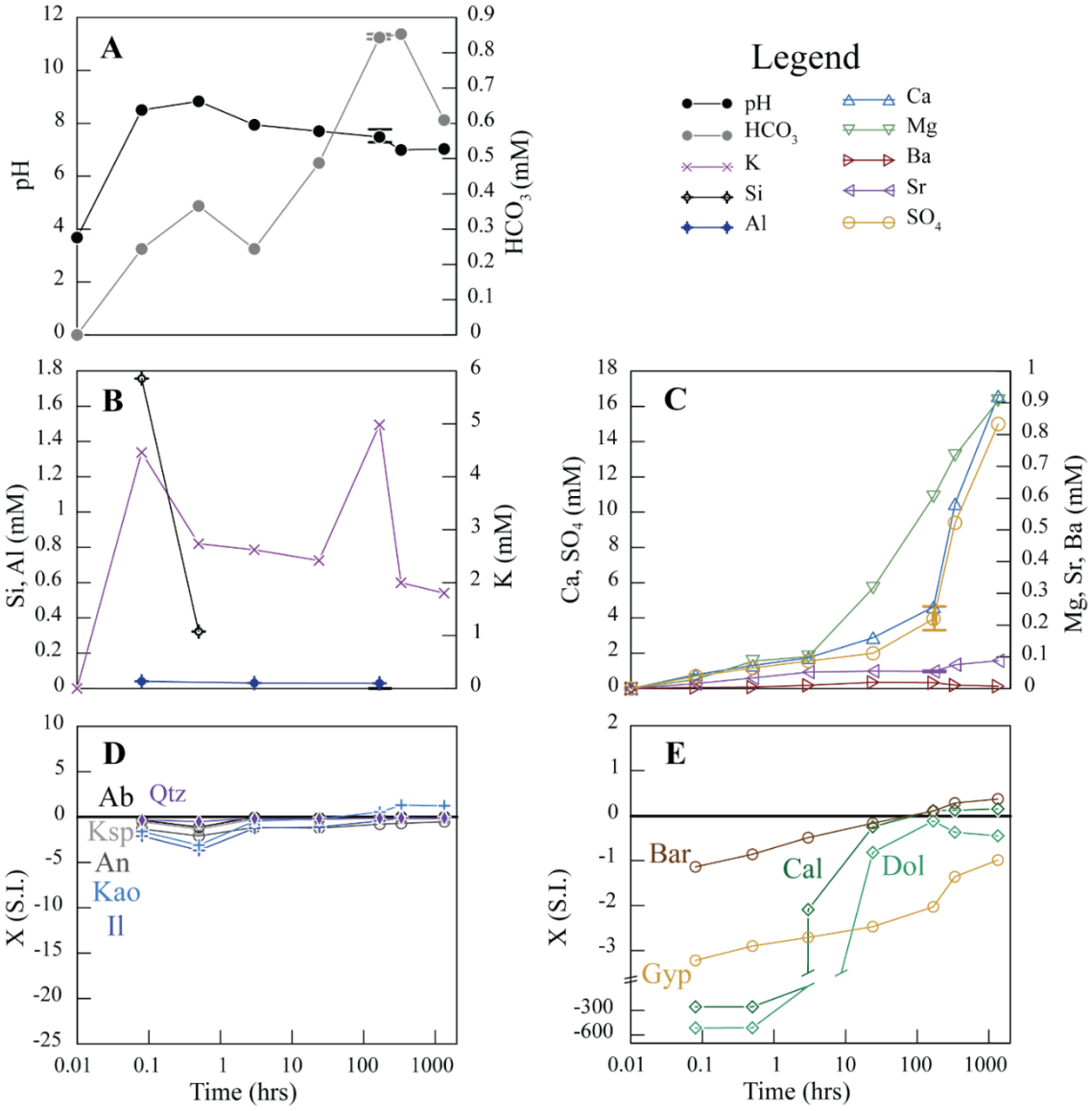

Figure C9. Changes in bulk chemistry and saturation indices for 12% TDS NaCl experimental solutions beginning at pH 4. Chemical data include HCO_3 and pH (A), concentrations of Si, Al, and K (B), concentrations of Ca, Mg, Sr, Ba, and SO_4 (C). Calculated saturation indices for quartz (Qtz), anorthite (An), kaolinite (Kao), potassium feldspar (Ksp), albite (Ab), and illite (Il) are shown in panel D, and those for calcite (Cal), dolomite (Dol), barite (Bar), and gypsum (Gyp) are shown in panel E. Error bars (1σ) for selected measurements are based on full experimental runs in completed in triplicate.

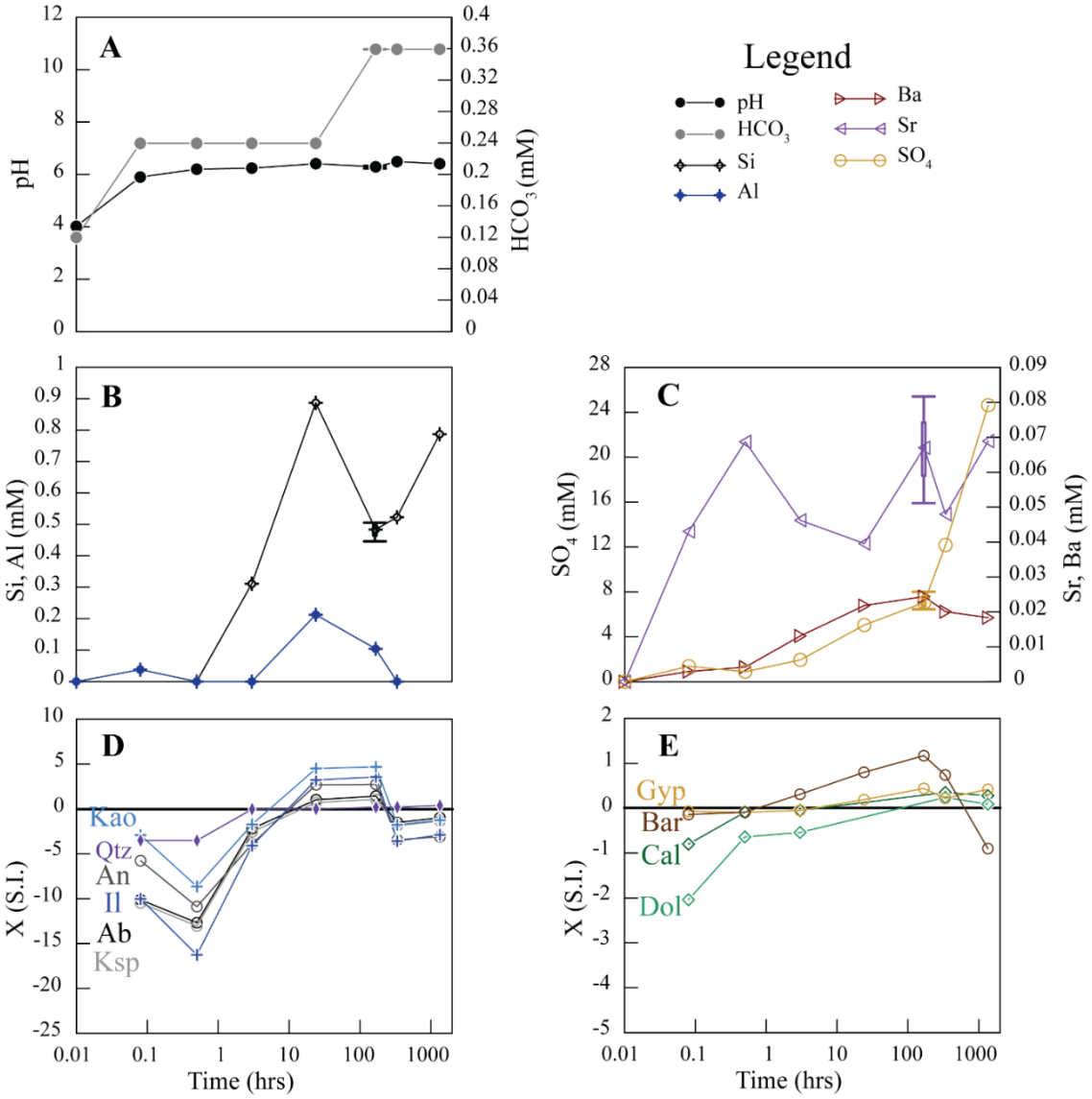

Figure C10. Changes in bulk chemistry and saturation indices for 12% TDS mixed composition experimental solutions beginning at pH 4. Chemical data include HCO_3 and pH (A), concentrations of Si, Al, and K (B), concentrations of Ca, Mg, Sr, Ba, and SO_4 (C). Calculated saturation indices for quartz (Qtz), anorthite (An), kaolinite (Kao), potassium feldspar (Ksp), albite (Ab), and illite (Il) are shown in panel D, and those for calcite (Cal), dolomite (Dol), barite (Bar), and gypsum (Gyp) are shown in panel E. Error bars (1σ) for selected measurements are based on full experimental runs in completed in triplicate.

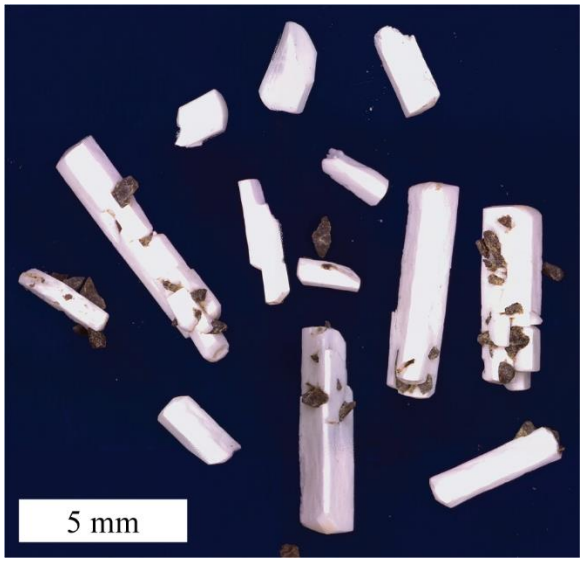

Figure C11. Photomicrograph of Gypsum crystals formed during DW-6-56 day experiment.

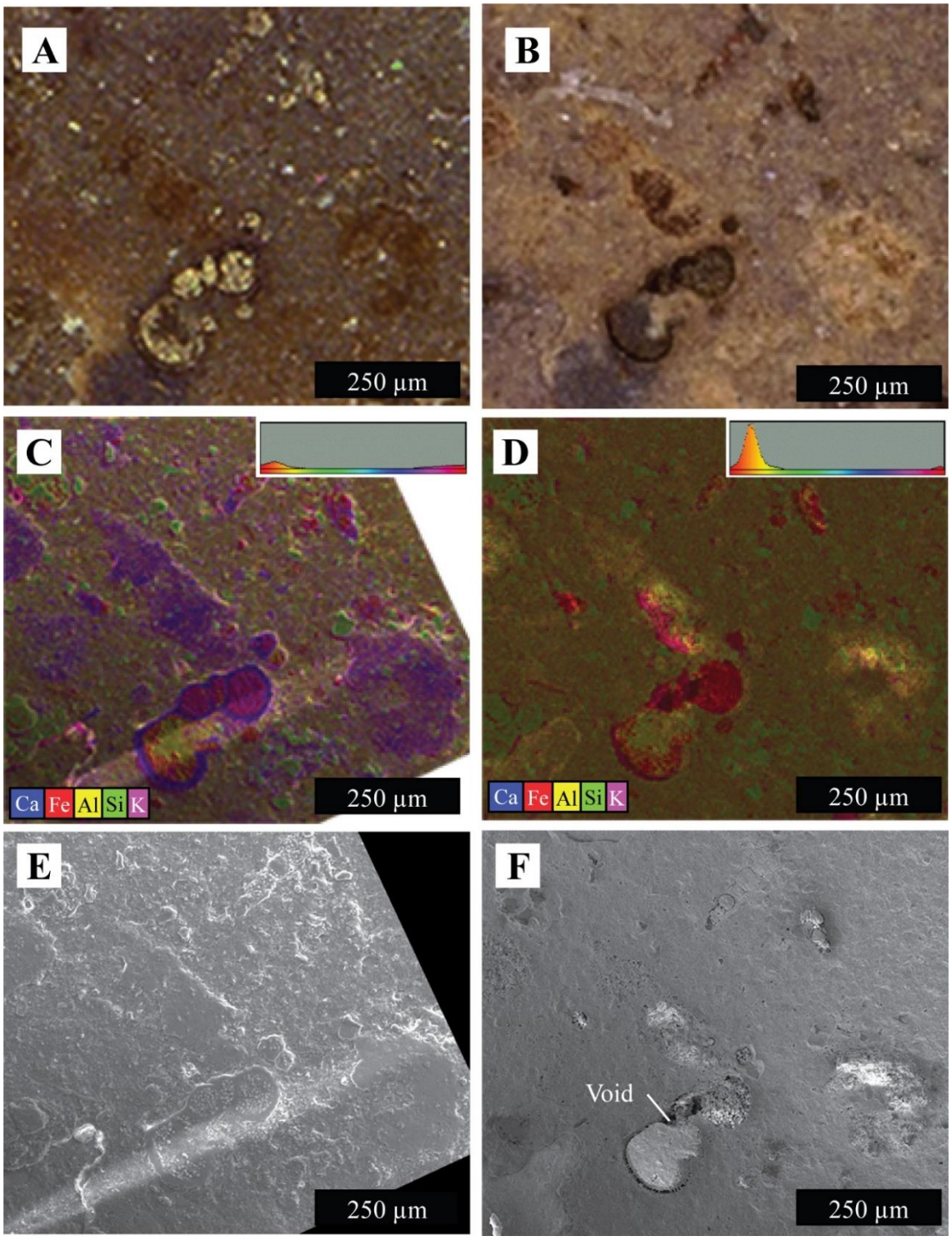

Figure C12. Images of mounted shale chips before (left) and after (right) to show physiological changes resulting from exposure to DIW water with initial pH of 2. Reflected light photomicroscope images (A and B) show evidence of carbonate shell dissolution and pyrite oxidation. False color EDS images (C and D) show Ca loss. SEM images (E and F) show void formation from the dissolution of carbonate shells.

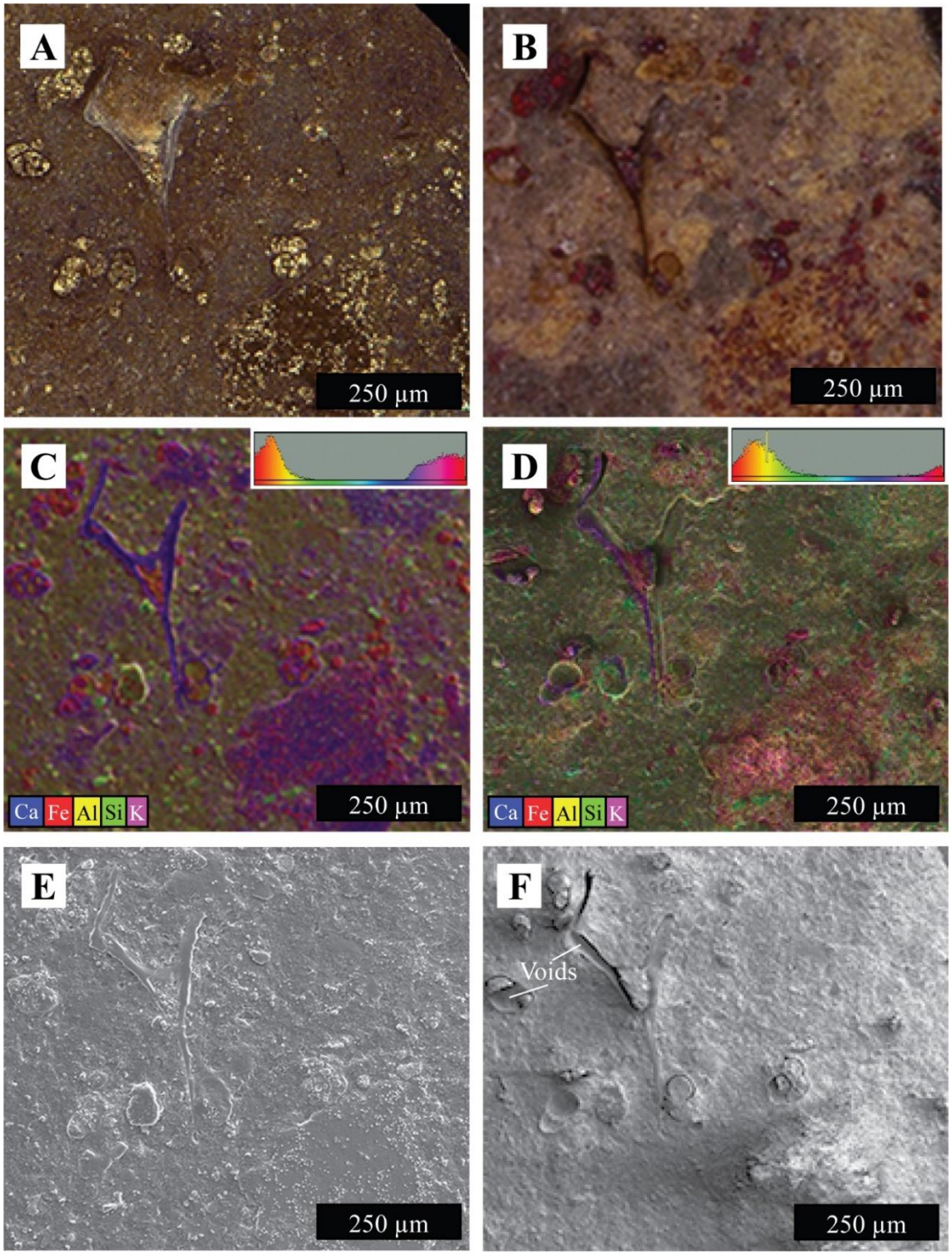

Figure C13. Images of mounted shale chips before (left) and after (right) to show physiological changes resulting from exposure to DIW water with initial pH of 4. Reflected light photomicroscope images (A and B) show evidence of carbonate shell dissolution and pyrite oxidation. False color EDS images (C and D) show Ca loss. SEM images (E and F) show void formation from the dissolution of carbonate shells.

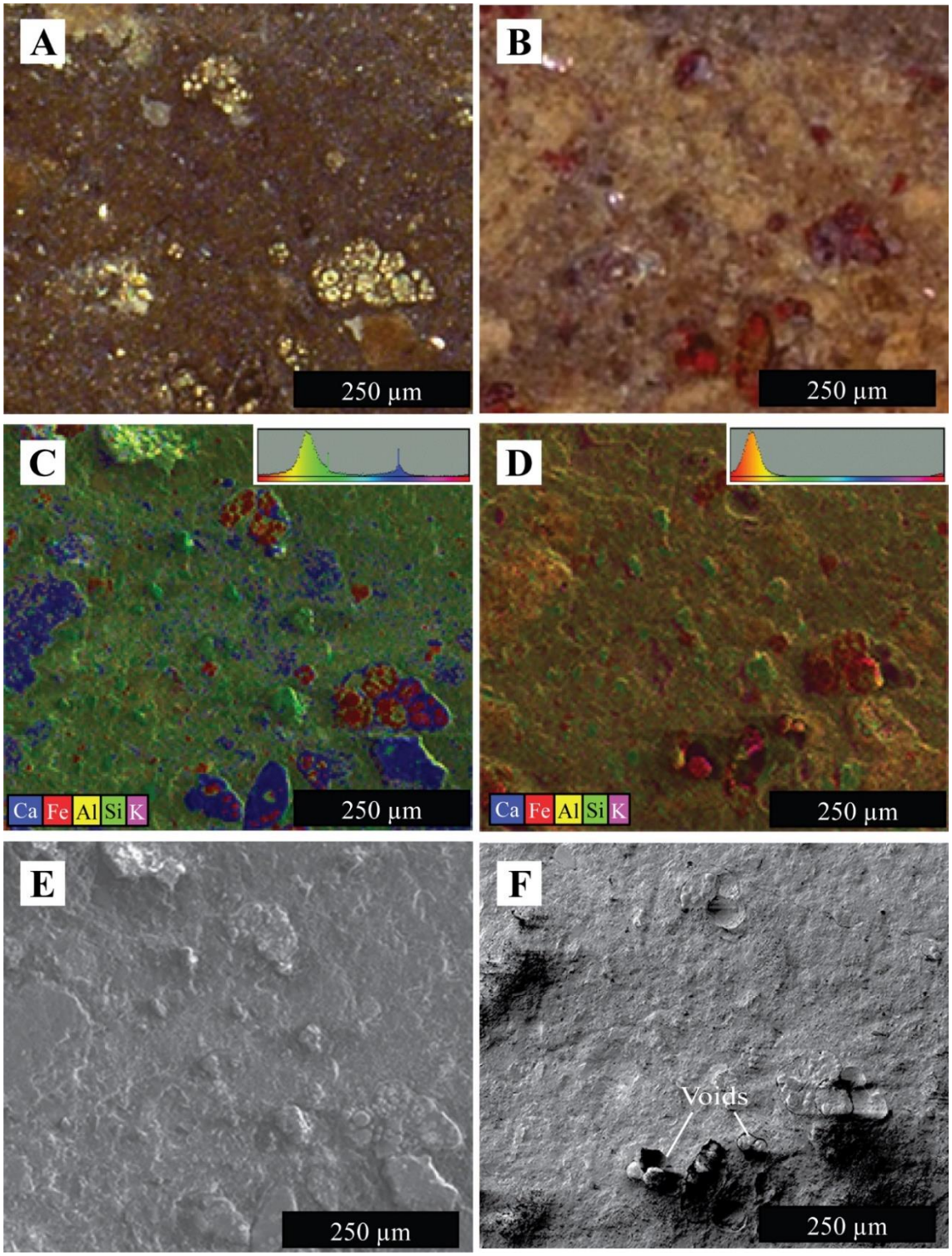

Figure C14. Images of mounted shale chips before (left) and after (right) to show physiological changes resulting from exposure to DIW water with initial pH of 6. Reflected light photomicroscope images (A and B) show evidence of carbonate shell dissolution and pyrite oxidation. False color EDS images (C and D) show Ca loss. SEM images (E and F) show void formation from the dissolution of carbonate shells.

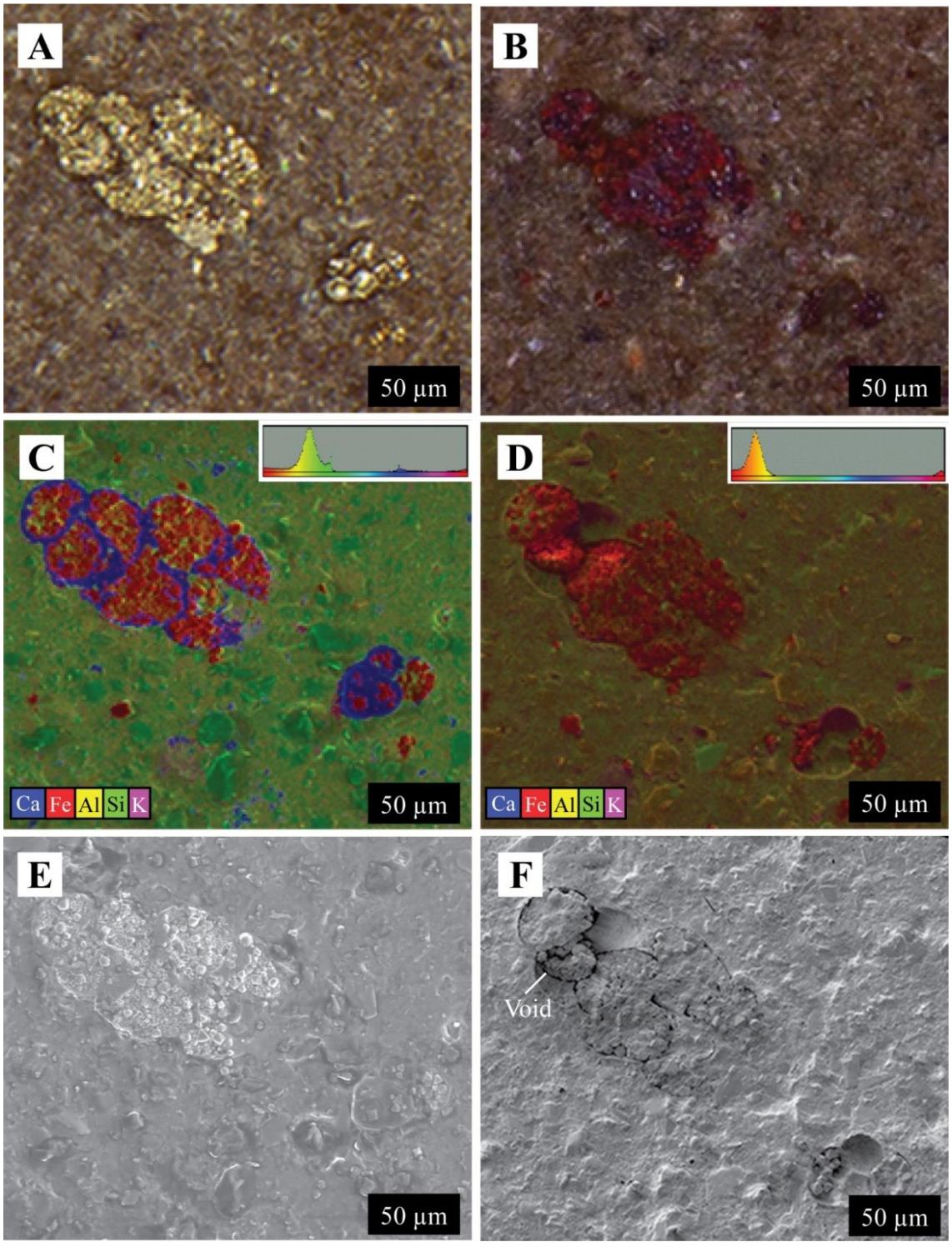

Figure C15. Images of mounted shale chips before (left) and after (right) to show physiological changes resulting from exposure to mixed composition solution water with 12% TDS and initial pH of 2. Reflected light photomicroscope images (A and B) show evidence of carbonate shell dissolution and pyrite oxidation. False color EDS images (C and D) show Ca loss. SEM images (E and F) show void formation from the dissolution of carbonate shells.

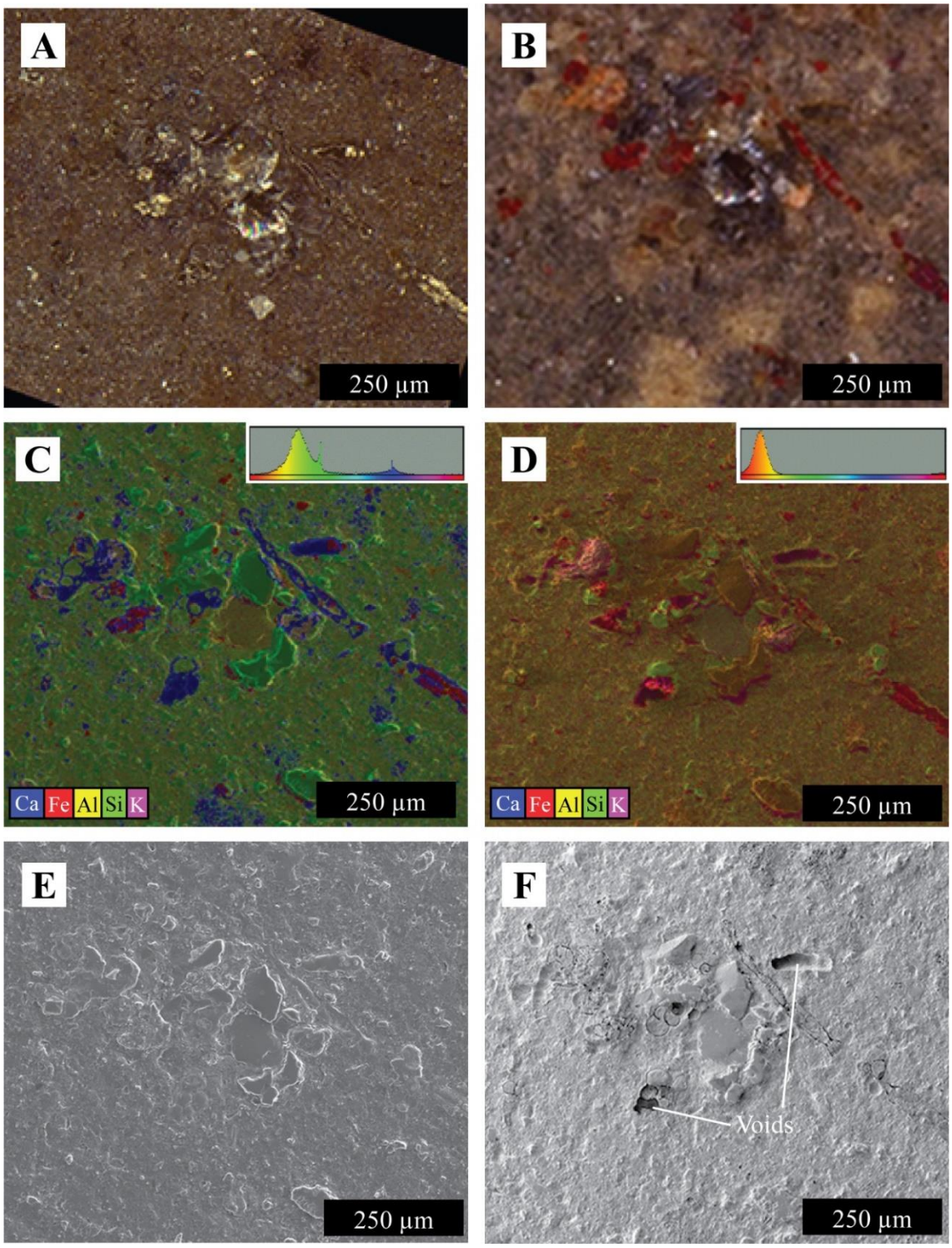

Figure C16. Images of mounted shale chips before (left) and after (right) to show physiological changes resulting from exposure to mixed composition solution water with 12% TDS and initial pH of 4. Reflected light photomicroscope images (A and B) show evidence of carbonate shell dissolution and pyrite oxidation. False color EDS images (C and D) show Ca loss. SEM images (E and F) show void formation from the dissolution of carbonate shells.

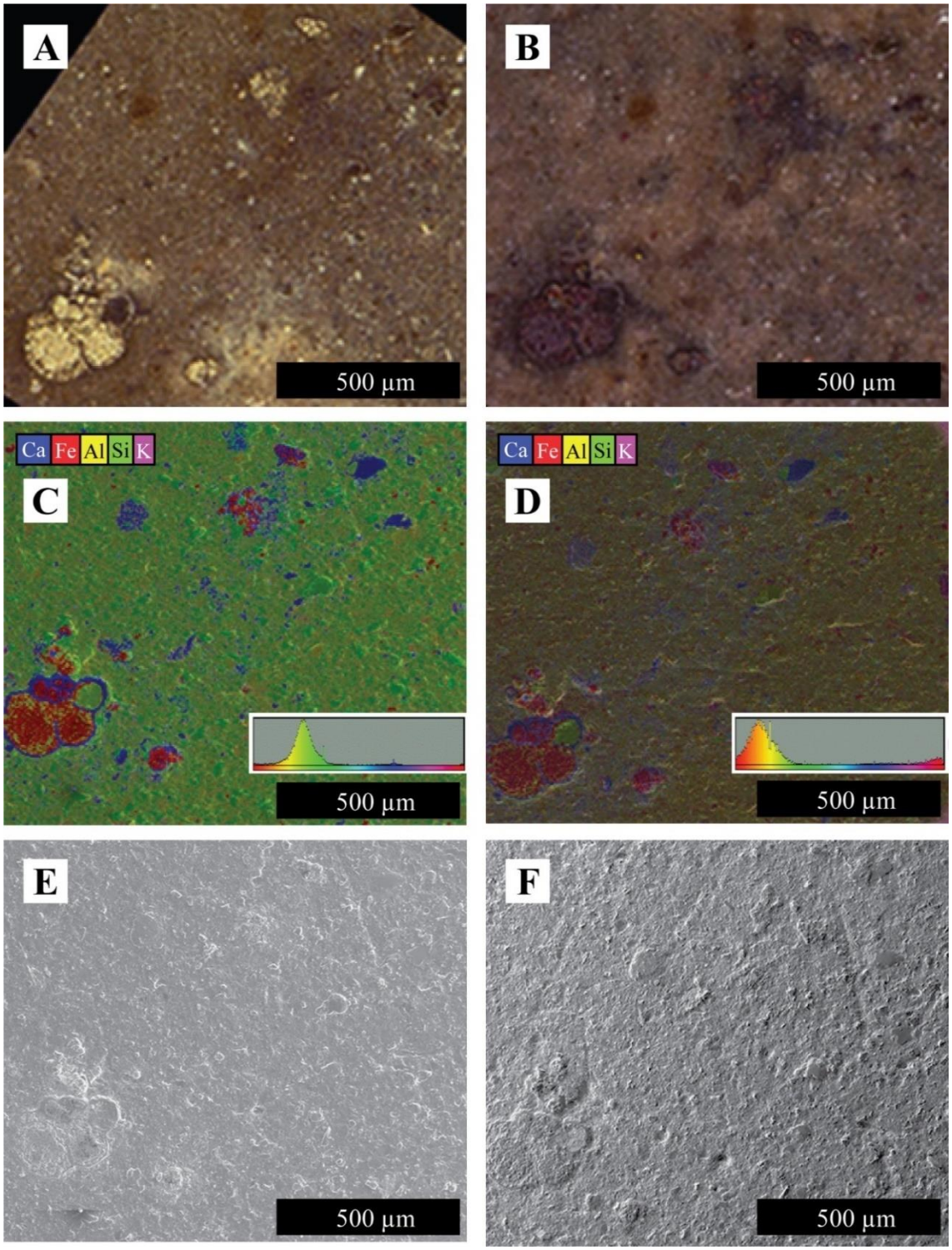

Figure C17. Images of mounted shale chips before (left) and after (right) to show lack of physiological changes resulting from exposure to mixed composition solution water with 12% TDS and initial pH of 6. Reflected light photomicroscope images (A and B) show evidence of pyrite oxidation but not carbonate shell dissolution. False color EDS images (C and D) show lack of Ca loss. SEM images (E and F) shows a lack of void formation.

BIBLIOGRAPHY

Acharya, H.R., C. Henderson, H. Matis, H. Kommepalli, B. Moore and H. Wang, 2011, Cost Effective Recovery of Low-TDS Frack Flowback Water for Re-use. U.S. Department of Energy, Washington, DC.

Alley, Bethany, Alex Beebe, John Rodgers Jr., James W. Castle, 2011, Chemical and physical characterization of produced waters from conventional and unconventional fossil fuel resources. Chemosphere, vol. 85, pp. 74-82.

André, Laurent, Vero Rabemanana, François-D. Vuataz, 2006, Influence of water-rock interactions on fracture permeability of the deep reservoir at Soultz-sous-Forêts, France. Geothermics, vol. 35, pp. 507-531.

Balashov, Victor N., Terry Engelder, Xin Gu, Matthew S. Fantle, Susan L. Brantley, 2015, A model describing flowback chemistry changes with time after Marcellus Shale hydraulic fracturing. AAPG Bulletin, vol. 99, no. 1, pp. 143-154.

Benko, K., and J. Drewes, 2008, Produced Waters in the Western United States: Geographical Distribution, Occurrence and Composition, Environmental Engineering Science, vol. 25(2), pp. 239-246.

Boschee, P., 2014, Produced and Flowback Water Recycling and Reuse. Oil and Gas Facilities

Carpenter, Aldren B. Micheal L. Trout and Edward E. Pickett, 1974, Preliminary Report on the Origin and Chemical Evolution of Lead and Zinc-Rich Oil Field Brines in Central Mississippi, Economic Geology, v. 69, pp 1991-1206.

Clark, C.E., and J.A. Veil, 2009, Produced Water Volumes and Management Practices in the United States, ANL/EVS/R-09/1, prepared for the U.S. Department of Energy, National Energy Technology Laboratory, September, 64 pp.

Engle, Mark and Elisabeth L. Rowan, 2014, Geochemical evolution of produced waters from hydraulic fracturing of the Marcellus Shale, northern Appalachian Basin: A multivariate compositional data analysis approach. International Journal of Coal Geology, vol. 126, pp. 45-56.

Harrison, Anna L., Adam D. Jew, Megan K. Dustin, Dana L. Thomas, Claresta M. Joe-Wong, John R. Bargar, Natalie Johnson, Gordon E. Brown Jr., Katherine Maher, 2017, Element release and reaction-induced porosity alteration during shale-hydraulic fracturing fluid interactions. Applied Geochemistry, vol. 82, pp 47-62.

Kharaka, Y. K., A. S. Maest, W. W. Carothers, L. M. Law, P. J. Lamothe and T. L. Fries, 1987, Geochemistry of metal-rich brines from central Mississippi Salt Dome Basin, U.S.A. Applied Geochemistry, vol. 2, pp 543-561.

Lester, Yaal, Imma Ferrer, E. Michael Thurman, Kurban A. Sitterley, Julie A. Korak, George Aiken, Karl G. Linden, 2015, Characterization of hydraulic fracturing flowback water in Colorado: Implications for water treatment. Science of the Total Environment, pp. 637-644.

Li, Jiawei, Zhixue Sun, Yin Zhang, Chuanyin Jiang, Claudia Cherubini, Alexander Scheuermann, Sergio Andres Galindo Torres, Ling Li, 2019, Investigations of heat extraction for water and CO_2 flow based on the rough-walled discrete fracture network. Energy, vol. 189, 116184.

Lu, Jeimin, Roxana Darvari, Jean-Philippe Nicot, Patrick Mickler, Sayyed A. Hosseini, 2017(a), Geochemical impact of injection of Eagle Ford brine on Hosston sandstone formation – Observations of autoclave water-rock interaction experiments. Applied Geochemistry, vol. 84, pp 26-40.

Lu, Jeimin, Patrick J. Mickler, Jean-Philippe Nicon, Wanjoo Choi, Willian L. Esch and Roxana Darvari, 2017(b), Geochemical interactions of shale and brine in autoclave experiments - Understanding mineral reactions dueing hydraulic fracturing of Marcellus and Eagle Ford Shales. AAPG Bulletin, v. 101, no. 10, pp. 1567-1597.

Olasolo, P., M.C. Juàrez, M.P. Morales, Sebastiano D'Amico, I.A. Liarte, 2016, Enhanced geothermal systems (EGS): A review. Renewable and Sustainable Energy Reviews, vol. 56, pp. 133-144.

Osselin, F., S. Saad, M. Nightengale, G. Hearn, A-M. Desaulty, E.C. Gaucher, C.R. Clarkson, W. Kloppmann, B. Mayer, 2019, Geochemical and sulfate isotpic evolution of flowback and produced waters reveals water-rock interactions following hydraulic fracturing of a tight hydrocarbon reservoir. Science of the Total Environment, vol. 687, pp. 1389-1400.

Pandey, S.N., A. Chaudhuri, S. Kelkar, V.R. Sandeep, H. Rajaram, 2014, Investigation of permeability alteration of fractured limestone reservoir due to geothermal heat extraction using three-dimensional thermo-hydro-chemical (THC) model. Geothermics, vol. 51, pp. 46-62.

Pandey, S.N., A. Chaudhuri, H. Rajaram, S. Kelkar, 2015, Fracture transmissivity evolution due to silica dissolution/precipitation during geothermal heat extraction. Geothermics, vol. 57, pp. 111-126.

Regenspurg, Simona, Thomas Wiersberg, Wulf Brandt, Ernst Huenges, Ali Saadat, Katja Schmidt, Günter Zimmermann, 2010, Geochemical properties of saline geothermal fluids from the in-situ geothermal laboratory Groß Schönebeck (Germany). Chemie der Erde, vol. 70, pp. 3-12.

Veil, John, 2012. U. S. Produced Water volumes and management practices in 2012. Prepaired for the Ground Water Protection Council, Veil Environmental, LLC, April, 119 pp.

Vengosh, Avner, Andrew Kondash, Jennie Harkness, Nancy Lauer, Nathaniel Warner and Thomas H. Darrah, 2017. The geochemestry of hydraulic fracturing fluids. Procedia Earth and Planetry Science, v. 17, pp. 21-24.

Zhang, Fu-Zhen, Pei-Xue Jiang, Rui-Na Xu, 2013, System thermodynamic performance comparison of CO_2-EGS and water-EGS systems. Applied Thermal Engineering, vol. 61, pp. 236-244.

VITA

Anna Atasha Hoffmann was born in Atlanta, Georgia. In 2012, they graduated with a B.S. in Geology from the University of Nevada, Reno, in Reno, NV. In 2016 they graduated with an M.S. in Geology with a focus on Metamorphic Petrology from Louisiana State University in Baton Rouge, LA. In May 2023, they received their Ph.D. in Geology and Geophysics with a focus on Aqueous Geochemistry in Petroleum Systems from Missouri University of Science and Technology in Rolla, MO.

As a graduate student, they worked as a Graduate Teaching Assistant for six semesters, assisting in Introductory Geology Labs and Mineralogy and Petrology courses. This inspired them to pursue a career as either an Instructor or Professor of Geology, where they aspire to provide a solid foundation in the subject matter and prepare and assist interested students in their own graduate experience.